UNIVERSIDAD COMPLUTENSE DE MADRID

FACULTAD DE CIENCIAS FÍSICAS

DEPARTAMENTO DE FÍSICA DE MATERIALES

MAGNETIC CONTROL OF SUPERCONDUCTING VÓRTICES

CONTROL MAGNÉTICO DE VÓRTICES SUPERCONDUCTORES

TESIS DOCTORAL DE:

ALICIA GÓMEZ GUTIÉRREZ

DIRIGIDA POR:

ELVIRA M. GONZÁLEZ

JOSÉ LUIS VICENT

Madrid, 2014

Magnetic control of superconducting vortices

Control magnético de vórtices superconductores

Alicia Gómez Gutiérrez

Departamento de Física de Materiales

Universidad Complutense de Madrid

Under the supervision of

Elvira M. González and José Luis Vicent

A thesis submitted for the degree of

PhD in Physics

2013

A mi hermana

A mi madre

A mi padre

“ Tell me and I forget,
Teach me and I remember,
Involve me and I learn.”
Benjamin Franklin

Agradecimientos

Esta tesis ha sido realizada en el Departamento de Física de Materiales de la Universidad Complutense de Madrid durante el periodo 2009-2013.

Durante estos años, son muchas las personas cuya aportación ha sido imprescindible en el transcurso de esta tesis, por ello, quisiera dedicarles unas palabras de agradecimiento.

En primer lugar, quiero agradecer a todos los miembros del Departamento de Física de Materiales. A los directores, Javier Piqueras y Fernando Sols, y al resto de profesores del departamento por facilitar la realización de este trabajo. A los técnicos Carlos Romero y Esther Garrido, por su infinita ayuda. A los becarios, por compartir esta experiencia conmigo, gracias por esas competiciones matinales (que difícil es el oro) y aguadas ayudas incluso en días festivos...Gracias especialmente al reciente doctor Javi Munárriz por su ayuda con el Latex.

Quisiera agradecer también al grupo del profesor Jacobo Santamaría. Mirko, Tornos, etc. gracias por toda la ayuda y colaboración en la sala,... y también fuera de ella.

Al Prof. Javier Palomares, Prof. Federico Cebollada y Prof. Jesús González por las películas de hierro monocristalinos estudiadas en el último capítulo de la tesis. Gracias también por vuestra colaboración y aportaciones.

I want to thank Prof. Kai Liu for giving me the opportunity to collaborate in his group during my stay in UC Davis. I am especially grateful to Dustin Gilbert for his hospitality during those months.

I would also like to thank CMT group at University of Antwerp for my stay in Belgium; especially Prof. Milorad Milosevic, for giving me that opportunity.

Quisiera agradecer al Prof. Ivan K. Schuller, por las intensas y fructíferas discusiones científicas. Gracias también por tu ayuda y por transmitirme tu inquietud científica.

I would like to thank Prof. Gernot Güntherodt and Prof. Jean-Pierre Locquet for agreeing to write the referee report needed for the admission of this thesis.

A los Prof. María Vélez y Prof. José Ignacio Martín de la Universidad de Oviedo, y al Prof. Miguel Ángel García, del Instituto de Cerámica y Vidrio, gracias por vuestra paciencia y amables respuestas a mis infinitos interrogatorios científicos.

Por últimos, dentro del marco profesional pero también personal, quiero agradecer a la pieza clave de esta tesis: mi grupo de investigación. Es fundamental tener un buen ambiente de trabajo para poder completar una tesis y vosotros me lo habéis ofrecido. Gracias Alejando Alija y David Pérez de Lara por los comienzos. Elena, contigo compartí mi primer congreso y muchos más momentos, gracias por tu atención. Las últimas incorporaciones: Fernando y Jorge, ¡mucha suerte! A los chicos, Javi y Luis, lo mejor de esta tesis, hemos formado un equipo que ha aprendido y crecido juntos (especialmente en la época AC), gracias por los interminables ratos juntos, el apoyo, las discusiones, risas, danzas, etc.

Parte de este grupo de investigación son mis directores de tesis Elvira y José Luis. Hay muchas formas de dirigir una tesis y no lo podríais haber hecho mejor. Gracias a los dos por confiar en mí desde el primer momento, por vuestra dedicación, por transmitirme vuestra sabiduría, por brindarme todas las oportunidades posibles y, sobretodo, por dejarme aprender de vosotros. No podría haber tenido mejor formación que la que me habéis dado entre los dos. Enhorabuena por vuestro trabajo, he sido afortunada.

Finalmente, quisiera acabar estos agradecimientos con las personas que, sin tener relación directa con esta tesis, han sido fundamentales en todos estos años.

Gracias Garo, Jorge, Ryu y muchos más compañeros de carrera; hicisteis divertidos los momentos más aburridos. Azahara, Esther, Pesquera y Víctor, gracias por seguir aguantándome lo inaguantable. Juntos llevamos nueve años de amistad y espero que sean muchos más.

Son muchas las personas que pasan por tu vida pero pocas las que se quedan. Quiero agradecer a mis amigas por estar siempre a mi lado y escucharme a pesar de no entender ni una palabra de lo que decía. Noelia, iniciamos este camino juntas y ahora eres un gran pilar de mi vida, sencillamente imprescindible. Gracias por quedaros.

Luis, pieza fundamental en este trabajo y en mi vida. Fuente inagotable de ánimos, fuerza y paciencia. Eres gran responsable de que haya llegado hasta aquí. Gracias.

La familia no se elige, te toca. Yo he tenido la suerte de tener la mejor familia que jamás podría haber elegido. Gracias por hacerme pensar que era capaz de todo lo que

me propusiera, por vuestra infinita paciencia cada vez que he tenido que tomar una decisión y por vuestro apoyo incondicional en todas las que he tomado. Sin vosotros, esto no hubiera sido posible. Os quiero.

Contents

1 Introduction

1.1 Motivation and outline

Superconductivity was discovered by H. Kamerlingh Onnes in 1911 when he measured that the resistance of mercury suddenly dropped to zero at the liquid helium temperature [1]. Since this discovery, an intense research on this field has developed new ideas in different areas of science (condense matter physics, material science, medical research, etc.) and technology.

In 1986, Bednorz and Müller discovered that certain oxides with perovskite strucuture are superconducting at temperatures above 30 K [2]. The following year, Chu and coworkers broke the liquid nitrogen temperature barrier with the discovery of YBaCuO, which is superconductor up to 93 K [3]. This finding opened new perspectives of science (they cannot be explained by the BCS theory) and applications (nitrogen is cheaper and easier to handle than helium). Among these applications, no-loss electric power lines, magnetically levitated trains, large magnets for medical and scientific applications, high sensitive magnetometers, etc. [4].

High temperature superconductors are the type-II superconductors [5]. In this type of superconductors, magnetic field can penetrate into the material in the form of small flux tubes called vortices. A transport current applied perpendicular to the vortices exerts a Lorentz force on them. When the current density exceed a critical value, so that the Lorentz force is higher than the pinning force, vortices start moving leading to a finite dissipation. An increase in the pinning force (enhancing the critical current which defines the threshold of vortex motion) is crucial for high current and power applications [4].

Intrinsic defects in the superconductors act like pinning sites and several studies have demonstrated that pinning can be easily enhanced by incorporating artificial structural defects [6, 7]. However, these pinning centers usually have deleterious effects on other superconducting properties, such as the reduction of the critical temperature.

A different approach has been shown in conventional superconductors by using arrays of magnetic nanostructures [8]. This approach provides the ideal scenario to understand and control the behaviour of vortex matter under many potential landscapes, which is crucial for basic reseach and future applications. Study the vortex dynamics in this type of magnetic/superconducting hybrid samples is the main objective of this thesis.

This dissertation is organized as follows:

- Chapter 1 contains a brief introduction to Type II superconductors and vortex dynamics in nanostructured superconductors.
- Chapter 2 describes the experimental methods used to fabricate and characterize magnetic/superconductor hybrid structures.
- Chapter 3 discusses the origin of the different features obtained at matching fields in the hybrids studied throughout this thesis.
- Chapter 4 contains the experimental results obtained for a bi-crystal like geometry of the pinning centers.
- Chapter 5 discusses the role of the magnetic stray fields in the dissipation behavior of this type of structures.

- Chapter 6 is devoted to the study of different vortex lattice dynamics (trapped vortex with and without interstitials and antivortex lattices).
- Chapter 7 discusses the interplay between magnetic and geometric ratchets.

Finally, the main results of this thesis will be summarized. A summary with the main points of this work is also available in Spanish.

1.2 Type II superconductors

1.2.1 Superconductors in magnetic fields

More than 20 years after the discovery of superconductivity, Meissner and Ochsenfeld found that superconductors do not behave as just ideal conductors, they act as perfect diamagnetic materials [5, 9]. When a superconductor is cooled down below its critical temperature, the magnetic field is expelled from the interior of the sample. This effect is known as Meissner effect and is maintained until certain critical field H_c is reached. The critical magnetic field destroys superconductivity and separates the normal and the superconducting states by a phase transition.

Soon, Fritz and Heinz London developed a phenomenological theory which successfully described the Meissener effect [5, 9]. The London equation together with the Maxwell equations implies a magnetic field that is exponentially screened from the interior of a superconductor over a certain distance. To expel the magnetic field, the superconductor generates screening (Meissner) currents that produce a magnetic field inside the superconductor equal in value and opposite in direction to the external field. This results in a screening of the interior of the sample from the applied field (B=0).

In 1950, Ginzburg and Landau (GL) proposed a generalization of the London theory based on the formalism of of the second-order phase transitions developed by Landau [5, 9]. By introducing a complex order parameter ψ, a good macroscopic description of the superconducting state is obtained. This order parameter is normalized to the superconducting electron density n_s:

$$n_s = |\psi|^2 \tag{1.1}$$

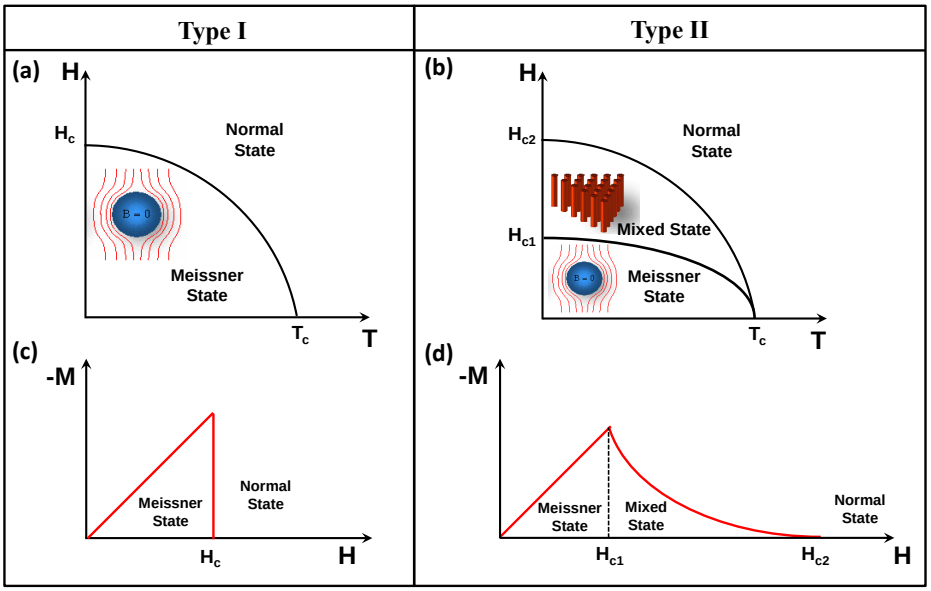

Figure 1.1: H-T phase diagram for a type I (a) and a type II (b) superconductors. Magnetization as a function of the applied magnetic field for type I (a) and type II (b) superconductors.

GL theory introduces two important characteristic lengths: the coherence length ξ and the penetration depth λ. The coherence length ξ controls the spatial variation of the order paramenter ψ. The penetration depth λ characterizes the length scale for variation of the magnetic field and the screening currents.

Both lengths exhibit a similar temperature dependence and they diverge as T$\rightarrow$T$_c$:

$$\xi(T) \propto \frac{1}{\sqrt{1-(T/T_c)}} \tag{1.2}$$

$$\lambda(T) \propto \frac{1}{\sqrt{1-(T/T_c)}} \tag{1.3}$$

The ratio between both magnitudes defines the GL parameter $\kappa = \lambda/\xi$ which is a material property and determines the behavior of a superconductor in an external applied magnetic field:

If $\kappa < 1/\sqrt{2}$ the superconductor is classified as type I. In this case, the superconductor behaves like a perfect diamagnet below the critical field H$_c$ (Meissner state). Above H$_c$,

superconductivity cannot be sustained and the sample turns to the normal state (see fig. 1.1(a)).

In contrast, for $\kappa > 1/\sqrt{2}$ a different behavior is obtained. In this case, the superconducting/normal (S/N) phase boundary energy is negative. Thus, the superconductor prefers the formation of as many domains as possible to increase the S/N surface area. Type II superconductors exhibit a different response to an external field and the phase diagram is described by two different critical fields (see fig. 1.1(b)). Below a certain lower critical field H_{c_1}, the superconductor is in the Meissner state. Over H_{c_1}, the magnetic field partially penetrates the superconductor in the form of quantized magnetic fluxs (fluxoids) forming the superconducting vortices and it is said that the superconductor is in the mixed state. This happens until the upper critical field H_{c_2} is reached, which turns the superconductor in the normal state.

Conceptually, the transition at H_{c_2} to the normal state arises when the normal cores of the vortices overlap. As the core size is temperature dependent (see eq. (1.2)), the upper magnetic field temperature dependence can be expressed as:

$$\mu_0 H_{c_2}(T) = \frac{\Phi_0}{2\pi\xi^2(T)} \tag{1.4}$$

The H-T phase diagrams for both type-I and type-II superconductors are shown in fig. 1.1 (a) and (b). Both types of superconductors have also a different behavior of the magnetization as a function of the external magnetic field, which are shown in fig. 1.1(c) and (d).

1.2.2 Vortex lattice

As was mentioned before, in type II superconductors for $H_{c_1} < H < H_{c_2}$ magnetic field penetrates the superconductor through the superconducting vortices.

Due to flux quantization, each vortex carries a quantized amount of magnetic flux Φ_0:

$$\Phi_0 = hc/2e = 2.07 \cdot 10^{-15} Tm^2 \tag{1.5}$$

As can be seen in fig. 1.2(a), vortices have a normal core of radio ξ where the order parameter vanishes (n_s) and the local magnetic field h(r) is maximum. Supercurrents

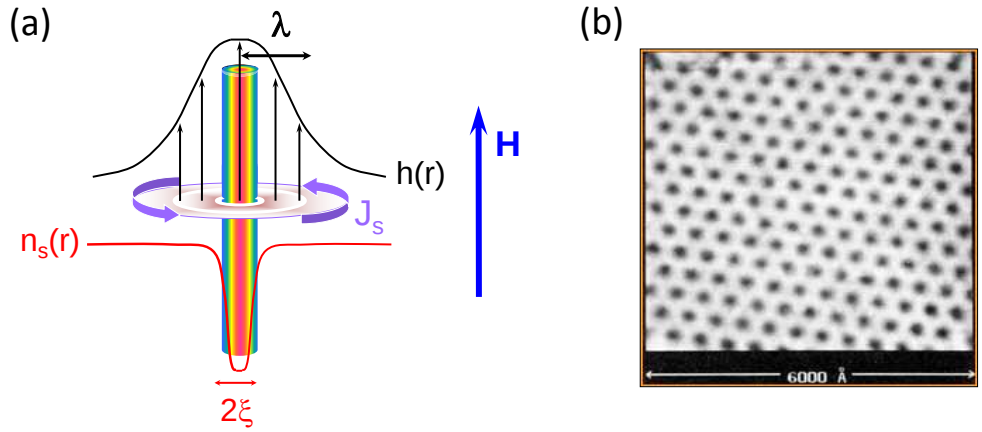

Figure 1.2: (a)Schematic of an isolated vortex in a type-II superconductor. H is the external magnetic field, λ and ξ are the penetration and the coherence length, n_s is the superconducting electron density, h(r) the local magnetic field and J_s the screening currents. (b) Scanning tunneling microscopy image of the Abrikosov vortex lattice of a Nb_3Sn single crystal (from Hess *et al.*[10]).

(J_s) circulating around the core concentrate the flux toward it and shield the rest of the superconductor. These screening supercurrents extend over a distance λ [5, 9].

Vortices experience a repulsive force from neighboring vortices due to the interaction of the circulating currents. Abrikosov showed that the lowest energy arrangement of vortices is a triangular array of lattice constant a_0:

$$a_0 = \left(\frac{2}{\sqrt{3}}\right)^{1/2} \sqrt{\frac{\phi_0}{B}} \tag{1.6}$$

Bitter decoration [11, 12], scanning tunneling microscopy (STM) [10, 13], Lorentz microscopy [14] and scanning hall probe microcopy [15, 16] are some of the experimental techniques that allow local visualization of the vortex lattice (see the STM image of a Nb_3Sn single crystal at 1.8K and 1T as an example in fig. 1.2(b)).

1.2.3 Vortex dynamics and vortex pinning

In a type II superconductor under an applied magnetic field $H_{c_1} < |\vec{H}| < H_{c_2}$, the superconductor is in the mixed state. If an external current $\vec{J}$ is applied perpendicular

to the vortices, a Lorentz force $\overrightarrow{F_L}$ is induced on the vortex lattice:

$$\overrightarrow{F_L} = \frac{1}{c}\overrightarrow{J} \times \overrightarrow{\Phi_0} \tag{1.7}$$

Under the influence of this Lorentz force, vortices start moving at a a certain velocity $\overrightarrow{v}$ and induce an electric field $\overrightarrow{E}$:

$$\overrightarrow{E} = \frac{1}{c}\overrightarrow{B} \times \overrightarrow{v} \tag{1.8}$$

This electric field is measured as a voltage drop along the direction of the current. Therefore, vortex motion is dissipative and leads to a non-zero resistance [5].

However, vortices interact with many types of intrinsic defects present in the superconductors (grain boundaries, dislocations, voids,...). This interaction can be attractive, so the vortex gets "trapped" or "pinned" in the defect by the pinning force F_p. This force can compensate the Lorentz force reducing the vortex mobility [5].

Critical or depinning current J_c is defined as the maximum current density that a superconductor can carry without resistance (so $F_p > F_L$). Over this critical current J_c, the Lorentz force overcomes the pinning force ($F_L > F_p$) and vortices start moving leading to a finite dissipation [5].

There are two main pinning mechanisms: core pinning and magnetic pinning [17].

- **Core pinning**. The free energy of the normal state exceeds that of the superconductor by $H_c^2/8\pi$ per unit volume. Both the normal core of the vortex and a cavity or defect (where the superconductivity is depressed) store a positive energy. If the vortex is located over the defect, the non superconducting volume is reduced and the energy of the system decreases. As a result, the vortex is attracted to the cavity.

- **Magnetic pinning**. Local magnetic fields generated by magnetic defects induce "Meissner type" screening currents that *expels* the field from the superconductor (see as an example fig. 1.3(a), where clockwise screening currents are generated to expel the stray field produced by a $\overrightarrow{m_z}$ magnetic moment). Imagine a superconducting vortex generated by a $\overrightarrow{H_z}$ external field; in this case, vortex supercurrents tend to *concentrate* the magnetic field in its core, so supercurrents circulate in

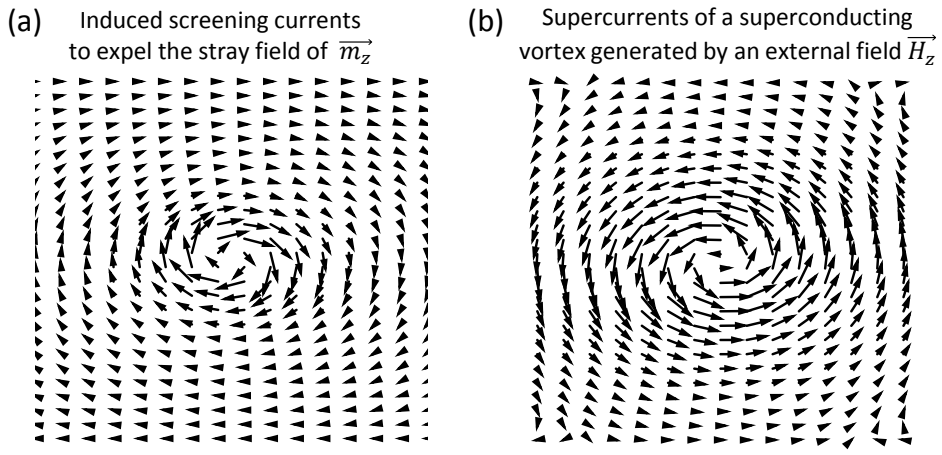

Figure 1.3: Magnetic pinning mechanism. (a) shows the clockwise supercurrents generated to expel the magnetic stray field produced by a m_z magnetic moment. (b) shows the anticlockwise supercurrents that surround a vortex generated by an external applied magnetic field H_z.

anticlockwise direction (see fig. 1.3(b)). If the vortex places on top of the magnetic defect, both supercurrents compensate and the free energy is reduced. Depending on the relative alignment between the external magnetic field and the magnetic moment, the interaction between a vortex and a magnetic moment can be attractive or repulsive.

1.3 Vortex dynamics in magnetic/superconducting hybrids

Progress in lithography techniques made it possible to reduce the size of the pinning centers to the order of tens or hundreds of nanometers. These sizes are comparable to the penetration depth and the coherence length, producing an enhancement in the interaction between the pinning site and the superconducting vortex. Since then, vortex dynamics and pinning effects by ordered arrays of nanodefects have been intensively studied (see, for example, the topical reviews of M. Velez *et al.* [18] and A. Yu. Aladyshkin *et al.* [19]).

Particularly, magnetic pinning sites embedded in the superconductor have been shown to act as effective pinning sites [8]. In addition, different geometries, magnetic

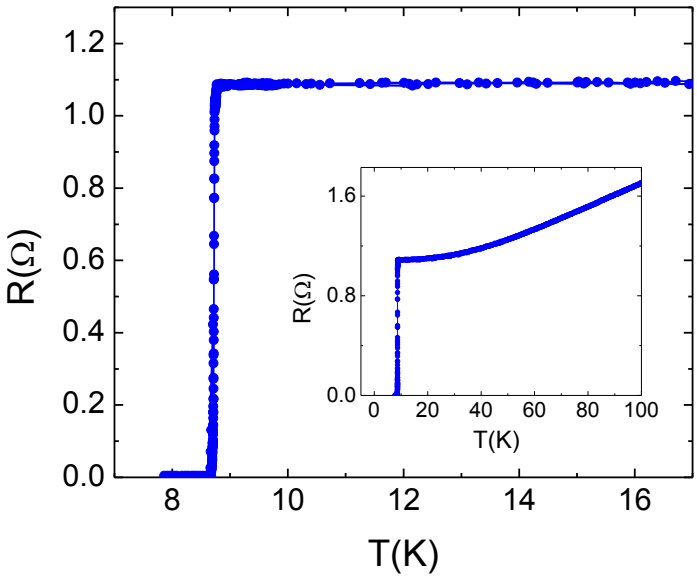

Figure 1.4: Resistance *vs.* Temperature for a Nb film grown on top of a rectangular array of Ni nanodots. Inset shows a wider temperature range.

states, etc. produces spatial variation of the pinning potential landscape which modifies the vortex dynamics. In this thesis, magnetic/superconducting hybrids will be studied. This section gives a briefly overview of vortex dynamics in this type of samples using, as an example, a 100 nm thick Nb superconducting film grown on top of a rectangular array of Ni nanodots.

1.3.1 Superconducting transition

The first step to characterize an hybrid sample is to determine the critical temperature. Fig. 1.4 shows a typical transition of a 100 nm Nb film measured with 10 μA. As can be seen in the inset, resistance (R) decreases with the temperature (T), which is the typical metallic behavior of the resistance. Once the temperature reaches the critical temperature (T_c), a sudden drop to zero is measured.

A criterion of $0.5R_N$ is used to define the critical temperature T_c, where R_N is the normal state resistance. The transition width ΔT_c is obtained as $T(0.9R_N)$-$T(0.1R_N)$ and gives information about the quality of the film.

For this hybrid sample, the critical temperature is T_c=8.74 K and the transition width ΔT_c = 30 mK.

1.3.2 Commensurabily effect

As previously mentioned, in a uniform superconductor, the minimum energy vortex configuration corresponds to the Abrikosov triangular lattice. However, in the presence of defects, vortices prefer to be placed at the positions where the system energy is minimized, distorting the triangular lattice [5].

In the presence of a periodic pinning array, for certain matching fields (B_{match}), the density of the vortex lattice equals an integer number of the density of the pinning density [7, 8]. At these fields, there is an integer number of vortices (n) per unit cell of the array of pinning centers.

$$B_{match} = n\frac{\Phi_0}{S} \tag{1.9}$$

where S is the unit cell area of the pinning array and Φ_0 the quantum fluxoid (eq. (1.5)).

For these matching fields, the Abrikosov lattice is distorted into the geometry of the pinning array which results in a pinning enhancement of the vortex lattice. This so-called *commensurability effect* gives rise to pronounced features in the superconducting properties at the matching fields (such as minima in the resistance or peaks in the critical current) [20].

As an example, the field dependence of the resistance has been measured in a 100 nm thick Nb superconducting film grown on top of a rectangular array of Ni nanodots. The nanodots are 40 nm thick and are arranged on a rectangular lattice of 400 nm x 600 nm. The critical temperature of the hybrid sample is T_c=8.74 K as shown in fig. 1.4.

Fig. 1.5 shows the magnetoresistance curve obtained at $0.985T_c$ and with 100μA of applied current. Deep minima in the resistance appear at certain fields [8]. The experimental interval between minima ($\Delta B_{match_{exp}}$=85.3 Oe) is in good agreement with the theoretical value obtained from eq. (1.9) for n=1:

$$B_{match} = \frac{\Phi_0}{S} = \frac{\Phi_0}{400nm \cdot 600nm} = 86Oe \tag{1.10}$$

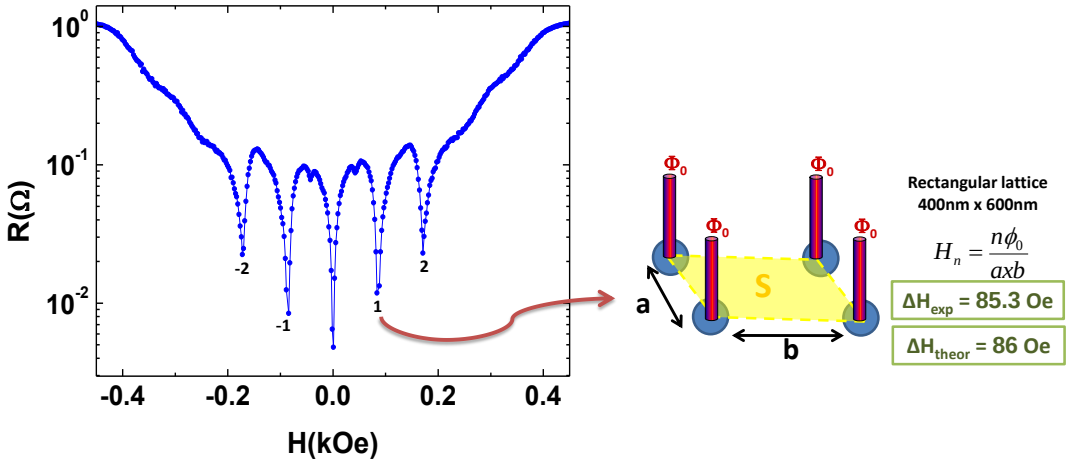

Figure 1.5: Field dependence of the resistance for a Nb film grown on top of a rectangular array of Ni nandots, measured at 0.985T$_c$ and with 100 μA.

Fig. 1.5 schematically shows the commensuration between the vortex lattice and the pinning array at the first matching field (n=1) (for which the density of vortex lattice equals the density of pinning centers). As a result of this commensuration, the vortex lattice motion slows down and minima appear in the dissipation (resistance).

Commensurability effect has been studied using different geometries (triangular[8], rectangular [21], kagomé [22, 23], honeycomb [24], quasiperiodic arrays [25], etc.) showing different matching minima structures due to the interaction between the vortex lattice and the different geometries of the pinning arrays.

1.3.3 Ratchet effect

Firstly, C. S. Lee *et al.* [26] theoretically suggested that vortex motion could be controlled by an asymmetric potential. They showed that the application of an alternating current to a superconductor patterned with an asymmetric pinning potential can induce a net vortex motion whose direction is determined only by the asymmetry of the pattern. The mechanism responsible for this phenomenon is the so-called *ratchet effect* [27].

Villegas *et al.* explored the vortex dynamics in a Nb film grown on top of a square array of Ni nanotriangles (see fig. 1.6(a)). The triangular shape of the dots resulted in

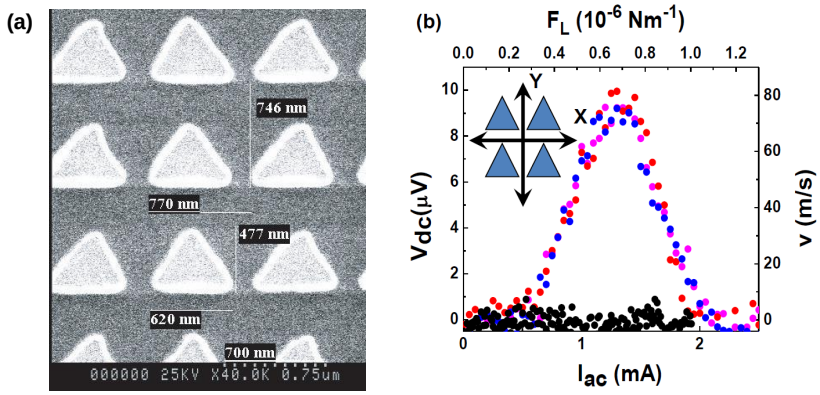

Figure 1.6: (a) SEM image of Ni triangles. (b) Dc voltage versus ac current amplitude for an applied field H=H_1 and T=0.99T_c. Magenta, blue and red circles correspond to frequencies ω= 10 kHz, ω= 1 kHz, ω= 0.5 kHz, respectively, with vortex motion parallel to the y axis. Black circles correspond to ω= 10 kHz for vortex motion parallel to the x axis. From Villegas *et al.* [28].

an asymmetric potential along the base to tip direction. In this work, an alternating driving current (I_{ac}) injected in the sample yields to an ac Lorentz force (F_L) in the perpendicular direction. It has to be noticed that the time averaged force on the vortices is zero ($\langle F_L \rangle$=0) as an alternating current is applied.

Vortex motion was studied along two different directions for the first matching field (H=H_{match}, one vortex is trapped in each triangle):

- *Vortex motion along the base-to-tip direction*: I_{ac} was injected along the x axis to study vortex motion along the base-to-tip direction. Due to the asymmetry along this direction, a rectification of the vortex motion was obtained, which was characterized by a non-zero dc voltage drop (see colored dots in in fig. 1.6(b)).

- *Vortex motion along the base direction*: I_{ac} injected along the y axis yields an ac Lorentz force on the vortices along the x axis (see eq. (1.7)). As there is no asymmetry along this direction, no rectification is obtained and the measured dc voltage signal is zero (see black dots in fig. 1.6(b)).

Interestingly, in this work, for H>3H_{match}, a dc reversed signal begin to develop for

lower Lorentz forces. This reversal signal is the fingerprint of the presence of interstitial vortices which feel a weak and inverted ratchet potential [28].

Progress in theory and experiments have developed various techniques for producing nanostructured pinning landscape that provide tailored asymmetries for vortex ratchets. See for example the review of vortex ratchets by P. Hänggi and F. Marchesoni [29].

2
Experimental Methods

In this chapter, the fabrication and characterization techniques used throughout this thesis will be explained. These techniques allow us to fabricate and characterize hybrid structures made of magnetic arrays of nanoelements embedded in superconducting films.

In the first section of this chapter, the fabrication process of the hybrids will be explained. Sputtering, lithography and etching techniques have been utilized. In the second and the third section, we will focus on the structural and magnetic characterizationtechniques, respectively. The structural characterization has been performed by X-ray diffraction.For, the magnetic characterization, two different magnetometers and OOMMF simulations have been used. Finally, in the last section, the experimental set-up for the low temperature characterization will be explained.

2.1 Fabrication techniques

Fig. 2.1 shows a schematic of the different steps needed to fabricate the hybrid samples:

1. Most of the samples studied in this thesis are polycrystalline, so silicon wafers

are usually chosen as substrates. An appropriate cleaning to remove unwanted particles is required; usually 10 minutes of ultrasonic bath in acetone and methanol is enough. In the case of the single crystal Fe nanotriangles, a MgO substrate was chosen to obtain the epitaxial growth of the Fe thin film.

2. Electron beam lithography (EBL) and DC magnetron sputtering are employed to define the nanopatterns that will interact with the vortex lattice. After this fabrication step, scanning electron microscopy (SEM) is used to analyze the final result of the nanopattern.

3. Once the nanopattern has been defined, DC magnetron sputtering in a high vacuum chamber, with a base pressure of $5{\cdot}10^{-8}$ Torr, is used to deposit the superconducting niobium thin film on top on the nanopatterned array.

4. Finally, standard photolithography and ion etching techniques are used to define a cross-shaped 40 μm bridge centered on the array to carry out the magneto-transport measurements. This bridge allows us to inject the current and measure the voltage drop in the standard four-point configuration in two perpendicular directions (see fig. 2.1 - point 4).

Fig. 2.2 shows an image of the final sample mounted in a rotatable sample holder that will be introduced in the He cryostat to perform the magneto-transport experiments.

In the following subsections we will describe the most important techniques used to fabricate the samples studied in this thesis: dc magnetron sputtering for thin film deposition, lithography techniques (optical and electron beam lithography) and reactive ion etching.

2.1.1 DC Magnetron Sputtering

Two thin film deposition steps are needed to fabricate the hybrid samples: (i) In the EBL process (2^{nd} step in fig. 2.1), a magnetic material is deposited to obtaine the array of pinning centers; (ii) in the 3^{rd} step in fig. 2.1, a superconducting Nb thin film is deposited.

Sputtering is based on the ejection of surface atoms of a target material by momentum exchange with high energy particles generated in a plasma. Most materials

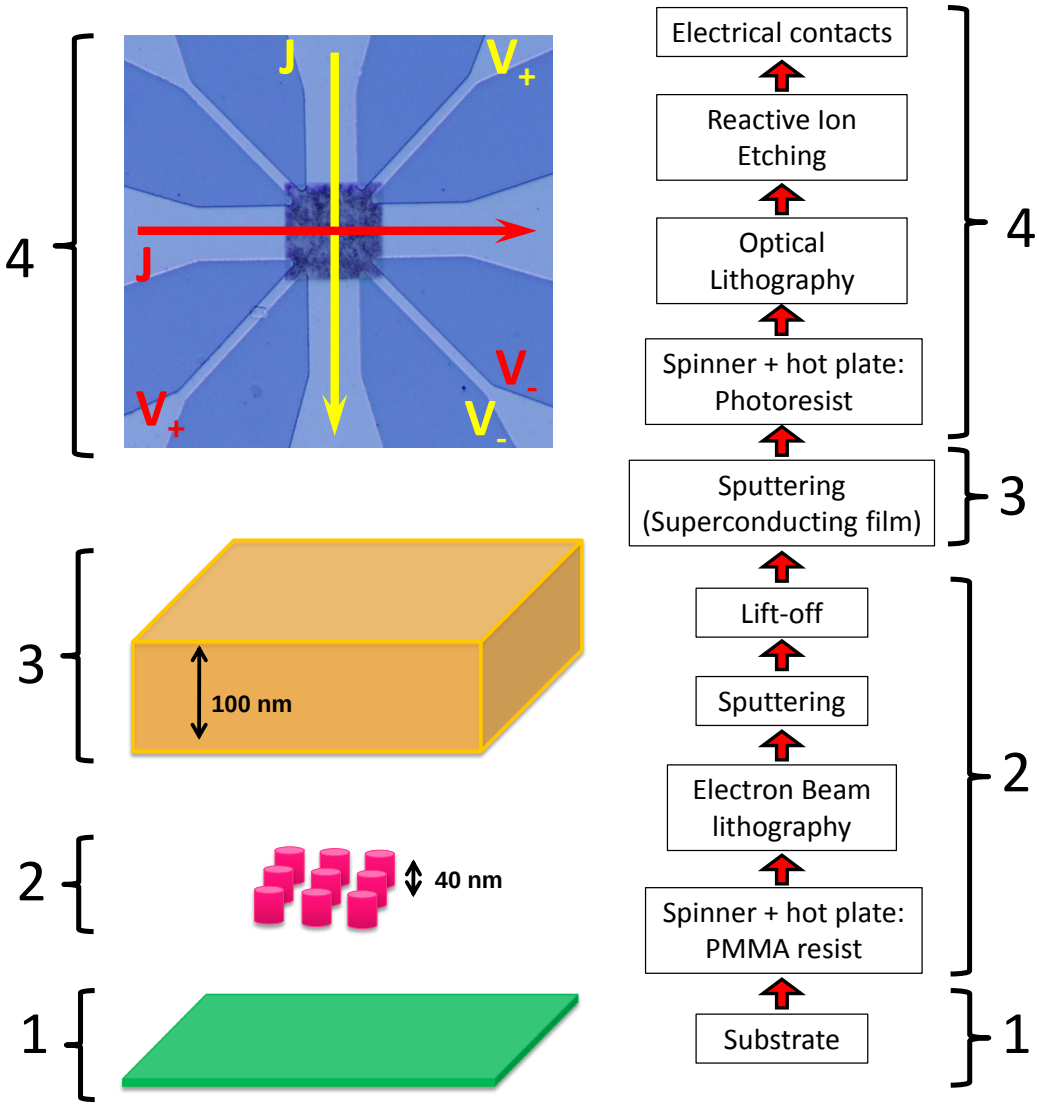

Figure 2.1: Schematic of the different steps followed to fabricate an hybrid sample. 1: Substrate; 2: Fabrication of the ordered array of pinning centers; 3: Deposition of the superconducting thin film; 4: Cross-shaped bridge fabrication to perform the transport measurements.

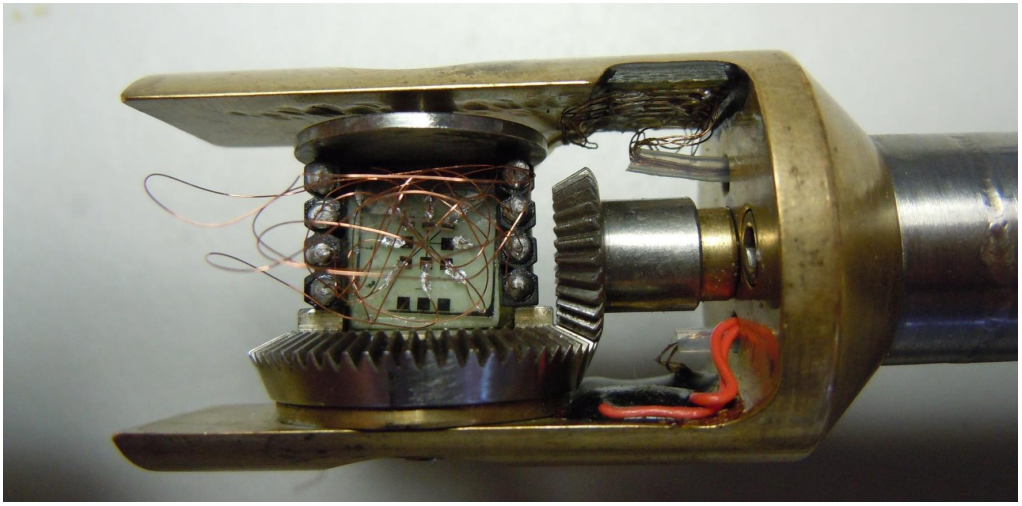

Figure 2.2: Image of the final hybrid sample with the electrical contacts mounted in the sample holder to do the transport characterization.

can be sputtered, so sputtering is a well-known technique used to deposit conductors, semiconductors, insulators and magnetic/non-magnetic materials.

The superconducting thin film is deposited in the Microscience system shown in fig. 2.3(a), whereas the magnetic material is deposited in AJA system fig. 2.3(b). Fig. 2.3(c) shows an image of the plasma in the AJA system during deposition of a nickel thin film.

The Microscience system consists of a main chamber and a load lock chamber. Both are connected to a turbo molecular pump supported in the back side by a rotatory roughing pump that exhausts gas from the rear part of the turbo pump. The base pressure in the main chamber is in the 10^{-8} Torr range which is measured by a Bayard-Alpert ion gauge. This high vacuum conditions are necessary in order to avoid contamination in the deposited thin film. During deposition, a constant Ar flow is injected and controlled by needle valves to keep the pressure in the mTorr range.

Inside the chamber, a Nb target is mounted in a magnetron sputtering gun. The target is placed on top of a water cooled Cu plate with magnets that generate a magnetic field to confine the plasma above the target increasing the deposition rate with lower Ar pressures. To enable the ignition of the Ar plasma, a negative potential is applied to the

target so the Ar^+ are accelerated towards it. These Ar^+ ions, via momentum transfer, extract the Nb atoms from the target surface which will adhere to the substrate and form the Nb thin film.

Typical Ar pressure is 10 mTorr for Nb deposition and 75 W are applied to the target. To avoid contamination in the thin film, the target is pre-sputtered for at least 10 minutes to obtain a clean surface (usually it is cleaned from oxidation which is observed by a red color of the plasma and high voltage and low current in the target). Once stable values of current and voltage are achieved, the film is deposited. The growth rate for I=268 mA, V=273 V and P=75 W is 5.6 $\AA$/s, so 3 minutes of sputtering are needed to deposit a 100 nm Nb film. Usually, together with the hybrid sample, a second clean Si substrate is loaded as a reference sample.

The AJA system is a simple and versatile system that allows depositing up to 11 samples in the same run. In this equipment, there is no load lock chamber and base pressure is usually higher (in the 10^{-7} Torr range). To reach better vacuum conditions, a liquid nitrogen trap can be used which lowers the pressure to $2 \cdot 10^{-8}$ Torr by condensing the gas atoms in a cold surface (see fig. 2.3(b)). Usually 1 mTorr of Ar pressure is injected and 30 W are applied to generate the plasma.

2.1.2 Electron Beam Lithography (EBL)

Electron beam lithography is the ideal tool to define small areas with nanometric resolution. It is based on the chemical modification of a polymer resist film caused by electron irradiation. In this case, because of the small wavelength of the 10-30 KeV electrons, resolution is not limited by diffraction limits, but by electron scattering in the resist and by the various aberrations of the electron optics. The best achieved resolution is around 10 nm. The main limitation of this technique is throughput, *i.e.*, it is a slow technique and it is very difficult to define large areas of a small pattern due to beam drift or instability during the exposure.

Before pattern writing, the sample needs to be prepared: after cleaning the substrate, it is covered with an electron beam sensitive resist. In our case, MicroChem 950 PMMA A4 positive resist is spinned at 4500 rpm for 1 minute and baked at 180 °C for 3 minutes in a hot plate. If the coating is good, the layer will be uniform and only one color will

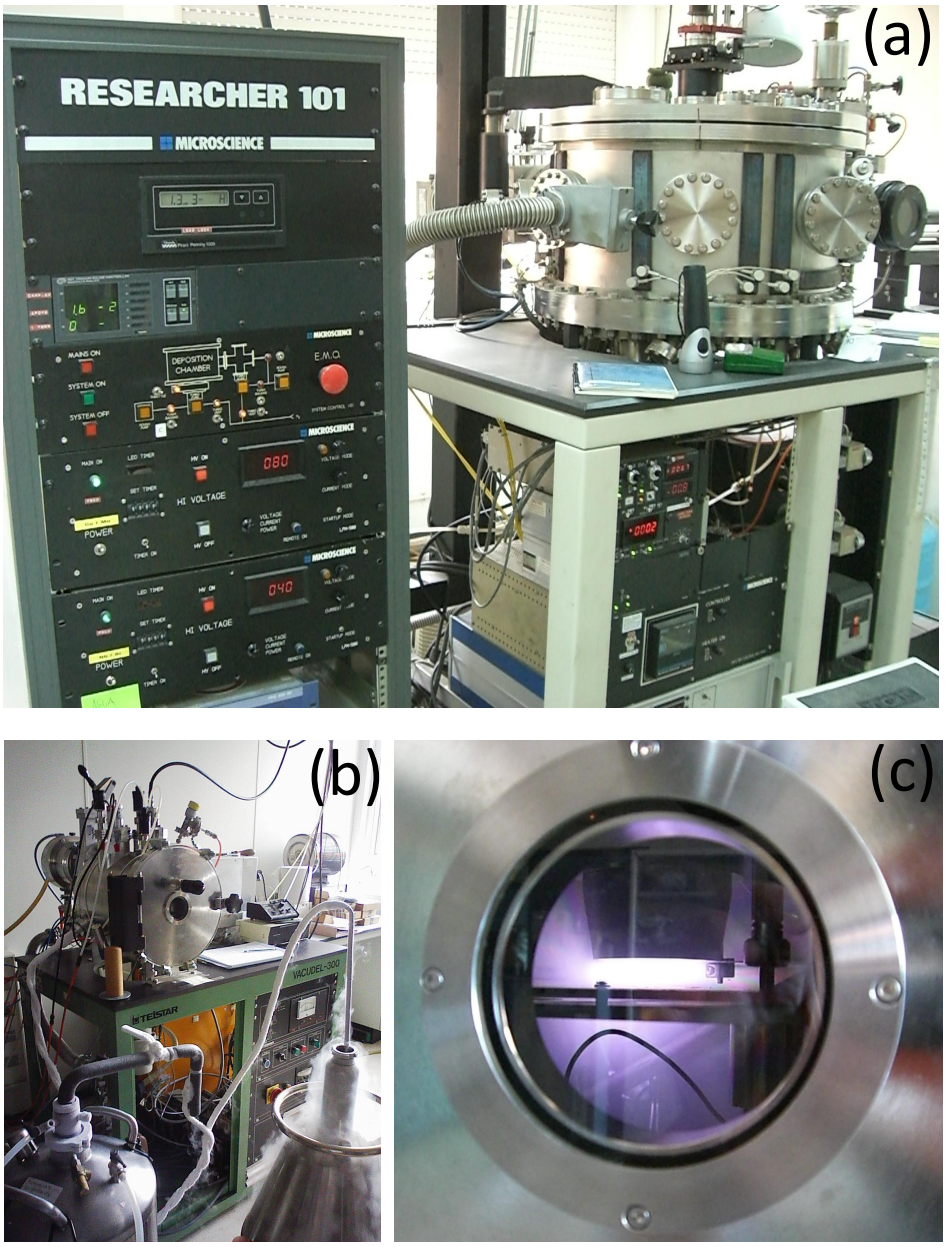

Figure 2.3: (a) Microscience sputtering system.(b) AJA sputtering system. (c) Image of the plasma during deposition in the AJA sputtering system.

be noticed. If multiple color reflection is obtained, the coating should be repeated after cleaning the substrate using the usual procedure.

Once a uniform layer of the resist have been deposited, the exposure procedure starts. We use a Raith 50 Electron Beam Lithography System (see fig. 2.4(a)). This system consist of a scanning electron microscope connected with a design editor and a pattern generator which guides the electron beam over the substrate surface. We use a LaB_6 filament with a typical accelerating voltage of 10 kV. To write a pattern into the resist directly, a computer generated pattern file controls the electron beam by deflecting and turning the beam off and on according to the pixilated patterns.

Focus and astigmatism need to be corrected before exposure. Once the beam is optimize and stabilized, the emitted electron current is read in a Faraday Cup (which is connected to a picoammeter). Usually, 100 pA is used, but it should be adjusted depending on the size of the structures that are going to be defined (the higher the current, the bigger the spot size). The measured current is used to calculate the dwell time (time that the beam stays in each pixel) needed to obtain a certain dose. The choice of a good dose is a crucial point in order to achieve a good pattern definition. It depends on several parameters like the type of resist, the thickness of the resist, the design pattern (due to proximity effects), etc. In our case, the typical area dose is around 250 $\mu C/cm^2$.

After adjusting the beam, the pattern is designed. This type of lithography does not need a mask, like in the case of the photolithograpy, so different patterns can be easily design, see fig. 2.4(b) as an example. In addition, a coordinate system with respect the edge of the sample can be defined so that the pattern is aligned and placed in the exact position. It typically takes around 5 minutes to expose a 100 μm^2 array of 200 nm diameter nanodots. Usually several patterns are exposed with different doses, so the best one can be chosen afterwards (see fig. 2.4(c)).

Finally, the sample is developed in MIBK (methyl isobutyl keton): IPA (isopropyl alcohol)(1:3) solution for one minute, rinsed in IPA for another minute and dried with nitrogen. As positive resist is used, the area exposed by the electron beam is removed in the development and holes in the resist are obtained.

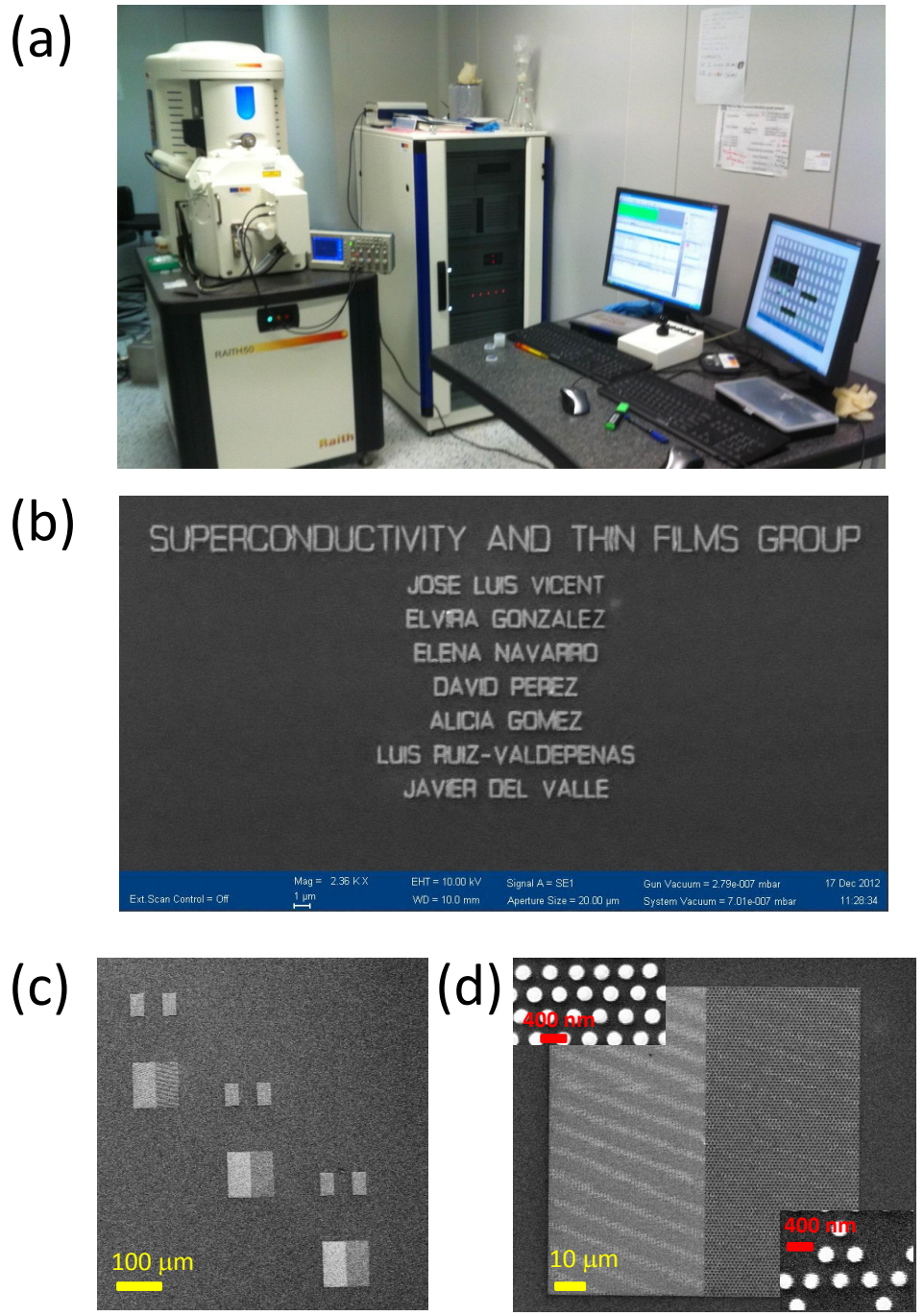

Figure 2.4: (a)Raith 50 Electron Beam Lithography System. (b), (c) and (d) show SEM images of different patterns defined by EBL (bar scales are included in the images).

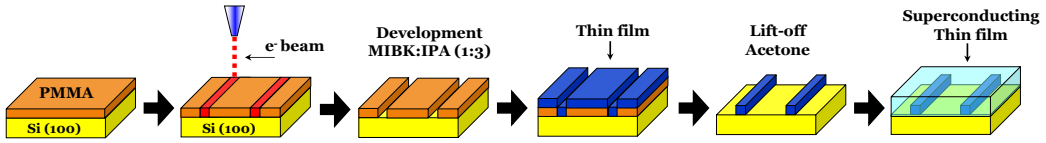

Figure 2.5: Schematic diagram of the e-beam lithography steps.

DC magnetron sputtering is used to deposit a thin film of the magnetic material that will fill the holes defined in the resist. Finally, lift off is done by boiling the sample in acetone to remove the rest of the resist.

Scanning electron microscopy is used to ensure the quality of the sample and measure the dimensions of the obtained array before depositing the superconducting thin film (see fig. 2.4(d)).

Fig. 2.5 depicts a summary of the electron beam lithography process, showing the steps of the procedure.

2.1.3 Optical Lithography

Optical lithography or photolithography is an optical system that transfers an image from a mask to a resist. It is a fast technique and it is commonly used to mass production of chips in the semiconductor industry. The spatial resolution of photolithography techniques is an overall contribution of the optics, alignment, development, etching... but, it is particularly dependent on the wavelength of the light used in the exposure process due to the diffraction limit. In our case, a UV lamp is used as lightsource ($\lambda \approx$400 nm) and the smallest feature that we can obtain is around 2 μm; however, recent developments have included exposure sources with smaller wavelengths (such as KrF and ArF lasers or X-rays) in order to reach smaller feature sizes (getting to resolutions up to tens of nanometers).

Photolithography proccedure is similar to the previously explained in the EBL and it is summarized in fig. 2.6. The first step is to coat the film with a suitable photosensitive resist by spin coating. In our case, Microposit S1813 positive resist is spinned at 5000 rpm for 40 seconds. Then, the resist is heated in a hot plate at 115° for 60 seconds. This process is called "soft bake" and is done in order to remove solvents from the resist before exposure.

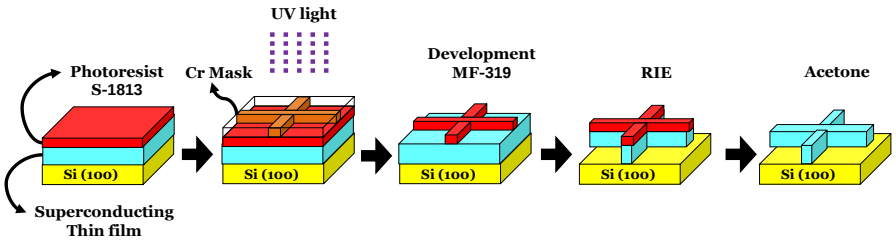

Figure 2.6: Schematic diagram of the photolithography and RIE steps necessary to define the measurements bridge.

This is followed by the alignment of a mask and exposure with the UV light source. The mask is a quartz substrate covered with a layer of chromium which defines the pattern. When the light shines though the photomask, the chromium part will block the light in some areas and will protect the resist. As a positive resist is used, the polymer chains that constitute the resist are broken in the exposed region and, later, the developer will wash away these parts. Microposit MF-319 is used as developer, where the sample is rinsed for 60 seconds to remove the illuminated parts.

As a result of the previous steps, a positive copy of the mask in the resist is obtained that will protect the superconducting thin film in the etching process (see fig. 2.6).

2.1.4 Reactive Ion Etching (RIE)

The final stage of the fabrication process is to transfer the pattern from the resist to the Nb film. This is done by an etching process which removes any material that is not protected by the resist and may be either a wet or dry process. In this case, we use dry chemically assisted reactive ion etching.

A Southbay 2000 Reactive Ion Etcher is used. The operation procedure is similar to the explained in section 2.1.1. Mass flow controllers and needle valves are used to inject in the chamber a mixture of Ar and SF_6 which generate the plasma by an alternating RF electromagnetic field. Particularly, the pressure condition is 7 sccm of Ar and 14 sccm of SF_6 at 40 mTorr of total pressure. 150 W RF power is applied to get the plasma.

This mixture of gases combines plasma and sputter processes: SF_6 molecules are dissociated and F atoms react with the Nb film producing NbF_5 which is volatile and is

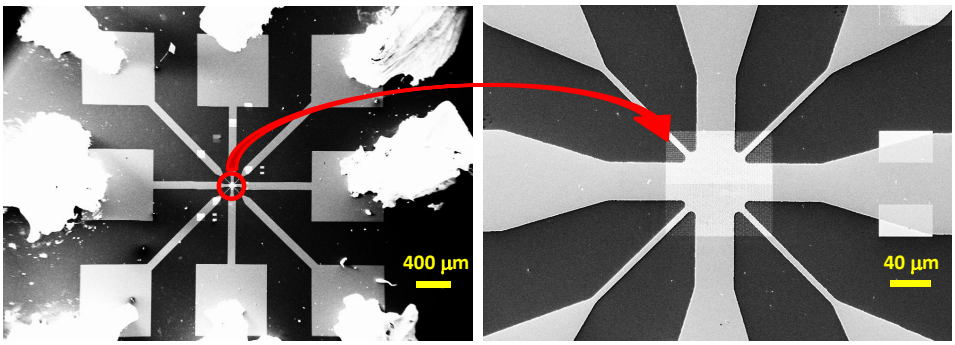

Figure 2.7: (a) SEM image of the final hybrid sample showing the electrical contacts in the cross-shaped bridge (defined by photolithography and RIE). (b) SEM image showing the alignment of the bridge with the array of nanoelements (fabricated by EBL).

pumped out of the chamber. However, these molecules can be deposited in the surface blocking the films, so, Ar atoms are introduced in the plasma to physically remove (by momentum transfer) the volatile molecules which would passivate the film surface [30].

Fig. 2.7 (a) shows the final hybrid sample (including the indium electrical contacts). As can be seen in more detail in fig. 2.7(b), a Nb cross-shaped bridge centered in the array defined by EBL is obtained after the photolithography and etching processes.

2.2 X-Ray Structural Characterization: XRD and XRR

X-Ray Diffraction (XRD) and X-Ray Reflectivity (XRR) patterns allow determine the structural properties of our samples. Particularly, thickness, roughness and crystal structure can be obtained by analyzing these patterns.

These experiments have been carried out in a X-ray diffractometer which uses a Cu tube as X-Ray source with a wavelength λ=1.54$\mathring{A}$ (which corresponds to the characteristic lines K_{α_1} and K_{α_2} which are due to the L $\rightarrow$ K shell transition). The generated X-rays are reflected or diffracted in the sample and are collected in a scintillator detector. Both, the sample and the detector are mounted on goniometers which allow to vary the relative angle between them. As a result, the intensity of the collected beam is studied as a function of these angles.

XRD and XRR scans of this thesis have been done in the standard θ-2θ configuration,

in which the sample and the detector are moved such that the incident and the scattered waves are perpendicular.

2.2.1 X-Ray Reflectivity (XRR)

XRR technique has been used to obtain the thickness of the films. In this case the observed oscillations peaks are due to an interference between the film surface and the film-substrate interfaces. From the period of the observed oscillations, the thickness can be determine.

Fig. 2.8 shows the XRR scans obtained for Ni films deposited for different sputtering times (different thicknesses). As can be seen, by increasing the deposition time, the period of the oscillation decreases. In order to obtain the film thickness t from these data, the positions of the minima have to be adjusted to the modified Bragg's Law (that takes into account the change in the index of refraction) [31]:

$$sin^2(\theta) = \left(\frac{n\lambda}{2t}\right)^2 + 2\delta \tag{2.1}$$

where θ is the angle defined by the sample axis and the X-rays, λ is the X-Rays wavelength, n is an integer number, t is the thickness of the sample and 1-δ is the real part of the index of refraction (n). The obtained thickness is indicated inside each graph.

Finally, from a linear fit of the thickness *v.s.* the deposition time, we can obtain the growth rate, which in this case corresponds to 1.52 $\mathring{A}$/s.

Similar analysis have been performed to obtain the growth rate of every material studied in this thesis.

2.2.2 X-Ray Diffraction (XRD)

XRD scans have been performed to study the crystallinity of the films. Nb, Co, Pd and Ni films are polycrystalline films. In the case of the Fe nanotriangles studied in chapter 7, XRD scans confirm the single-crystal structure of the Fe films grown on top of MgO substrates [32].

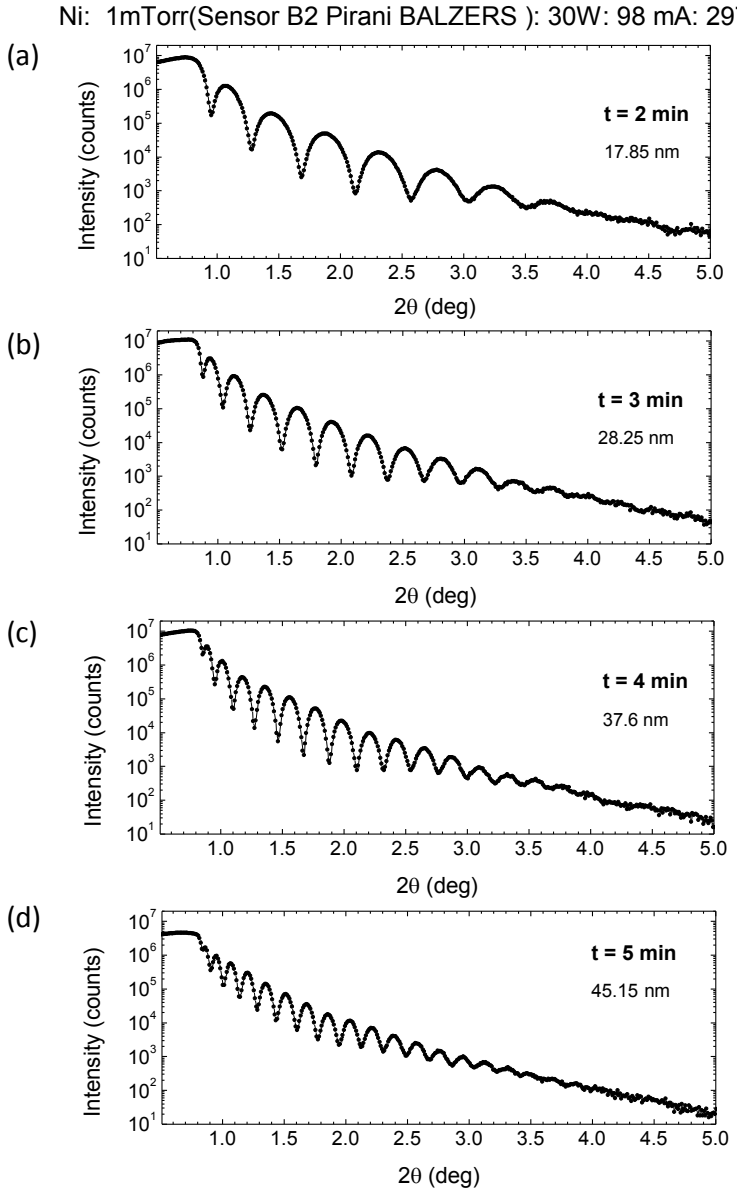

Figure 2.8: Reflectometry scans of Ni films grown on top of Si substrates at 30 W and 1 mTorr of Ar pressure for different deposition times: (a) 2 minutes, (b) 3 minutes, (c) 4 minutes and (d) 5 minutes.

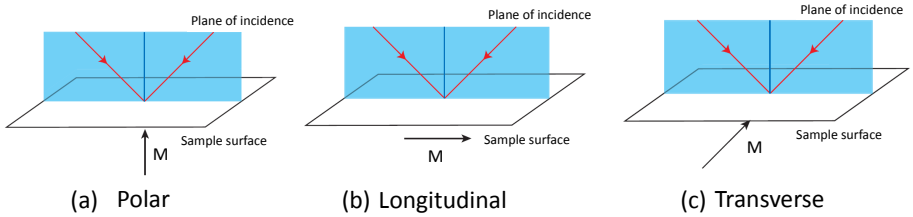

Figure 2.9: Geometries used in MOKE measurements: (a) polar, (b) longitudinal and (c) transverse.

2.3 Magnetic Characterization

Magnetic characterization has been performed by using vibrating sample magnetometer (VSM) and a magneto-optical Kerr effect setup with a focused beam (NanoMOKE). In addition, micromagnetic simulations have been used to complement the informations provided by the experimental techniques. In this section, this techniques will be explained.

2.3.1 Magneto-Optical Kerr Effect (MOKE)

Magneto-Optical Kerr Effect is based on the change of the polarization state of the light by reflection from a magnetized surface.

Three different geometries can be used in the MOKE measurements which arise from the direction of the magnetization with respect to the plane of incidence and the sample surface (see fig. 2.9): (i) polar geometry where the magnetization is perpendicular to the sample surface; (ii) longitudinal geometry where the magnetization is parallel to the sample surface and the plane of incidence; (iii) transverse geometry where the magnetization is parallel to the sample surface and perpendicular to the plane of incidence. Polar and transverse MOKE produce a rotation of the axis of polarization, whereas transverse MOKE produces a changed in the reflected intensity. If M_z is almost 0, polar contribution can be neglected.

The experimental set-up for the MOKE measurements is as follows:

A HeNe laser (λ=632.8 nm) laser is used to generate a intensity stabilized p-polarized beam. This beam is focused in the sample by focusing lens creating a spot size 30

μm diameter. The spot can be localized on the array using a CCD camera. The incident angle is set to 45° with respect to the sample normal, which is typically used to probe M_x in the longitudinal geometry. After reflection, a beam splitter is used to divide the reflected beam of light in two. One of them goes through a linear polarizer that extinguishes the p-polarized component, so only the s-polarized light passes through. This s-polarized beam is focused onto a photodiode that produces a voltage proportional to the incident light intensity. This intensity, as is produced by a rotation of the polarization, is proportional to the M_x. The other beam is focused on another photodiode that measures the intensity of the p-polarized reflected beam. In this case, the signal is proportional to the M_y component.

The sample is placed in a quadrupolar electromagnet that allows applying fields up to 1000 Oe. So, both M_x and M_y components of the magnetization can be measured as a function of the applied magnetic field.

2.3.2 Vibrating Sample Magnetometer (VSM)

Fig. 2.10 shows an schematic of a vibrating sample magnetometer. The sample is mounted on a non-magnetic rod which is attached to a vibration unit. This unit oscillates the sample at a frequency of f=83 Hz and 1 mm amplitude. The sample is centered at the geometrical center of the gap between the poles of an electromagnet. In our case, we use a water cooled electromagnet capable of applying constant fields up to 2.2 Tesla. In the inner part of the electromagnet, the pick-up coils measure the induce voltage.

Vibrating sample magnetometer is based on the flux change in a coil induced by a vibrating magnetic moment. By using a calibration standard, the proportionality constant between the induced voltage and moment can be calculated, which in our case is ∼10mV/emu. The system sensitivity is $\sim 10^{-5}$ emu, and the sample can be rotated, so angular dependence studies are possible.

2.3.3 Micromagnetic simulations: OOMMF

Magnetic simulations presented in this thesis are based on micromagnetism which was originally introduced by Brown in 1963 [33]. Micromagnetism central idea is the

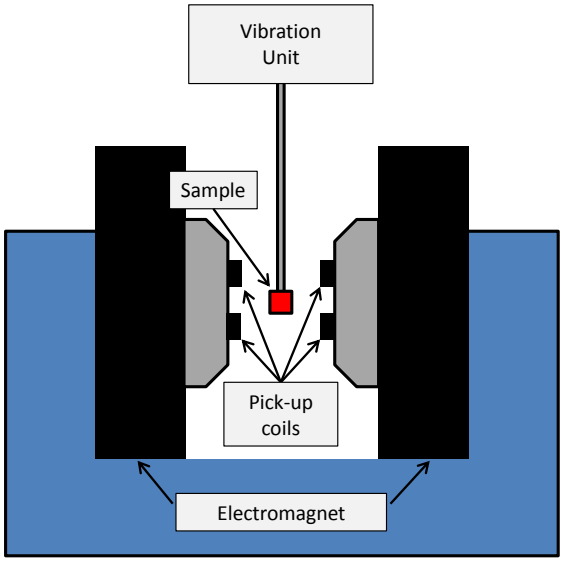

Figure 2.10: Schematic of a vibrating sample magnetometer.

transition from individual spins to a continuous magnetization inside a given volume or cell. Each cell is considered as an elementary magnetic moment and represents a small volume of the magnetic body where the average magnetic moment varies smoothly (so magnetization can be considered constant inside each cell). In this model (continuous approach), the free energy E is the sum of various energy contributions [34, 35]:

$$E = E_{ex} + E_{An} + E_{Mag} + E_{Zeeman} \tag{2.2}$$

where E_{ex} is the exchange energy, E_{An} the magnetocrystalline anisotropy energy, E_{Mag} the magnetostatic energy and E_{Zeeman} the Zeeman energy.

From the first-order variation of the free energy, an effective field (H_{eff}) that acts on each magnetic moment ($\overrightarrow{M}$) can be obtained:

$$\overrightarrow{H_{eff}} = -\frac{1}{\mu_0}\frac{\delta E}{\delta \overrightarrow{M}} \tag{2.3}$$

The dynamics of the magnetization inside each cell is then described by the Landau-Liftshitz-Gilbert (L-L-G) equation:

$$\frac{d\overrightarrow{M}}{dt} = -\gamma\overrightarrow{M} \times \overrightarrow{H_{eff}} - \frac{\gamma\alpha}{M_s}\overrightarrow{M} \times (\overrightarrow{M} \times \overrightarrow{H_{eff}}) \tag{2.4}$$

where γ is the gyromagnetic ration, M_s the saturation magnetization and α the phenomenological damping parameter. The first term corresponds to a precessional movement of the magnetization around the effective magnetic field. The second term is the relaxation term which drags the magnetization into the direction of the effective field [34].

Micromagnetic simulations have been performed using the Object Oriented MicroMagnetic Framework (OOMMF) open source software developed at the National Institute of Standards and Technology (NIST)[36]. In addition, the open source vector graphics editor Inkscape [37] was used to design the magnetic sample (geometry and dimensions) that will be used as the input for the OOMMF simulations.

The sample is discretized in a 2 dimensional regular mesh by OOMMF. The cell dimensions of the grid have to be determined and should be smaller than the exchange length [35] (on which the exchange interaction is prevalent) - so magnetization can be considered constant inside each cell. Typical values of the cell size are around 10 nm, although it depends on the material and the size of the simulated sample. Material parameter such as M_s, exchange constant, anisotropy or the damping coefficient should be specify as well.

To initialize the simulation, an initial M configuration and an external magnetic field is considered. Then, the effective field is calculated and introduced in the L-L-G equation which is numerically solved. The final stable configuration is given by the minimization of the free energy and is used as the initial state for the next considered magnetic field. As a result of the simulation, the magnetization and the value of the different energy terms can be obtained as a function of the applied magnetic field.

During this thesis, micromagnetic simulations have been used to provide a useful complement to the experimental results obtained by the magnetometer techniques.

2.4 Experimental set-up for low temperature characterization

Fig. 2.11(a) shows a general view of the experimental set up used to transport characterization. In fig. 2.11(b), a schematic diagram illustrates the main parts of this experimental set-up:

- A **helium liquifier** provides the liquid helium that will be transfered to a **cryostat** through a **He dewar**. The cryostat is connected to a **recovery system** that will recover the evaporated helium directly from the cryostat and store it. The recovered helium gas will be liquefied again to be reused.
- A **nitrogen liquifier** is used to obtain liquid nitrogen to precool the cryostat.
- The sample, mounted in sample holder, is introduced in the cryostat and connected to the required **instrumentation** to perform the measurements. These will be controlled by a **PC** through the **Labview software**.

2.4.1 Helium Liquefier System

A QuatumCONDENSER Helium Liquefier System of Quantum Technology Corporation is used to produce liquid helium. This system consist of different helium circuits:

- Closed loop refrigeration circuits: closed helium circuits where high purity helium gas is cooled down by expansion/compression cycles.
- Helium supply circuit: an open circuit to provide helium gas to liquefy by thermal contact with the closed circuits.

Closed loop refrigeration circuits

Closed loop refrigeration circuits provide the cooling power to liquify helium in three stages.

The first two stages are based on the Gifford-McMahon (GM) cycle and are linked together in a cold head with a single displacer-regenerator as shown in fig. 2.12(a). In

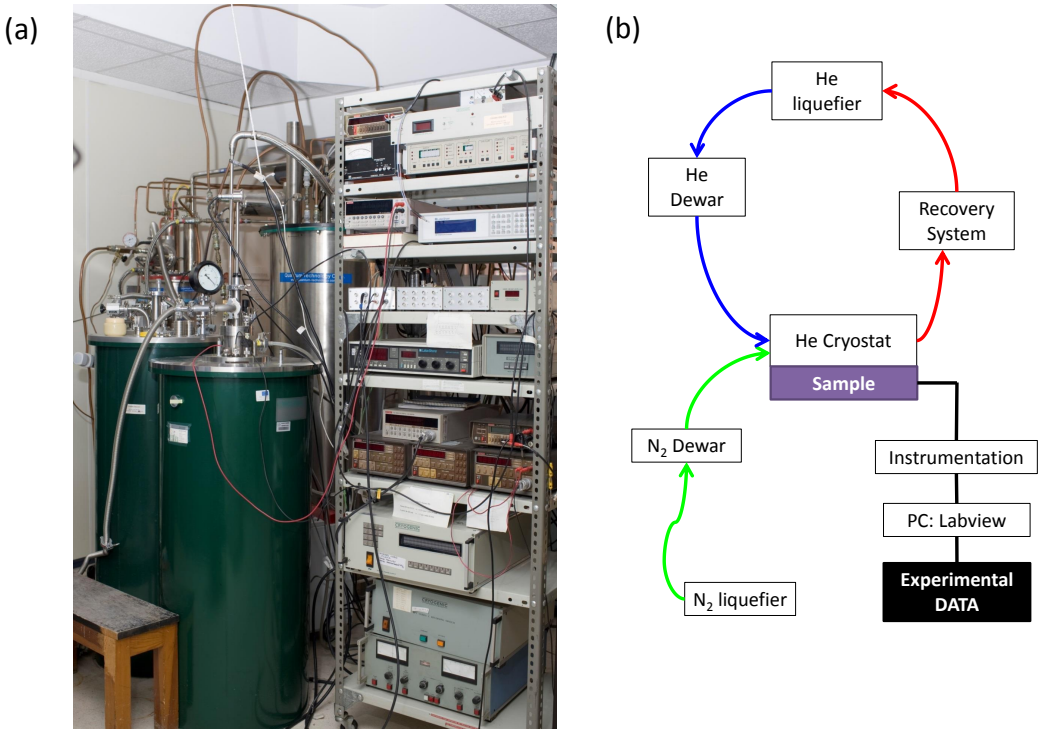

Figure 2.11: Picture (a) and schematic (b) and of the experimental set-up to perform the low temperature characterization.

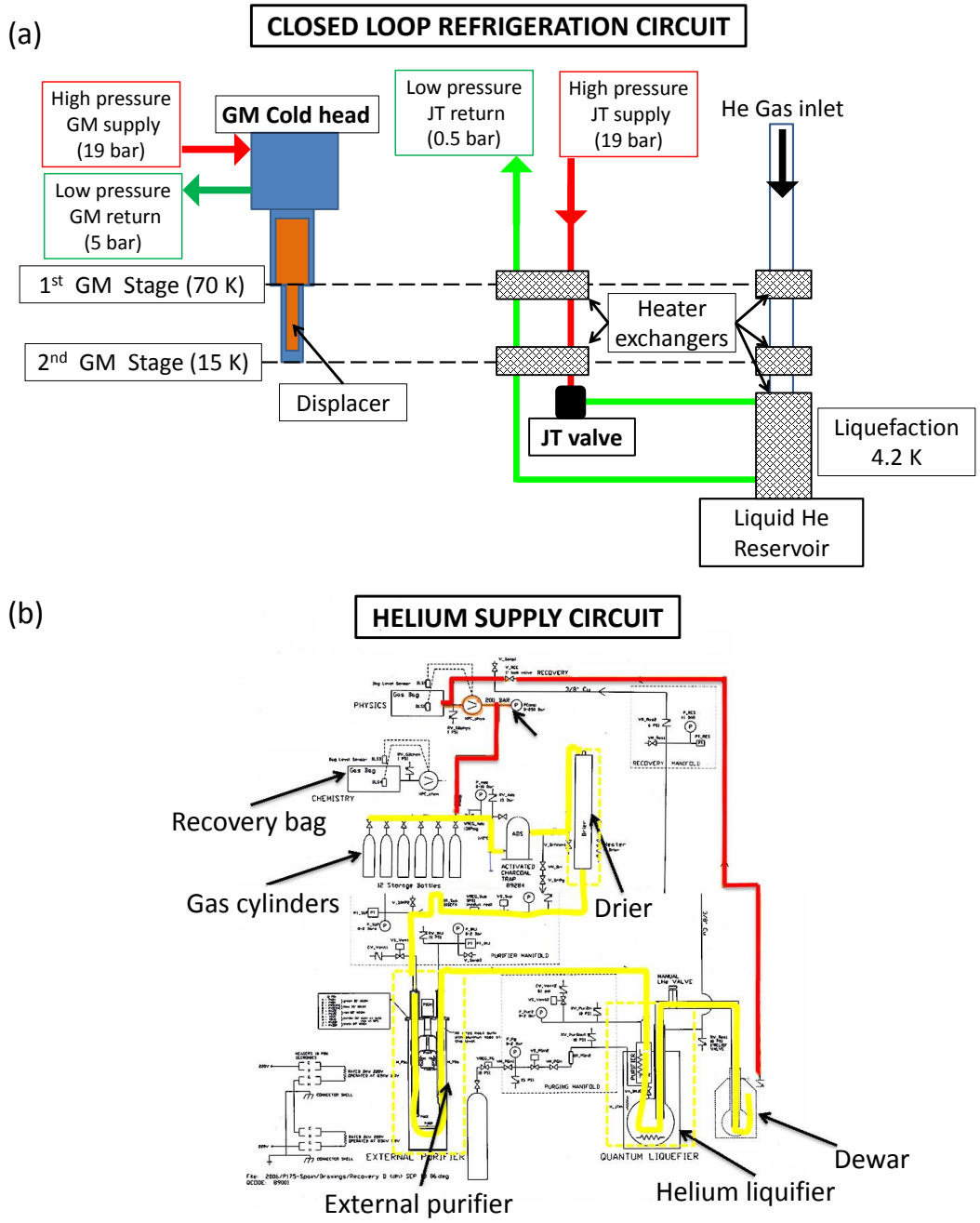

Figure 2.12: (a) Schematic of closed loop refrigeration circuits showing the two GM stages and the JT stage and the corresponding temperatures. Different colors indicate different gas pressures.(b) Schematic of the Helium supply circuit, red lines indicate the recovery circuit and yellow lines indicate the purification and liquefaction circuits.

this cycle, the helium gas pressure cycles isothermally from 19 bar to 5 bar. First, the compressed helium supply valve is opened and high pressure helium gas at room temperature is flowed into the cold head. As the high pressure gas is admitted into the cylinder, the displacer moves upwards, forcing the gas to pass through the regenerator. Then, the high pressure valve is closed and the return valve is opened. In this line, pressure is at approximately 5 bar, so the gas expands through the regenerator into the return line. This is an isothermal expansion so heat is taken up from the system, producing the useful cooling power. Finally, the displacer is forced downwards to push any remaining helium gas through the regenerator and into the return line to the helium compressor. The return valve is closed and the helium is again compressed in the compressor for the next cycle. In the first stage, the operating temperature is 70 K and in the second one, the temperature is 15 K.

The third stage of the refrigeration is a Joule-Thomson (JT) stage. The JT cycle is based on an adiabatic expansion through a valve which is insulated so that no heat is transferred during the process. The Van der Waals equation predicts that the actual behavior of a gas upon being throttled depends in large part on the molecular parameters. Actually, an inversion temperature (T_i) is defined for each gas; below this temperature, the gas cools when it adiabatically expands. In our system, in order to precool the helium below the inversion temperature, the gas at 17 bar is cooled to 15 K by the first two GM stages. Then, it expands through the JT orifice and produce a cold mixture of gas and liquid at 0.5 bar. This mixture provides cooling for liquefaction and for precooling the incoming high pressure gas (see fig. 2.12(a)).

Helium supply circuit

A continuous flow of helium gas is provided to the system to be liquified. Fig. 2.12(b) shows a diagram of this circuit. Red lines indicate the recovery circuit whereas yellow lines indicate the purification and liquefaction circuits.

Recovery system

The cryostat is connected to a system designed to recover the evaporated helium (red line in fig. 2.12(b)) . A recovery line conects the cryostat to an atmospheric pressure

recovery bag. This line is preferably made of copper, so helium temperature is increased before getting into the recovery bag. The bag is made of a rubber like material which is designed to minimize the permeability for both H_2O and Air which would contaminate the helium.

Two sensors control the compressor on/off operation. The helium gas is exactred from the bag, pressurized to 135 bar and stored in the gas cylinders. To avoid overfilling, the first sensor turns the compressor on when certain height is reached. When the height of the bag is decreased below a certain level, where a second sensor is installed, the switch turns the compressor off to avoid vacuum in the bag which could lead to contamination.

The recovered helium stored in the cylinders will be fed back into the liquefier. Despite the recovery system, part of the helium is lost by purging lines or during the measurements (the helium that cools the sample is evacuated through a roughing pump), so, eventually, a new charge of gas or liquid helium is necessary.

Purification and liquefaction circuit

To avoid contamination, that would freeze blocking the system, the helium liquifier includes a purification system. First, the inlet gas passes through a drier where H_2O is trapped. Later, in an external purifier the helium is cooled down to 40 K and forced to pass through a deposit of molecular sieve that eliminates possible air impurities.

Finally, the helium is transferred into the liquifier. First, the gas is precooled to 70 K and 15 K by thermal contact with the first and second GM stages. Then, by thermal contact with the JT return gas in a heat exchanger, it is liquefied (see fig. 2.12(a)). The liquid helium is collected in the internal reservoir, where a transfer line connected to a manual valve allows transfering the helium to an external dewar.

2.4.2 He cryostat

To perform the low-temperature magnetoresistance measurements, a 2 Tesla cryostat and a 9 Tesla cryostat have been used (see fig. 2.11(a)). The principal features of the 9 Tesla cryostat are shown in fig. 2.13 and listed below:

- Helium reservoir

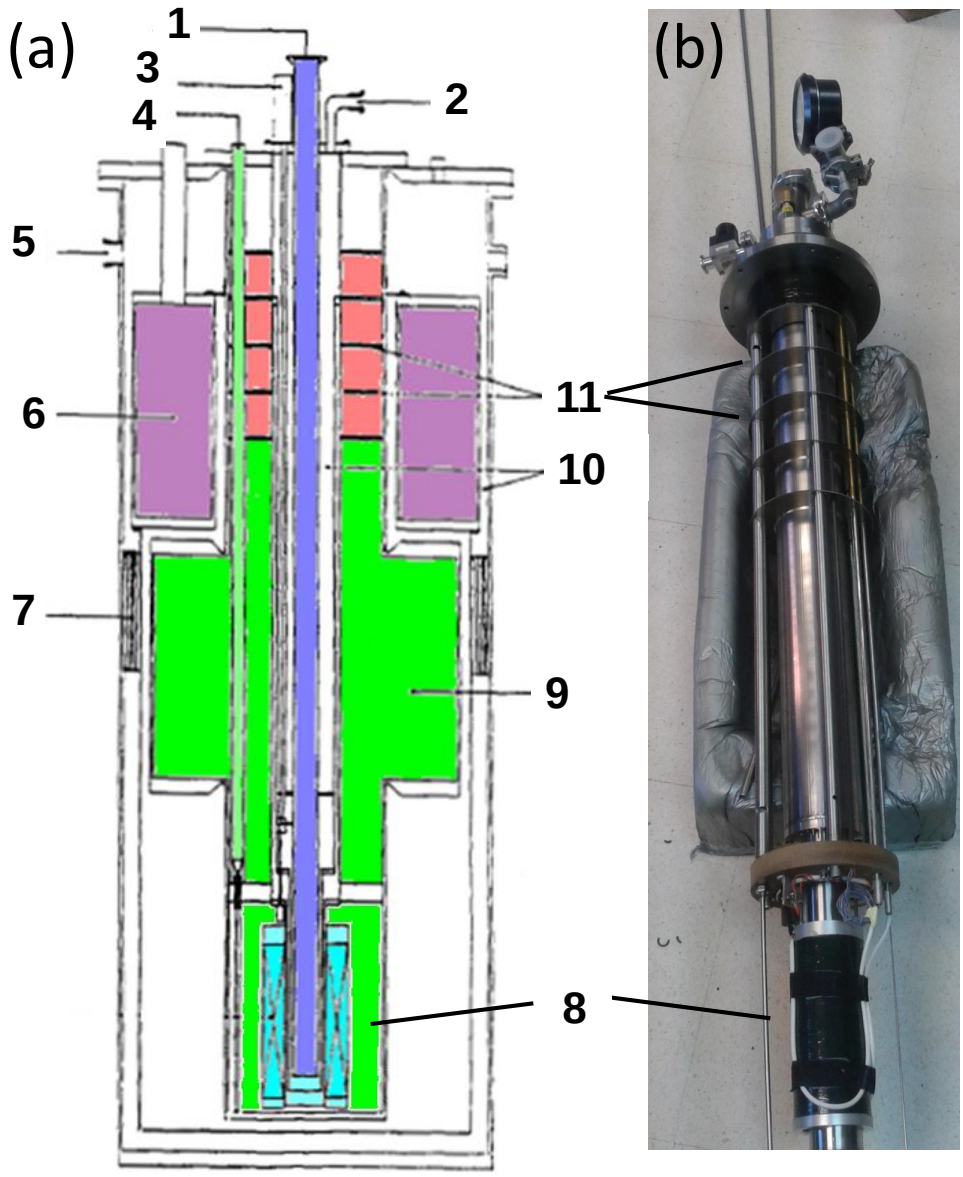

Figure 2.13: (a) Diagram of the 9 T cryostat. (b) Image of the variable temperature inset of the cryostat. Numbers indicate: 1. Sample space; 2. Vacuum sealed valve; 3. Needle valve; 4. Port to the vacuum helium tube; 5. Overpressure relief valve; 6. Nitrogen reservoir; 7. Radiation shield; 8. Superconducting magnet; 9. Helium reservoir; 10. Vacuum space; 11. Radiation blaffles.

- Nitrogen reservoir
- Vacuum space
- High purity aluminium radiation shield
- Over-pressure relief valve
- Radiation Baffles
- Heaters and thermometers
- Superconducting 9T Magnet
- Helium Level Gauge
- Needle valve from the helium reservoir to the sample space

Superconducting solenoid

Magnetic field is generated by a superconducting magnet in each cryostat. One of them is designed to produce magnetic field up to 2 T, the other one up to 9 T. Both magnets are composed of a single coil made from NbTi wires on an aluminium former. As can be seen in fig. 2.13(b), it is cast in epoxy resin to eliminate wire movement during energization. To energize the coil a Keithley 2420 Current Source is used for low currents (up to 3 A) and a Cryogenic SMS120C 4Q 20B DC power supply is used for high currents (up to 80 A).

The magnet is wired with a superconducting switch connected in parallel across the magnet and wired to the input/output current terminals. A heater wound into the switch enables this to be resistive or superconducting. This heater is controlled by the DC power supply and controls whether the superconducting magnet is in the persistent mode or not:

When the heater is enable, the switch becomes resistive and the applied current goes from the power supply to the non-resistive coil (the superconducting solenoid). In this operation mode, as the current coming from the power supply is increased or decreased, the magnetic field is changed (see fig. 2.14(a)). Once a certain magnetic field is reached, the magnet can work in the persistent mode. In this mode, the switch

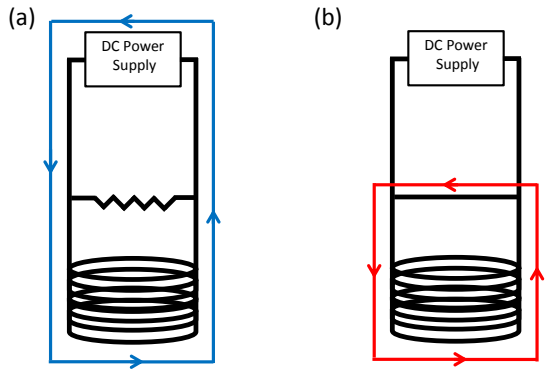

Figure 2.14: Schematic of the superconducting solenoid, DC power supply and the superconducting switch circuit in the non-persistent (a) and persistent mode (b).

is cooled down and becomes superconducting. Current from the magnet will begin to circulate through the switch and the power supply current can be ramped to zero keeping constant magnetic field. This mode is used to perform measurements at constant magnetic field (see fig. 2.14(b)).

Cooling down the cryostat

1. **Evacuation.** Sample space and vacuum space should be evacuated before cooling down the cryostat. A turbo pump is used to evacuate the insulating vacuum space. The vacuum in this part should be set in the 10^{-5} Torr range to ensure good insulation. Once this pressure is reached, pumping is stopped and the vacuum space is isolated. Additionally, the sample space is connected to a rotatory pump which evacuates the sample space until the cryostat is warmed up. This will avoid air condensation in the sample space.

2. **Precooling.** The cryostat should be precooled with liquid nitrogen before transferring the liquid helium. Nitrogen should be introduced slowly to the bottom and the cryostat should be filled to the top of the helium reservoir. This ensures the dominant thermal mass is completly pre-cooled and will minimise losses during the liquid helium tranfer. The external nitrogen reservoir should be also filled to ensure rapid cooling of the shield and superinsulation. Precooling should be done for a period of at least four hours (usually eight hours is enough).

3. **Removal of liquid nitrogen.** Liquid nitrogen is eliminated by pressurizing the helium vessel with dry nitrogen or helium gas and forcing the liquid out through an appropriate pipe. Usually, the extracted liquid nitrogen is transferred to the external nitrogen reservoir.

   The residual liquid nitrogen in the helium reservoir has to be vaporized using the heater located in the base of the helium reservoir. This heating process is performed until the temperature of the helium reservoir base is raised to 80 K.

   It is very important to eliminate all the liquid nitrogen prior to starting the helium tranfer. Any residual nitrogen will freeze, causing a blockage of the helium transfer tube.

4. **Liquid helium transfer**

   After the nitrogen has been purged out, the liquid helium can be introduced. Helium transfer should not be too rapid in order to ensure efficient cooling of the cryostat. The onset of liquid accumulation can be detected by the themometer on the base of the reservoir, which will settle at a stable 4.2 K. A liquid helium level gauge indicates the level of the accumulated helium. The exhaust line of the cryostat is connected to the recovery line only when the purity of the recovered helium is ensured.

   The transferred helium is measured by a helium level gauge which consists of a fine wire made of NbTi which has a critical temperature higher than the boiling point of liquid helium. The voltage developed across the sensor is directly proportional to the length of the conductor in the helium vapor, so this voltage drop can be converted to the equivalent helium depth.

2.4.3 Transport Measurements

Electrical transport measurements have been performed to study the superconducting properties of the hybrid samples.

Standard four probe measurements are performed by using the cross-shaped bridge shown in fig. 2.1-4. This bridge consists of two 40 μm paths for current injection and

four 8μm paths for measuring the voltage drop. This geometry allows characterizing the sample in two perpendicular directions.

The sample is mounted in a variable temperature probe that will be inserted into the cryostat. There are different probes available in the laboratory, among them, fig. 2.2 shows the rotator probe which allows rotating the sample with respect to the magnetic field.

The sample probe is connected to a 224A programmable DC current source to inject currents ranging from 0.1 μA to 3 A. The voltage drop is measured by means of a 182 Digital Nanovoltmeter. For ac measurements, a Lakeshore 140 AC current source with variable frequency is connected to the probe.

Temperature control

Most of the measurements in this work are made at constant temperature very close to T_c. A small variation in the temperature will dramatically change the superconducting properties, so it is crucial to keep the temperature very stable during the measurement. Both cryostats allow a precise temperature control between 1.6 K and 400 K: cooling is done by a constant flow of helium in the sample space; heating is done by heater exchangers externally controlled.

Two valves control the helium flow in the the sample space. A needle valve regulates the flow of helium that enters from the main helium bath to the sample space. Another valve, located between the sample space and the external rotatory pump, controls the helium gas exhausted from the sample space. These valves control the pressure in the sample space which is usually set between 1 and 10 mTorr.

Once the gas flow has been set, the temperature can be regulated by controlling two different heaters. The first one is placed in the needle valve and controls the temperature of the He gas that enters in the sample space. An extra heater, located in the sample holder, directly controls the sample temperature. Temperatures are read by calibrated Cernox sensors that are attached to both heat exchangers.

A 340 LakeShore Temperature Controller reads the temperature and controls the heaters to establish a certain temperature (set point). This is done by proportional-integral-derivative (PID) control loops. This algorithm calculates the heater output

based on the difference between the set-point temperature ($T_{set-point}$) and the feedback reading of the sample temperature (T_{sample}). There are three variable terms: P or proportional term, I or integral term and D or derivative term. The PID equation is:

$$Heater - Output = P\left[e + I\int(e)dt + D\frac{de}{dt}\right] \tag{2.5}$$

where the error e is defined as e=$T_{set-point}$-T_{sample}.

An appropriate choice of the PID settings is crucial to control and establish a certain temperature. The sample temperature can be controlled with 1 mK accuracy.

Data acquisition

To carry out the transport measurements, different electrical devices have to be controlled and synchronized at the same time: temperature controller, power supply of the superconducting magnet, ac/dc current source and nanovoltmeter. For this aim, every device is connected to the computer by parallel IEEE ports and controlled by Labview. Labview (Laboratory Virtual Instrument Engineering Workbench) is a graphical language from National Instruments that is used for instrument control and automate data acquisition. LabVIEW programs are called virtual instruments (VIs) and contains a front panel (the interface to interact with the VI) and the block diagram (the code that controls the program).

To control every device and perform different transport measurements, several VIs have been created. Among them:

- **R*vs.*T:** at constant current and magnetic field, voltage is read as the temperature is ramped up or down.
- **V*vs.*I:** at constant temperature and magnetic field, voltage is read as current is ramped up.
- **R*vs.*H:** at constant temperature and current, voltage is read as magnetic field is ramped up or down.
- **V_{dc}*vs.*I_{ac}:** at constant temperature and field, voltage is read as the ac current is ramped up.

3

Origin of the commensurability effect: Vortex pinning *vs.* Superconducting wire network

3.1 Introduction

As explained in section 1.3.2, in superconductors grown on top of an ordered array of nanodots, minima in the resistance appear for certain magnetic field that satisfies that the vortex lattice density equals a fractional or interger number the pinning center density. These minima have been explained as an enhancement of the vortex pinning when both lattices are commensurated [8, 38] and it can be observed as peaks in the critical current as well [20, 39].

It has been shown that this effect is enhanced when the size of the pinning site is of the order of the coherence length [20]. Since typical values of the coherence length are in the range of tens and hundreds of nanometers (depending on the temperature and material [5]), electron beam lithography is the ideal tool to define these arrays. The

main disadvantage of this type of lithography is that it is very difficult to fabricate large areas of an array due to problems with the beam stability and alignment issues.

For this reason, this effect is usually studied by means of magnetotransport measurements. This technique has the advantage that the size of the sample is only limited by the size of the bridge that is used to perform the transport measurements (usually in the order of microns). However, in transport measurements, only experiments near T_c can be performed, so that only low currents are applied and self-heating problem is avoid.

As was shown in the introduction (section 1.2), coherence length (ξ) diverges as temperature (T) approaches the critical temperature (T_c):

$$\xi(T) = \xi(0)\frac{1}{\sqrt{1 - T/T_c}}, \tag{3.1}$$

Since transport measurements are performed near T_c, ξ is usually in the order of tens or hundreds of nanometers, which is similar to the distance between the pinning sites.

When the width of the superconducting strips between the holes (W) is of the order of magnitude than the coherence length ($\xi \simeq$W), a superconducting wire network is formed [20, 40–44]. Superconducting networks exhibit maxima in the critical temperature at the matching fields, which is known as the Little-Parks effect [45]. This effect is based on the suppression of the T_c caused by the superconducting currents that appear to preserve the fluxoid quantization at non-integer values of the matching field [5]; when the external magnetic field generates an integer number of fluxons per hole, the free energy is minimized and a maximum in T_c is obtained [45]. As is shown in fig. 3.1(a), a maximum in T_c induces a minimum in the resistance (as R(H) is measured a constant temperature (T_0 in fig. 3.1(a)). Fig. 3.1(b) shows a typical 2-dimensional array of superconducting junctions and fig. 3.1(c) the obtained magnetoresistance curve for different temperatures [46]. Maxima observed in the critical current at the matching fields can be explained following the same reasoning.[44].

Transport measurements are performed near T_c where the coherence length (ξ) is of the order of magnitude than the distance between the nanodots (W), it is not clear the origin of the features observed in the resistance and in the critical current at the

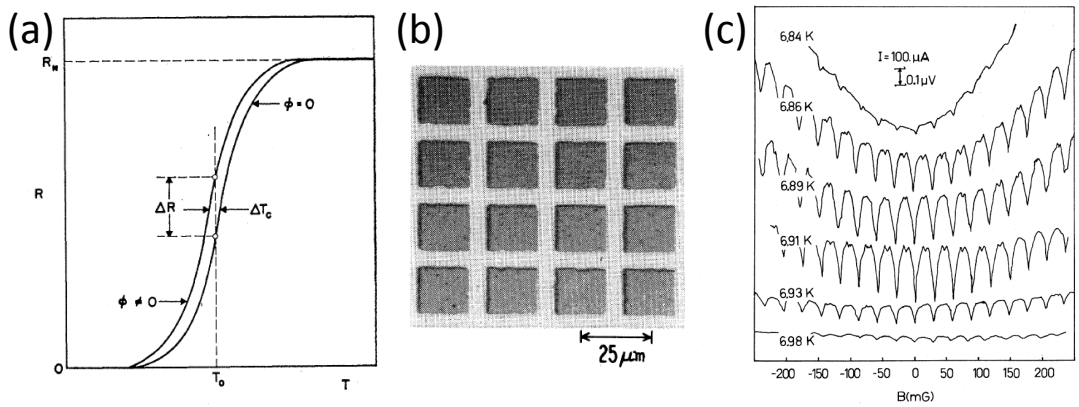

Figure 3.1: (a) Typical variation of the resistance with temperature of a thin cylindrical superconductor showing how a small change in T_c due to the Little-Parks oscillations induces a change in resistance as well (from Parks *et al.* [45]). (b) Image of the Pb-Cu-Pb proximity effect junction array measured in (c), which shows the magnetic field dependence of the resistance within the resistive transition (from Tinkham *et al.* [46]).

matching fields [42]. To clarify the origin of the commensurability effect, temperature should be decreased until ξ <<W when the superconducting wire network regime is not satified. Due to current limits to avoid self-heating, a complete study at low temperatures can not be performed by transport measurements.

To study the vortex lattice dynamics at lower temperatures, magnetization measurements M(H) and χ(H) are performed. In this case, no currents are applied to the sample and low temperatures can be achieved. However, in order to obtain enough signal, large areas of the sample are needed. This technique has been used to characterize superconducting properties in thin films with arrays of antidots [7, 43, 47]. In this case, an overall enhancement of the width ΔM of the hystereis loop is observed as a consequence of the pinning enhancement in the perforated superconducting film compared to the plain film. In addition, step-like features are observed at the matching fields.

Anodized aluminum oxide membranes are the ideal substrates to grow large areas of patterned hybrids, even though only triangular lattices can be fabricated. Superconducting samples grown on top of these membranes have been studied as well. Welp *et al.* [48] fabricated large areas of perforated Nb films using this type of membranes with

holes of 45 nm diameter and 100 nm period of the triangular lattice. Due to the small size of the features, they obtained commensurability effect down to 4.2 K and 0.9 T. In addition, they reported an oscillatory behaviour of the phase boundary (T_c(H)) which is a direct consequence of the fluxoid quantization and it has the same origin than the Little-Parks oscillations (since the coherence length even at such low temperatures is of the same order of magnitude that the pattern period).

A crossover from vortex pinning to superconducting wire network has already been reported in superconducting films with arrays of antidots, both in magnetotransport measurements [49] and magnetization measurements [43]. Since this crossover occurs when $\xi \simeq$W, it can be induced by decreasing distance between antidots (W) or increasing the coherence length ξ by increasing the temperature.

The aim of this chapter is to clarify the origin of the minima observed in the R(H) curves and the peaks observed in the I_c(H) on superconducting films grown on top of nanodot arrays. For this aim, a complete study over a wide range of temperature will be performed. In addition, at low temperatures, random intrinsic pinning competes with the periodic pinning,. This fact makes that the commensurability effect may not be observed [18, 39, 50].

3.2 Sample description

As mentioned before, in order to have enough signal in magnetization measurements, a larga sample is needed. Arrays of magnetic Ni nanodots have been fabricated on Si (100) substrates using electron beam lithography and lift-off technique in combination with DC magnetron sputtering. Both, good stability of the electron beam and good alignment have allowed us to defined large areas of this array (3 mm x 3 mm) without stitching. The Ni nanodots dimensions are 200 nm diameter and 40 nm thickness. In this sample, Ni dots are arranged on a square lattice of 400 nm side.

Finally, a 100 nm thick Nb film was deposited by DC magnetron sputtering on top of the arrays, forming the magnetic / superconductor hybrid samples.

3.3 Experimental results

3.3.1 Transport measurements

Magnetotransport measurements were performed following the usual procedure (section 2.4). Fig. 3.2(a) shows the minima in resistance obtained at different temperatures ranging from 0.97T$_c$ (brown dots) to 0.99T$_c$ (blue dots). Fig. 3.2(b) shows the magnetic field position of the resistance minima *vs.* the order of the minima n (H=nH$_{match}$).

From the linear fit shown in fig. 3.2(b) the spacing between minima is obtained, which corresponds to the experimental value of the matching field: $\Delta H_{match_{exp}} = 124$ Oe. This value is in good agreement with the theoretical matching field calculated from the pinning density for a square array of 400 nm side (a=400 nm) [8]:

$$\Delta H_{match_{theo}} = \frac{\Phi_0}{a^2} = 129Oe, \tag{3.2}$$

As can be seen in fig. 3.2(a), decreasing the temperature, the upper critical field is increased and minima of higher order are observed. However, at such low temperatures, for small fields, the sample goes to the superconducting state and zero resistance is recorded in the measurement.

To observe minima at low matching fields, the temperature has to be closer to T$_c$. Fig. 3.3(a), show the R(H) curve obtained at 0.99T$_c$ for an applied current 1 mA. In this case, minima are observed up to n=2 (2H$_{match}$) and fractional minima for n=1/2 and n=3/2 (1/2H$_{match}$ and 3/2H$_{match}$) are observed as well [22, 51].

Fig. 3.3(b) and (c) show the dependence of the current *vs.* the applied magnetic field at 0.99T$_c$ for different voltage criterion (V$_c$ = 5·10^{-7} V and V$_c$ = 1·10^{-5} V, respectively). Fig. 3.3(b) is associated with the depinning current (current needed to set vortices in motion), whereas fig. 3.3(c), where a higher voltage criterion is used, vortices are already moving. In both graphs, peaks in the current and minima in resistance are observed at the same matching fields (compare fig. 3.3(a),(b) and (c)).

From these results, we can conclude that commensurability effect between the superconducting vortex lattice and the pinning array is observed in this sample for temperatures ranging from 0.99T$_c$ to 0.97T$_c$. The effect is revealed as minima in the

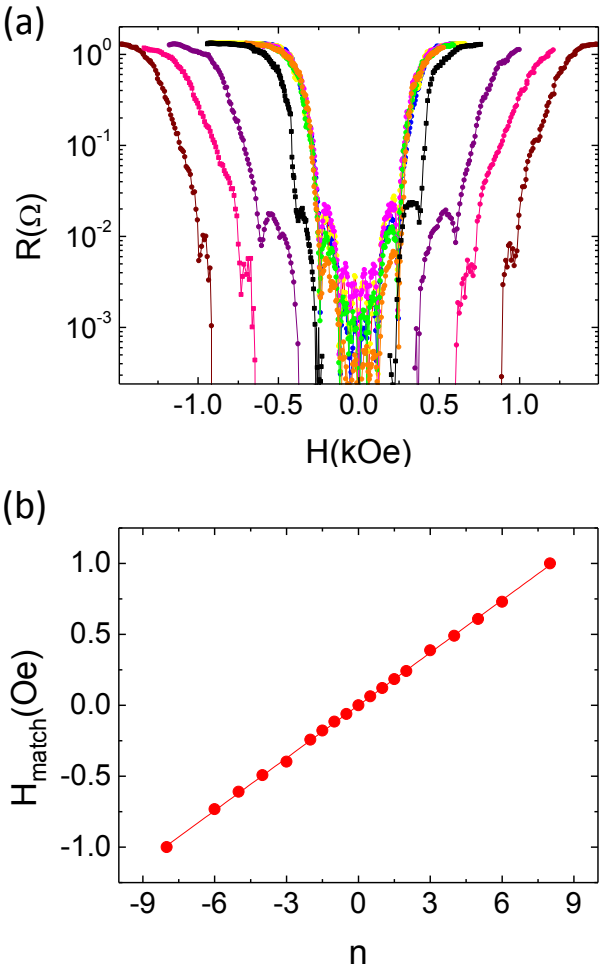

Figure 3.2: (a) Magnetic field dependence of the resistance for temperatures ranging from $0.97T_c$ (brown) to $0.99T_c$ (blue). (b) Dots show the magnetic field position of the resistance minima *vs.* the index number n. The red solid line is the linear fit to the experimental data.

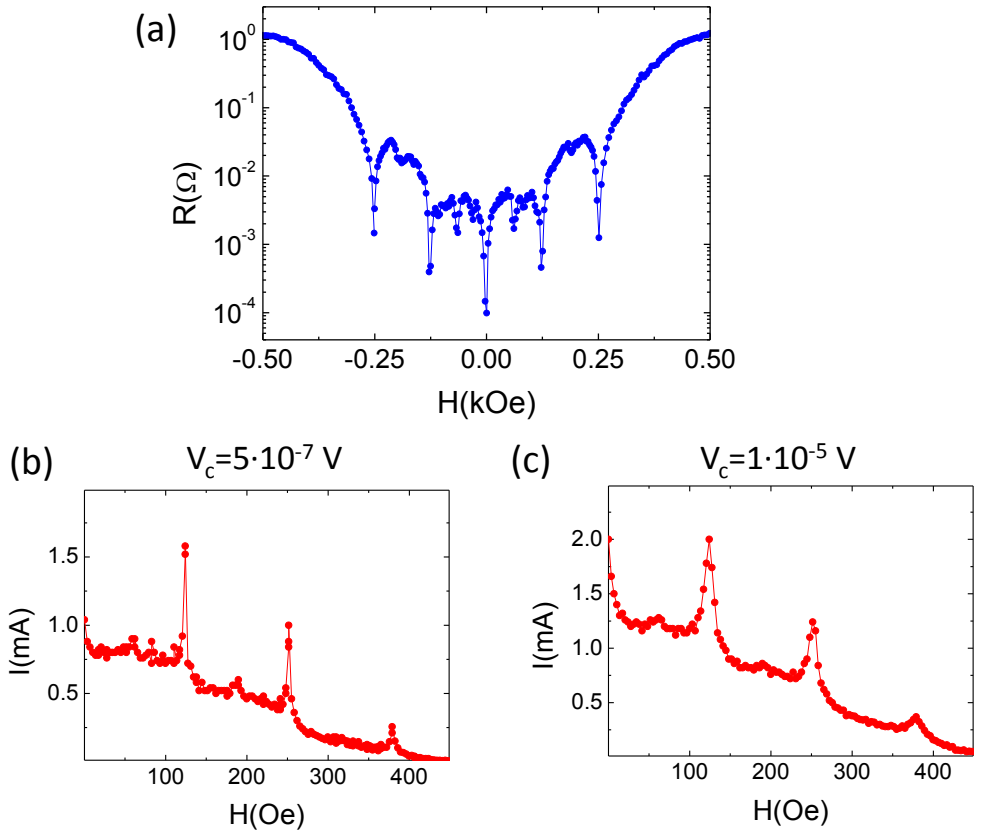

Figure 3.3: Magnetotransport measurements at $0.99T_c$: (a) Magnetic field dependence of the resistance for an applied current I=1 mA. Fig. (b) and (c) show the critical current as a function of the magnetic field obtained for a voltage criterion of $5{\cdot}10^{-7}$ V and $1{\cdot}10^{-5}$ V, respectively.

resistance and maxima in the critical current. In addition, we extract that this effect is present in this sample both in the static and dynamic regime of the vortex lattice.

3.3.2 Magnetization measurements

Ac susceptibility experiments were performed in a Quantum Design MPMS superconducting quantum interference device (SQUID) magnetometer with ac and dc magnetic fields applied perpedicular to the sample plane.

AC Magnetometry

Superconductor AC response

In AC magnetic measurements, small AC magnetic fields (h_{ac}) are superimposed on a DC field causing a time-dependent moment in the sample. The field created by this moment induces a current in the secondary coils that allows measuring the induced magnetic moment in the sample.

If small h_{ac} amplitudes are applied, the driving ac fields induces small currents that produce vortex oscillations inside the effective pinning potential wells. This regime is known as the linear regime (Campbell regime), where response is independent of the ac amplitude and small dissipation is obtained. In this regime, ac susceptibility measurements have been used to estimate the vortex pinning strength in superconducting films with arrays of antidots [52].

Our study will be performed on the nonlinear regime which is well described by the Bean critical state model [5]. In this case, the h_{ac} amplitudes are increased, larger forces drive the vortices and they are no longer localized in the pinning valleys. As a result, vortices can travel larger distances and dissipation is not negligible. The real part of the ac susceptibility χ' measures the shielding capability, so, as vortex mobility decreases (pinning increases), χ' tends to more negative values (up to -1 for perfect shielding, in the Meissner state). On the contrary, if the vortex lattices becomes more mobile, the ac field can penetrate in the sample easily and χ' tends to zero. The imaginary part of the susceptibility χ" provides information about the ac losses in the sample [7, 53].

Experimental results

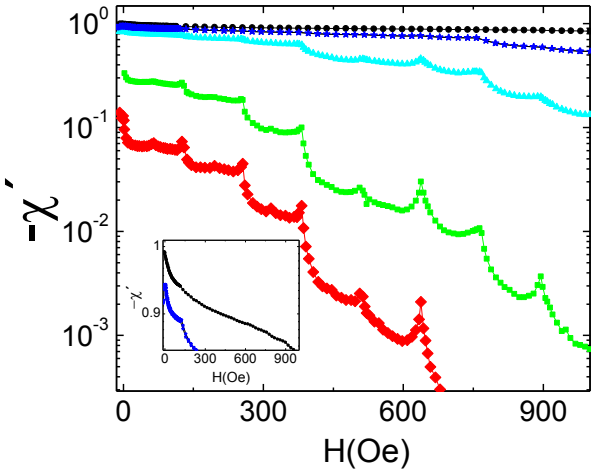

Figure 3.4: Ac susceptibility χ' as a function of the applied magnetic field for different temperatures:0.99T_c (red), 0.98T_c (green), 0.94T_c (cyan), 0.90T_c (blue),0.79T_c (black). Dips are observed at matching fields, however these features disappear for lower temperatures (inset: zoom-in to show that no features are observed at 0.79T_c).

In this work, we studied the magnetic field dependence of the real part of the susceptibility χ'. The applied ac field amplitude was h_{ac}=1 Oe and where the non-linear regime is observed and we can assume that the sample is in the critical state. Frecuency is set to f=1 kHz.

Fig. 3.4 shows χ' as a function of the applied dc field (H) for 0.79 $T/T_c < T <$ 0.99T_c. Peaks are observed at matching fields, which indicate reduced vortex lattice mobility, or equivalently, an increase in pinning. As shown in inset in fig. 3.4, these features at matching fields are smeared out at low temperatures. For temperatures close to T_c, peaks are observed at fractional matching fields for n=1/2, 3/2 and 5/2 (see red curve in fig. 3.4).

DC Magnetometry

DC magnetrometry has been performed as well. In this case, the sample is magnetized by a constant magnetic field applied perpendicular to the substrate and the magnetic moment of the sample is measured by a superconducting quantum interference device (SQUID) by measuring the currents induced in the superconducting pickup coils.

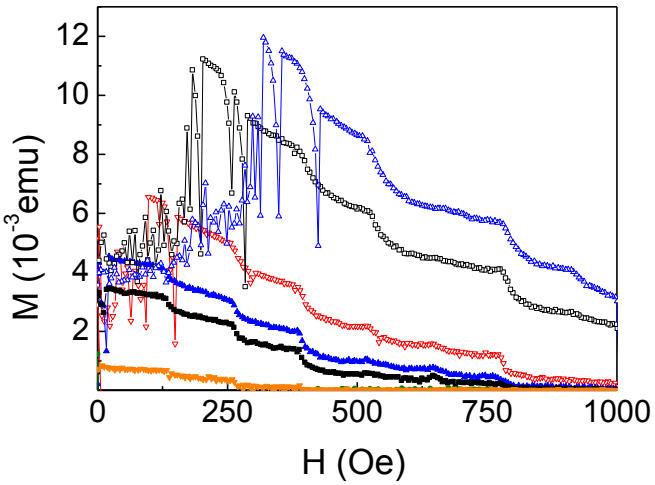

Figure 3.5: M(H) at different temperatures going from $0.78T_c$ (blue) to $0.94T_c$ (orange). Note that dips are observed in the magnetization at matching fields.

Magnetic field dependence of the magnetization is shown in fig. 3.5 for temperatures ranging from $0.78T_c$ to $0.94T_c$. Matching anomalies appear as shoulders at matching fields and can be observed more clearly as T is reduced. However, for low temperatures, penetration of the vortices in the sample takes place at higher fields. Therefore, similarly to the transport measurements, in this case, at low temperatures, it is not possible to observe the commensurability effect over a wide range of H.

Finally, we have plotted the field derivatives dM/dH and $d\chi$/dH at $0.89T_c$ (see fig. 3.6). As can be seen, maxima appear in both magnitudes at matching fields which are consistent with the expetected theoretical value (see eq. (3.2)).

3.4 Discussion: Vortex pinning *vs.* Superconducting wire network

Different methods for studying the superconducting properties of a thin film grown on top of an ordered array of magnetic nanodots have been employed: R(H), I_c(H), χ(H) and M(H). Each property characterizes the superconductor in a different range of temperatures. However, they overlap, so the study of the superconducting properties can be performed over a wide range of temperatures: minima in R(H) and peaks in I_c(H) and

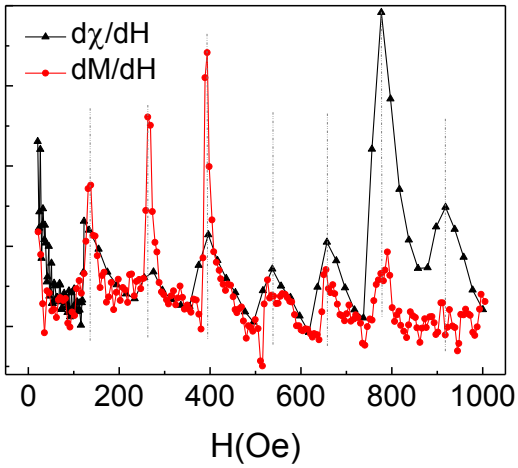

Figure 3.6: dM/dH (red dots) and dχ/dM (black triangles) for T=0.89T$_c$. Both magnitudes show maxima at matching fields (indicated as dashed lines).

χ'(H) have been observed at the matching fields at 0.99T$_c$. Whereas magnetotransport measurements do not permit measuring temperatures lower than 0.97T$_c$, peaks in χ'(H) have been observed until 0.90T$_c$. At this temperature, χ'(H) and M(H) can be compared, and features at matching fields have been observed in magnetization until 0.78T$_c$ (see fig. 3.7(a)). From our experimental results, we observe that different features appear at the matching fields for each property and, contrary to the obtained in works based on arrays of holes [43], no significant changes have been obtained as temperature is decreased.

But the most remarkably argument, supporting vortex pinning governs the oscillatory behavior, is obtained taking into account the comparison between the dimension and periodicity of the array with the coherent lengths. In this work, features at matching fields have been measured down to 0.78T$_c$. As no crossover have been obtained by reducing the temperature, the origin of the commensurability effect is the same over the whole range of temperatures. If the origin of these oscillations were based on the Little-Parks effect, that is our system behaves like a superconducting wire network, the edge-to-edge distance between dots (which will be the equivalent to the width of the wires W) should be comparable to the coherence length, specifically W$\leq$1.84ξ [42]. In our case, the edge-to-edge distance is W=200 nm and the lowest measured temperature

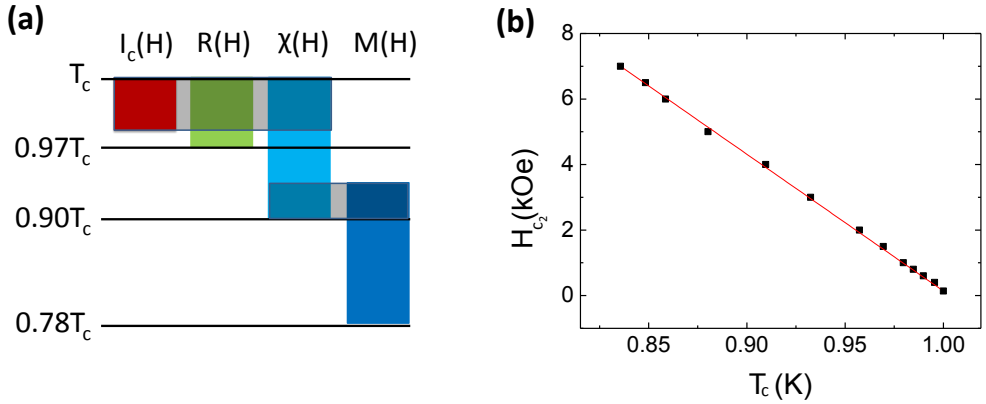

Figure 3.7: (a)Sketch showing the temperature range where the different superconducting properties have been measured. Grey areas show the overlap in temperature between properties. (b) Black squares show the experimental values of the upper critical field H_{c_2} as a function of the temperature T, the red line shows the linear fit to the experimental data.

is $0.78T_c$, to obtain $W=1.84\xi(0.78T_c)$, from eq. (3.1), we obtain that $\xi(0)$=51 nm. This value for the coherence length at 0 K exceeds the upper limit of the BCS coherence length for Nb bulk (ξ_0=39 nm) [54], so this approach is not possible.

From the temperature dependence of the upper critical field $H_{c_{2_\perp}}$ (fig. 3.7(b), $\xi(0)$ is obtained according to:

$$H_{c_{2_\perp}}(T) = \frac{\Phi_0}{2\pi\xi(T)^2}, \tag{3.3}$$

with ξ(T) the expression shown in eq. (3.1). From the linear fit, we obtain $\xi(0)$= 9 nm (which is lower than the tabulated value for Nb bulk ξ_0=39 nm because our film is in the dirty limit). From this, we can calculate the actual coherence length of our system at $T=0.78T_c$: $\xi(0.78T_c)$=19 nm. This value is more than ten time smaller than the distance between dots ($W>10\xi(0.78T_c)$) so, it is far from the superconducting wire network regime. This simple calculation rules out the wire network scenario.

3.4.1 Superconducting wire network regime

As is known coherence lengths diverge at the superconducting transition temperature; therefore very close to T_c, the coherence length is expected to be of the same order than

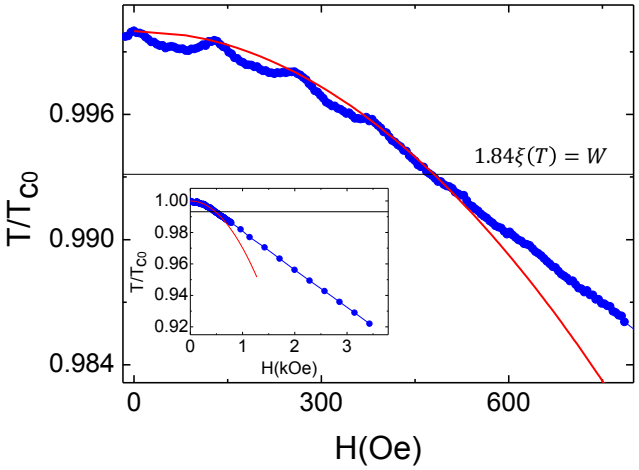

Figure 3.8: Critical temperature normalized to its zero field value as a function of the perpendicular applied magnetic field. Red line is the parabolic fitting of the maxima obtained in T_c at the matching fields. For temperatures lower than the crossover for the LP effect, a linear behavior is obtained. Inset shows Tc_c *vs.* H for higher fields.

the separation between dots. This possible scenario can be explored in the Little-Parks framework, i. e. by measuring T_c(H) very close to the critical temperature (see fig. 3.8). Three sharp maxima in the critical temperature appear at the matching fields which are commonly attributed to Little-Parks oscillations and superconducting wire network behavior.

In the superconducting wire network regime the sample behaves like a 2 dimensional system, so even for perpendicular fields $H_{c_2} \propto 1/\xi \propto \sqrt{1 - T/T_{c_0}})$ [42]. Red line in fig. 3.8 shows this fitting which confirms this behavior. However, as can be seen in the inset, for higher fields (lower temperatures) $H_{c_2} \propto 1/\xi^2 \propto 1 - T/T_{c_0})$ which is the expected behavior of a thin film in a perpendicular applied magnetic field. Black line shows the temperature criterion for the superconducting wire network (W=1.84ξ(T)); over this temperature the system satisfies the condition to obtain Little Parks oscillations and the maxima obtained in T_c at the matching fields and the parabolic fitting can be explained in the scenario of superconducting wire network.

Fig. 3.9 shows the transitions for different fields around H=H_{match} and H=5_{match}. In both graphs the red line corresponds to the matching condition (H=H_{match}), blue line

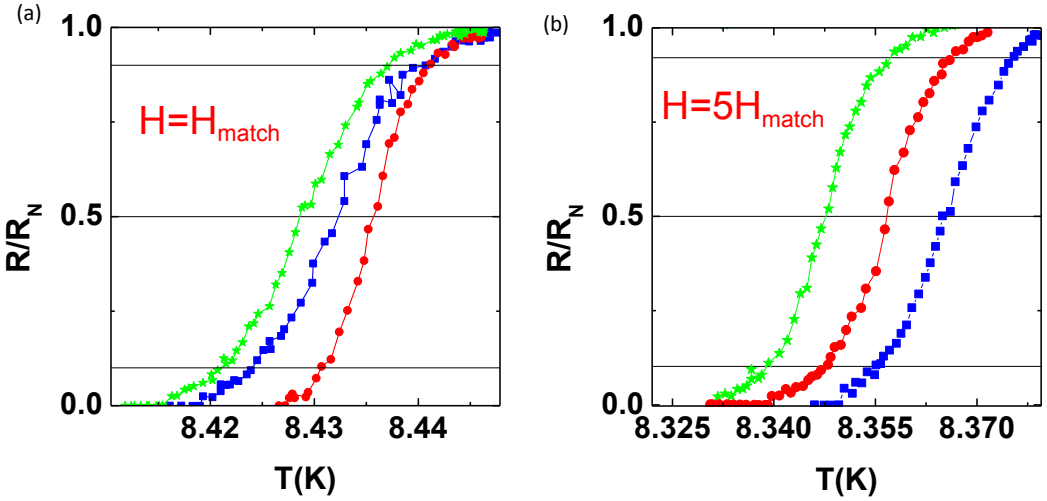

Figure 3.9: Resistive transition for different applied magnetic fields around (a) H=H_{match} and (b) H=5_{match}. In (a)[(b)] red line corresponds to H=H_{match} [H=$5H_{match}$], blue line to H<H_{match} [H<$5H_{match}$] and green line to H>H_{match} [H>$5H_{match}$].

to smaller fields (H<H_{match}) and green line to higher fields (H>H_{match}), both in out of matching conditions. A clear difference can be noticed, in the case of the first matching field (inside the Little-Parks regime), the lower temperature corresponds to the resistive transition at the matching field. However, for higher matching fields (far away from the Little-Parks transition), the lower temperature corresponds to the smaller field (even though it is out of the matching condition).

Finally, we analyze the width of the resistive superconducting transition as a function of the applied magnetic field (ΔT_c=T(0.9R_N)-T(0.1R_N)) (see fig. 3.10). Minima in the width of the transition are observed for every matching field in the whole field range. In addition, an overall enhancement of the width of the transition is observed in the crossover from the superconducting wire network regime to the thin film regime.

From these last results we conclude that a thin film grown on top of the nanodots exhibits Little-Parks oscillations and pinning enhancement. A transition from the superconducting wire network regime to pinning enhancement is observed very close to T_c (T>0.993T_c). This transition can be observed both in the T_c-H phase boundary and in ΔT_c *vs.* H. In the former, peaks in the critical temperature are obtained at the

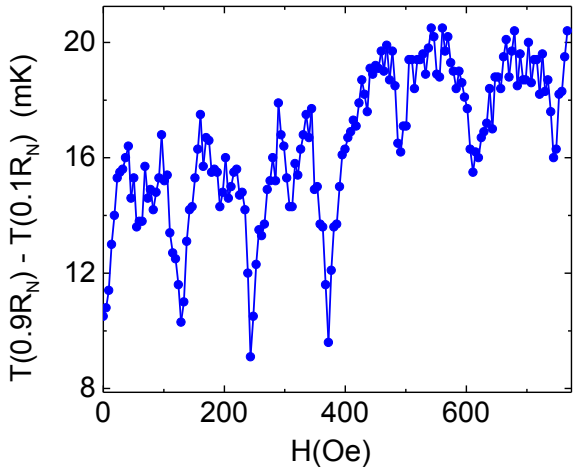

Figure 3.10: Width of the resistive superconducting transition as a function of the perpendicular applied magnetic field. Minima in the width are observed at the matching fields. An increase in the width of the transition is observed in the crossover from the superconducting wire network regime to the thin film regime.

matching fields which can be fitted to a parabolic behavior. In the later, an overall broadening of the superconducting transition is obtained in the thin film regime.

3.5 Summary

The most important points of this chapter can be listed as follow:

- The origin of the minima observed in the magnetoresistance curves needs to be clarify. They can be produced by an enhancement of pinning of the vortex lattice in a superconducting thin film or by the Little-Parks oscillations observed in superconducting wire networks. To this purpose, magnetotransport and magnetization measurements have been performed over a wide range of temperatures.

- Minima in R(H), peaks in I_c(H), peaks in χ'(H) and shoulders in M(H) have been observed at the matching fields. No difference in these features have been observed as temperature is decreased, so, there is no crossover between regimes.

- For the lower measured temperature (0.78Tf=1 kHz_c), distance between dots is 10 times bigger than the coherence length at that temperature, so the wire network regime is not possible.

- For temperatures very close to T_c ($T>0.993T_c$) a crossover to the superconducting wire network regime is observed both in T_c *vs.* H and in ΔT_c *vs.* H.

- From these experimental results, we conclude that the type of systems studied in this thesis (superconducting thin films grown on top of arrays of magnetic nanodots separated more than 200 nm) behaves like a thin film for temperatures lower than $0.993T_c$. The origin of the observed features at the matching fields below this temperature is an enhancement of the vortex pinning.

4

Vortex dynamics in bicrystal-like structures

4.1 Introduction

As was shown in the first chapter of this thesis, vortex dynamics on arrays of artificial pinning potentials has called the attention of many researches and different effects have been studied [18, 19]. Among them, commensurability or matching effects between the vortex lattice and the periodic array [8], channeling effects of the moving vortex lattice [51, 55, 56] and ratchet effects, when alternating driving forces together to asymmetric potentials induce a net flow of vortices [28, 57].

Most of the literature has been focused on regular and symmetric arrays [18], but interesting results have been already reported on other types of array, for instance fractal arrays [58], or short-range ordered arrays [59]. In this chapter, we study commensurability and rectifier effects, if any, when the vortex lattice moves on an array with two different potential landscapes. Although the array is fabricated with symmetric nanodots, these nanodots are arranged in two different lattices. We can call this array a bicrystal-like array. A border line, a boundary, separates the two potential landscapes in the array.

This type of array allows addressing different effects as the role played by the pinning center density, the competition between commensurability and rectifier effects and so on.

To investigate this phenomena two different bi-arrays have been fabricated. The first one keeps the same nanocenter density along the two halves of the array and the full bi-array shows reflection symmetry. The second bi-array shows different nanocenter densities in each half of the array and, in addition, reflection symmetry is broken in one of the two halves. In the former, matching effects could be analyzed, in the latter commensurability and ratchet effect could be explored.

4.2 Sample Description

Two different hybrid samples have been fabricated on Si (100) substrates. Both samples consist on arrays of Ni circular dots embedded in Nb films. Standard electron beam lithography and sputtering techniques have been used to fabricate the arrays following the usual procedure. The dimension of the whole array is 100 μm x 100 μm. The Ni dot dimensions are 40 nm thickness and 200 nm diameter. On top of the array, the Nb film is grown by sputtering with a thickness of 100 nm (section 2.1).

Sample A (see fig. 4.1) is fabricated with two lattices of Ni dots, one of them shows square order with a unit cell side of 400 nm. The second lattice shows triangular order with a triangle side of 430 nm. These dimensions and arrangements ensure the same density of pinning centers along the whole bi-array.

Sample B (see fig. 4.2) is fabricated looking for a completely different scenario. The bicrystal-like array is grown with two dissimilar Ni dot densities and with reflection symmetry in one half of the array and with broken reflection symmetry in the other one. One half of the bi-array shows a triangular order with a triangle side of 400 nm. The second half of the bi-array shows lower density of Ni dots. This half of the bi-array has been obtained from the triangular lattice by eliminating dots at selected positions. The well known kagomé periodic array, which shows reflection symmetry, can be obtained by taking out 3/4 of the dots from the triangular lattice. An array lacking reflection symmetry is achieved from the triangular lattice eliminating 3 out of 9 pinning sites [22]. The result is a kagomé-like lattice that exhibits a reflection symmetry axis from the

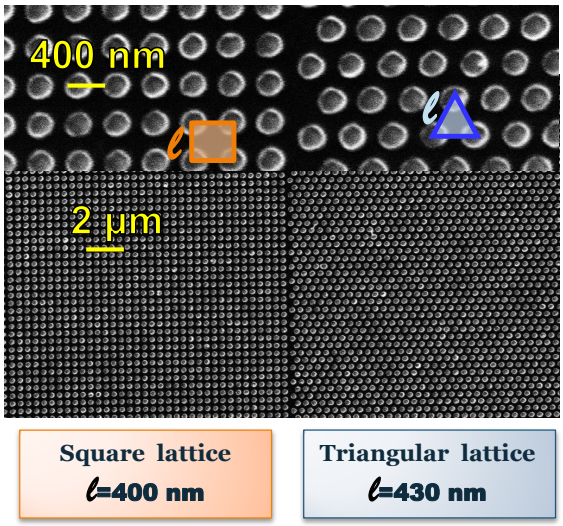

Figure 4.1: SEM image of sample A bi-array consisting of two lattices of Ni dots (dot diameter is 200 nm, and thickness is 40 nm). The left lattice shows square order with a unit cell side of 400 nm. The right lattice shows triangular order with a triangle side of 430 nm. Two different scales are shown.

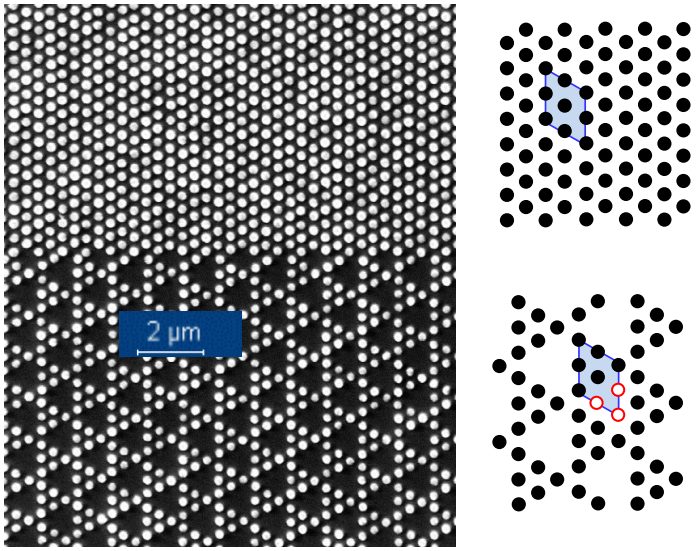

Figure 4.2: SEM image of sample B bi-array consisting of two lattice of Ni dots (200 nm dot diameter and 40 nm thickness). The upper lattice shows a triangular order with a triangle side of 400 nm. The lower lattice has a kagomé-like order and can be derived from the triangular lattice by eliminating a fraction of 3/9 from the triangular one; thus, only a fraction of 6/9 remains forming a lattice of triangular building block. (See the sketch on the right side of the panel)

base to the tip of the triangles (see the sketch in fig. 4.2). Therefore, a periodic pinning potential with broken reflection symmetry can be obtained from triangular arrays of circular Ni dots.

For transport measurements, a cross-shaped 40 μm wide bridge has been defined in the magnetic/superconducting hybrid sample (section:fabricacion). A SEM image of the bridge is shown in fig. 4.3 showing the alignment of the bridge with respect to the boundary between lattices in sample B. This cross-shaped bridge allows injecting currents and measuring voltages in two perpendicular directions, for instance parallel or perpendicular to the boundary or to the reflection symmetry axis in sample B (the symmetry axis of the kagomé-like array is from base to tip of the triangular building block (fig. 4.2)).

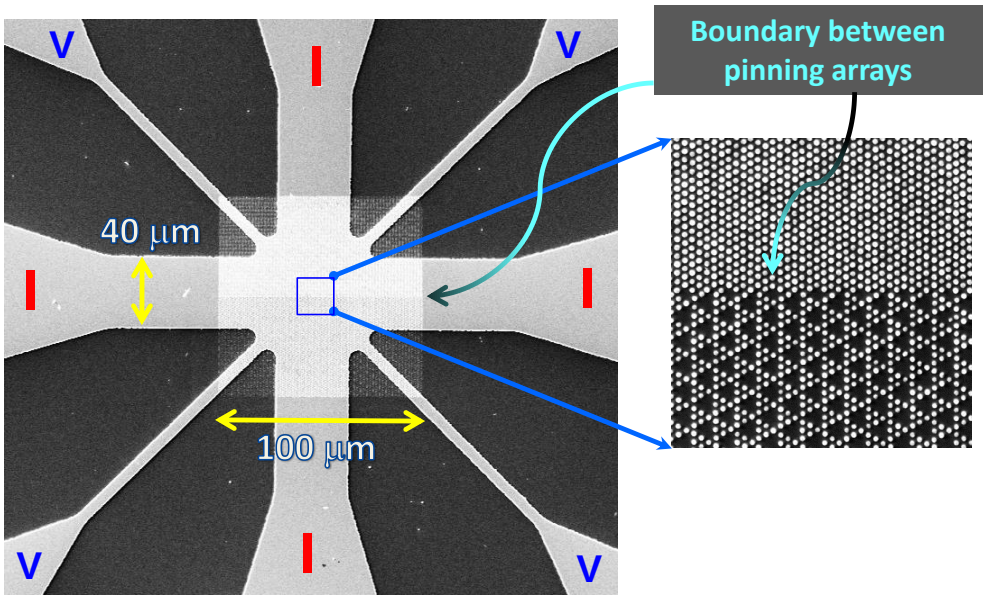

Figure 4.3: SEM image of the cross-shaped measurement bridge (40 μm width) showing the alignment with respect to the bi-array. The current contacts (labeled as "I") and the voltage contacts (labeled as "V") are shown too. Bi-array dimension is 100 μm side and the boundary between pinning arrays is located along and at the half width of one of the current paths.

4.3 Vortex dynamics

4.3.1 Commensurability effect

Sample A

Figure 4.4 shows magnetoresistance data when the vortex lattice moves on a bi-array with two regions of different unit cells: square and triangular cells. In this bi-array the dot density is kept the same along the whole array. The experimental data have been recorded for two temperatures close to the superconducting critical temperature and for vortex motion parallel or perpendicular to the boundary which separates the bi-array in two halves, one half with triangular symmetry and the other one with square symmetry (see fig. 4.1). The main minimum appears at applied magnetic field 129 Oe. This value is exactly the same which is obtained theoretically, taking into account the dot density.

The main matching field (m=1) is the one for which the density of vortex lattice equals the density "n" of pinning centers:

$$H_m = m \cdot n \cdot \phi_0, \tag{4.1}$$

For a square lattice (with "a" being the side of the square):

$$n(square - lattice) = \frac{1}{a^2} \Rightarrow H_m(square - lattice) = m \cdot \frac{1}{a^2} \cdot \phi_0, \tag{4.2}$$

For a triangular lattice (with "a" being the side of the equilateral triangle):

$$n(triangular - lattice) = \frac{1/2}{(\sqrt{3}/4)a^2} \Rightarrow H_m(triangular - lattice) = m \cdot \frac{2}{\sqrt{3}a^2} \cdot \phi_0, \tag{4.3}$$

The magnetoresistance data and the positions of the minima do not reveal the unit cell of the vortex lattice. Moreover, the vortices do not distinguish whether or not the vortex lattice moves from the triangular array to the square array (vortex motion perpendicular to the boundary) or the vortices sweep both landscapes at the same time, i. e. vortices move parallel to the boundary. The conclusion of these experimental data is very clear: the density of pinning centers emerges as the only parameter which governs the behaviour of the vortex matching effects. When the applied magnetic fields

are such that the density of vortex lattice is an integer number of the density of pinning centers, commensurability effects appear. That is, for selected values of the applied magnetic fields, the vortex lattice slows down and minima show up.

Sample B

In sample B the scenario is fully different, since the two parts of the bi-array show different dot densities and one of the areas (kagomé-like symmetry) shows broken reflection symmetry (see fig. 4.2).

Figure 4.5(a) shows the magnetoresistance measurements at constant temperature for the two relevant vortex motion directions, i.e. parallel or perpendicular to the boundary which separates the two Ni dot lattices. In comparison with the results obtained in sample A, we observe that the magnetoresistance minima look different in each one of the directions. When the vortex lattice moves perpendicular to the boundary between the two areas (triangular and kagomé-like) there are sharp and well define minima but, when the vortex lattice moves parallel to the boundary, one of the minima disappears and the rest of them are shallow and not so well define.

First of all, we analyze the position of the minima for vortex motion perpendicular to the boundary. Matching fields are extracted from the slope of the linear fit of the magnetic field position of the resistance minima *vs.* the index number n, results of the linear fit are shown in fig. 4.5(b).

The first matching field at 99 Oe corresponds to the main minimum in the kagomé-like array. Since this array has been obtained by eliminating 3 out of 9 dots of the triangular lattice, this matching field is also a fractional minimum of the triangular array:

$$H_1(kagome-like) = \frac{6}{9} \cdot H_1(Triangular) = \frac{6}{9} \cdot 149Oe, \tag{4.4}$$

In this configuration of motion, the first and second minima corresponding to the triangular array are also observed.

In the case of vortex motion parallel to the boundary the kagomé–like minima are absent and we only observe the matching conditions for the triangular array (see fig. 4.5(a)).

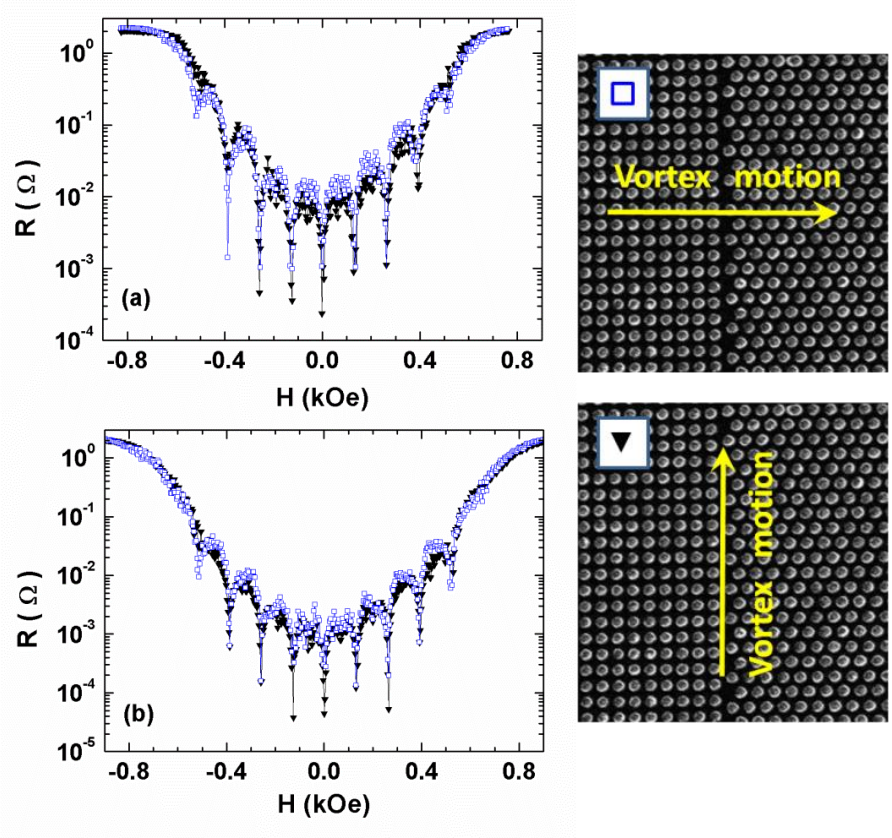

Figure 4.4: Sample A. Resistance (R) as a function of the magnetic field (H) applied perpendicular to the substrate. Critical temperature is $T_c = 8.35$ K. Blue squares correspond to vortex motion perpendicular to the border line which separates the two Ni dot lattices (see the upper sketch on the right). Black triangles correspond to vortex motion parallel to the boundary (see the lower sketch on the right). (a) R(H) at temperature T=0.99T_c and (b) at temperature T=0.98T_c.

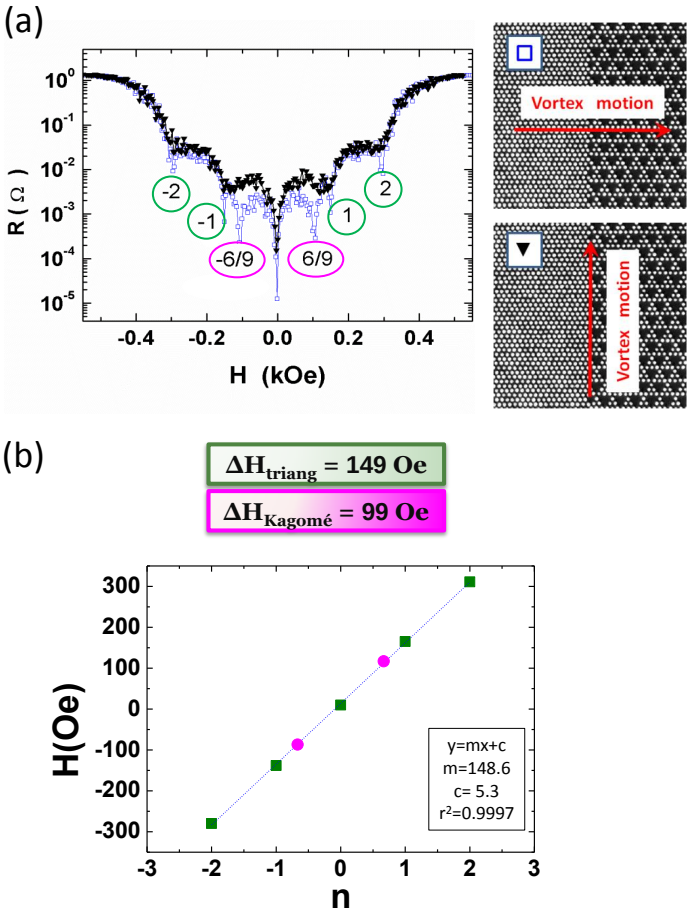

Figure 4.5: Sample B. (a) Resistance (R) as a function of the magnetic field (H) applied perpendicular to substrate at temperature T=0.98T_c. The critical temperature of the sample is T_c = 8.63 K. Blue squares correspond to vortex motion perpendicular to the boundary which separates the two Ni dot lattices (see the upper sketch on the right). Black triangles correspond to vortex motion parallel to the border line (see the lower sketch on the right). Numeric label 1 indicates first integer matching field for the triangular lattice, numeric label 2 indicates second integer matching field for the triangular lattice and numeric label 6/9 indicates fractional matching field for the triangular lattice or first integer matching field for the kagomé-like lattice.(b) Magnetic field position of the resistance minima *vs.* the index number n. Magenta dots correspond to the matching fields from the kagomé-like array and the green squares to the triangular one. The blue dashed line is the linear fit to the experimental data.

Straightforward conclusion can be extracted taking into account the path that the vortex lattice follows in each one of the two directions. When the vortex lattice moves perpendicular to the boundary, the interaction of the vortices with the two landscapes occurs one after the other, so the vortex lattice fits the two densities. When the vortex lattice flows along both landscapes at the same time, the triangular ordered array overcomes the kagomé-like order and the vortex lattice becomes commensurable with the triangular array.

4.3.2 Ratchet effect

Sample B

Finally, we explore the possible ratchet effect in sample B, since part of the bi-array shows broken reflection symmetry induced by an asymmetric arrangement of the nickel nanodots (see fig. 4.2). This asymmetry could be only probed moving the vortices in the direction parallel to the boundary,*i.e.*, in the direction where the vortex lattice does not match the kagomé-like potentials.

Figure 4.6 shows a clear ratchet effect for the first integer matching field of the triangular lattice. It is observed in the appropriate direction: for vortex motion parallel to the boundary (ac current is injected perpendicular to the boundary). In addition, the ratchet effect vanishes when the vortex lattice moves perpendicular to the boundary, since vortices are moving in a symmetric potential landscape.

Temperature dependence is shown in fig. 4.6. As temperature is decreased, V_{DC} signal is increased and the needed injected ac current to observe the effect is increased.

In the work of Perez de Lara *et al.* [22] vortex dynamics was studied in a sample grown on top of the same kagomé-like arrangement of nickel nanodots. In that work, ratchet effect is observed and a reversal of the dc voltage signal is measured as ac current is increased independently of the perpendicular applied magnetic field. Reversal signal is generated by interstitial vortices that move at lower currents in potential wells of opposite asymmetry ([22, 28].

However, in this sample with a bi-crystal structure, no reversal is obtained. In this case, even though half of the array has the same arrangement that in that work

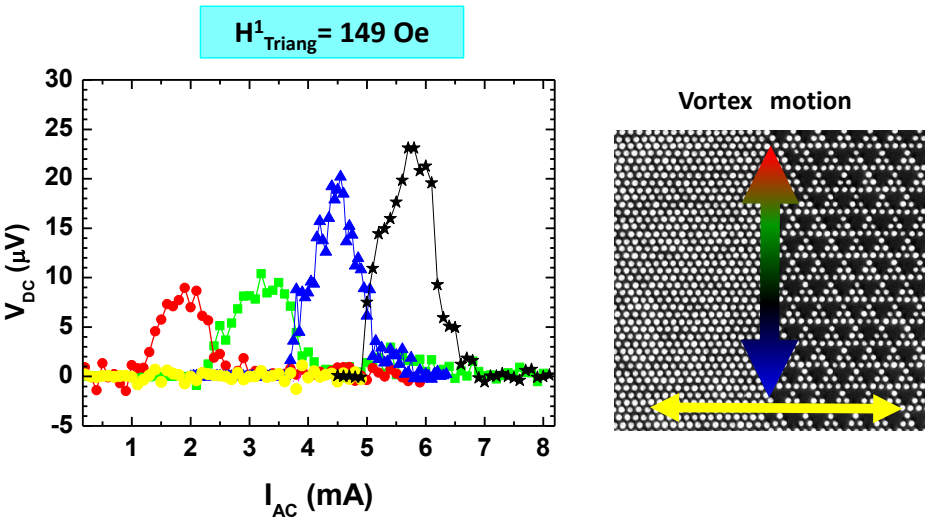

Figure 4.6: Sample B. DC voltages (Y-axis) vs. AC current amplitudes (X-axis) at different temperatures. The critical temperature of the sample is T_c =8.63 K and the temperatures are: 8.40 K (black stars), 8.45 K (blue triangles), 8.50 K (green squares) and 8.55 K (red and yellow circles). Vortex motion is parallel to the boundary for red, green, blue and black curves and perpendicular to the boundary for yellow circles. The perpendicular magnetic field corresponds to the first matching field of the triangular lattice.

(kagomé-like arragement), the other half is a triangular lattice where no asymmetry is present and, in addition, no interstital vortices are present for this applied field.

4.4 Summary

The most important points of this chapter can be listed as follow:

- Bi-array with single pinning density. Commensurability effects between the vortex lattice and the pinning centers do not depend on the geometry of the dot array. Minima appear in the magnetoresistance, when the vortex lattice density is an integer number of the pinning density independent of the vortex motion direction respect to the boundary of the bi-array. So, the moving vortex lattice arrangement cannot be extracted from these experimental data.

- Bi-array with different pinning densities. (a) Vortex motion perpendicular to the boundary shows minima in the magnetoresistance at integer matching fields of both the triangular and kagomé-like dot arrays. In this case, vortex lattice crosses both arrays and both matching conditions develop.(b) Vortex motion parallel to the interface only shows shallow minima in the magnetoresistance coming from the commensurability condition with the higher density array (triangular dot lattice).

- Bi-array with symmetric and asymmetric pinning potentials. The asymmetric pinning landscape (kagomé-like in our case) produces ratchet effect under ac injecting currents when the vortex motion is along the reflection symmetry axis (from triangle building block base to tip), in spite of there is not commensurability between the vortex lattice and the kagomé-like array.

5

Control of Dissipation:

Tuning the magnetic stray field

5.1 Introduction

Superconductivity and magnetism are generally considered competing effects, but these two long range order phenomena, with proper system design, have been shown to develop cooperative behavior. Recent studies have focused on the role of the magnetic stray fields in the behavior of the superconductivity, specially very close to the phase transition, when superconductivity is only weakly developed [19]. For instance, the nucleation of superconductivity can be controlled in superconductors grown on top of plain ferromagnetic films that exhibit a periodic domain structure. In this case, the superconductor is influenced by a nonuniform magnetic field profile that can be altered by changing the magnetic domain structure and the external applied magnetic field [60, 61].

As has been shown in previous chapters, magnetic nanostructures strongly influence the vortex dynamics by enhancing the pinning of the superconducting vortex lattice.

In this chapter, we will use magnetoresistance measurements to determine the effects of stray fields in the dissipation process. We will show that, on the contrary to the expected behavior, in the regime where vortices are already moving (over the critical current), an increase in the magnetic stray field generates an increase in dissipation. These results systematically probe the main role of stray fields in superconducting vortex dynamics.

5.2 Sample Description

Arrays based on circular Co/Pd nanodots (200 nm diameter and 42 nm thickness) were fabricated using electron beam lithography, in conjunction with magnetron sputtering in a high vacuum chamber with a base pressure of $1x10^{-8}$ Torr. The nanodots are polycrystalline, arranged on a rectangular lattice (400 nm x 600 nm spacing) covering an area of 100 x 100 μm^2 (see fig. 5.1(a) and (b)).

Three arrays have been fabricated keeping identical physical dimensions but with different relative thickness of the Co/Pd layers:

- **In-plane single domain sample (IPSD)**: Pd(24nm)/Co(16nm)(fig. 5.1(c)).
- **Vortex state sample (VS)**: Pd(5nm)/Co(35nm)(fig. 5.1(d)).
- **Out of plane sample (OP)**: $[Pd(0.6nm)/Co(0.4nm)]_{40}$ multilayer (fig. 5.1(e)).

Every structure was finished with a 2 nm Pd layer to prevent oxidation (capping layer).

After the magnetic characterization, following the usual procedure, a 100 nm thick Nb film was deposited and the cross-shaped bridge centered on the array was defined to form the magnetic / superconductor hybrid structure to perform the transport measurements (see section 2.1).

5.3 Magnetic Characterization

Magnetic characterization was performed by vibrating sample magnetometry (VSM), magnetic force microscopy (MFM) and magneto-optical Kerr effect (MOKE) (see section 2.3).

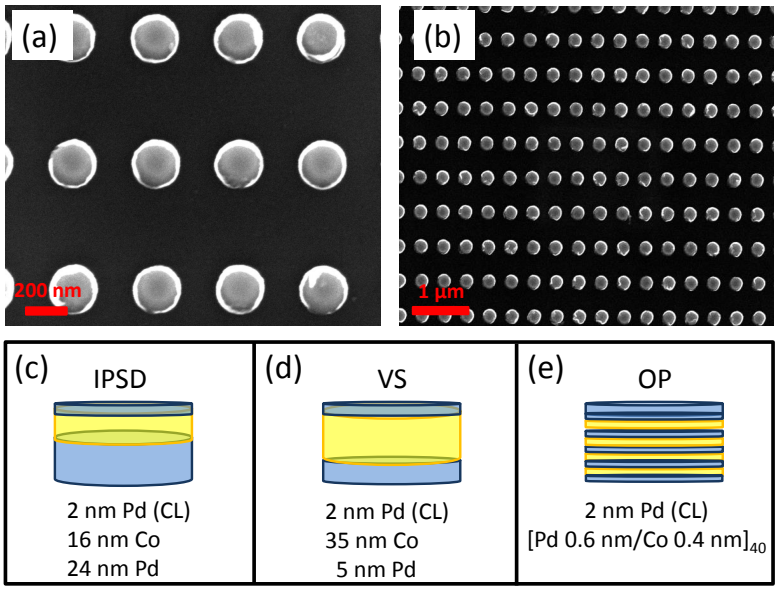

Figure 5.1: (a) and (b) show SEM images of a rectangular lattice with different magnification (bar scale is shown in each image). (c), (d) and (e) show a sketch of the nanodot composition of the IPSD, VS and OP samples respectively.

5.3.1 In plane magnetization: First Order Reversal Curves

Magnetic characterization is usually based on measuring hysteresis loops. From them, we can extract very useful information of the magnetic properties of the sample such as saturation magnetization (M_s), remanence magnetization (M_r), coercivity (H_c), initial susceptibility (χ_i), etc. First Order Reversal Curves (FORC) distribution is an extra tool to be considered that can give new information of the studied system [62, 63].

The measurement procedure of the FORC's is schematically shown fig. 5.2(a). First, the sample is subjected to a saturating field. Then, the field is lowered to a reversal field (H_r) and the FORC curve is acquired increasing back the field to positive saturation. The FORC curve M(H,H_r) is the magnetization curve (M) as a function of the applied magnetic field (H) and the reversal field (H_r). Figure 5.2(b) schematically shows a family of FORC's (usually 10^2 FORC's are measured by decreasing H_r until the negative saturation field is reached).

After measuring a family of FORC's, the FORC distribution is calculated. This distribution is defined as a mixed second order derivative of M(H,H_r):

$$\rho(H, H_r) = -\frac{1}{2}\frac{\partial^2 M(H, H_r)/M_s}{\partial H \partial H_r} \tag{5.1}$$

This derivative evaluates how the slope between FORC's changes along H and H_r.

Fig. 5.2(b) will be used to explain the physical information that can be extracted from this derivative. See, for example, blue FORC in fig. 5.2(b): we positively saturate the sample and travel down to H_{r_1}. If H_{r_1} does not reach the smallest flipping field of the sample, no irreversible switching event will take place, every FORC will simply trace out on top of the previous one and magnetization will be only function of the applied magnetic field H. In this case, if we examine the derivatives in eq. (5.1), we will get $\rho = 0$. The physical meaning of $\rho = 0$ is that every switching process has been reversible.

If we then decrease H_r (see red FORC for H_{r2} and H_{r3}in fig. 5.2(b)) and an irreversible switching event occurs (such as flipping a single domain particle or nucleation a magnetic domain), the obtained FORC will be a new curve which will tend to fill the interior of the major hysteresis loop. In this case, magnetization depends on both H and H_r, and

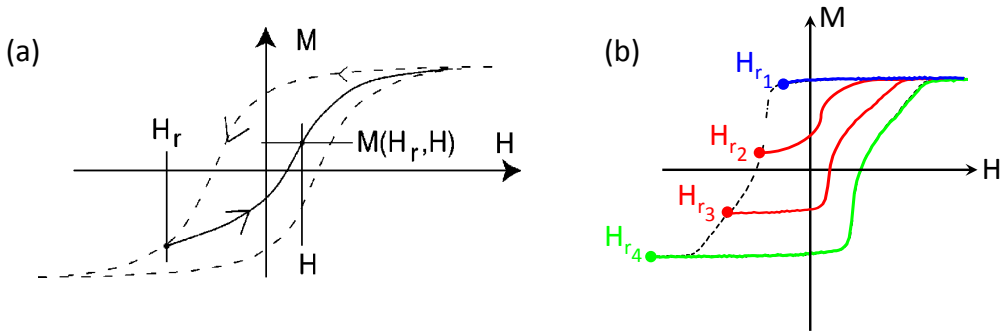

Figure 5.2: (a) FORC acquired after saturating in a positive applied field. (b)Schematic family of first order reversal curves (FORCs). Blue and green FORCs correspond to reversible processes, for which the FORC distribution is zero. Red FORCs represent irreversible processes with non-zero value of the FORC distribution.

$\rho \neq 0$. That is, irreversible switching events generate a value of the FORC distribution different to zero.

Finally, when H_r reaches the negative saturation field (see green FORC for H_{r4} in fig. 5.2(b)), every FORC will travel back up the descending curve, magnetization will not depend on H_r and $\rho = 0$.

In summary, we get that FORC distribution is a function of H and H_r and a change in the slope between FORCs corresponds to a irreversible switching event during the magnetization process that will generate a FORC distribution different to zero ($\rho \neq 0$).

Originally FORC distribution were based on the procedure described by Mayergoyz for experimentally determine a Preisach distribution. The Preisach model is based on a distribution of hysterons, which are elements of irreversible switching defined by two stable states (+1 and -1), needed to generate a macroscopic hysteresis loop [64, 65]. Each hysteron is characterized by a coercivity (H_C), which corresponds to the loop half width, and bias field (H_B), which corresponds to horizontal loop shift,(see fig. 5.3(a)). In this model, $\rho(H_B, H_C)$ corresponds to the weight function of the hysterons. This model can be extrapolated to a macroscopic sample. In that case, $\triangle H_C$ gives information of the coercivity distribution due to different particle sizes or anisotropy distribution and $\triangle H_B$ gives information of the bias field distribution usually due to interactions.

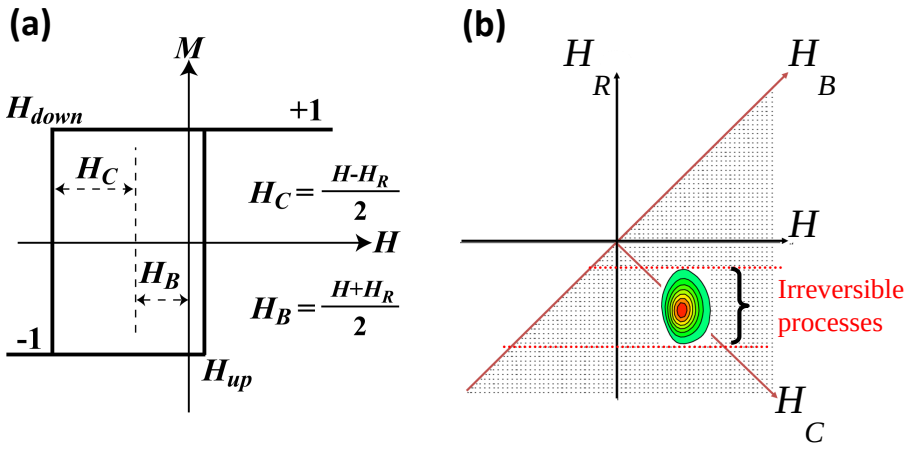

Figure 5.3: (a) Schematic of a hysteron.(b) (H,H_r) and (H_C,H_B)coordinate systems. Dashed part represents the allowed measurements region.

Both coordinate systems, (H,H_r) and (H_C,H_B), can be related by a coordinate transformation which corresponds to a rotation of the axes. Note that as $H > H_r$, FORC distribution is only possible for $H_C > 0$ (see fig. 5.3(b)).

$$H_C = \frac{H - H_r}{2} \tag{5.2}$$

$$H_B = \frac{H + H_r}{2} \tag{5.3}$$

In Plane Single Domain Sample

We will start analyzing the FORC distribution obtained for a single domain, uniaxial particle (SDP):

Imagine that the SDP is saturated in the positive direction along the easy axis. If the magnetic field is decreased (see red line for H_r1 in fig. 5.4(a)), the SDP will remain aligned along the positive direction until the negative switching field (-H_{switch}) is reached. So, for H_r >-H_{switch}, the magnetization process is totally reversible and does not depend on the H_r. This generates a FORC distribution equal to zero.

If H_r reaches the negative switching field (-H_{switch}) (see purple line for H_{r2} in fig. 5.4(a)), the SDP will be flipped and will remain in the opposite direction until the

applied magnetic field H reaches the positive switching field (+H_{switch}) that will flip the particle again to the positive direction. This is an irreversible event that will ocurr for $H_r = -H_{switch}$ and $H = +H_{switch}$, so it will generate a FORC distribution different from zero around $H_B = 0$ (see fig. 5.4(a)).

Figure 5.4(b) shows the family of FORCs obtained for the IPSD Sample (Pd(24nm)/ Co(16nm) bilayer fig. 5.1(c)) for the applied magnetic field applied along the short axis of the until cell. As can be seen in fig. 5.4(c), the obtained FORC distribution exhibits a prominent ridge along the local coercivity H axis, centered at $H_B = 0$.

This FORC distribution is characteristic of the single domain behavior, the spread centered on $H_B = 0$ is due to the interaction between the nanodots and the spread along H_C is due to distribution in size and thickness of the nanodots in the array.

Vortex State Sample

As shown before, 16 nm thick Co layers exhibit single domain behavior. However, when the Co thickness layer is increased, a different magnetization behavior is obtained. In this case, we will analyze the magnetic behavior of the VS sample, with a 35 nm thick Co layer (fig. 5.1(d)).

This sample exhibit completely different FORC characteristic (see fig. 5.5(a) and (b)). The FORCs family have a pinched shape near zero applied field with very low remanence; the FORC distribution shows two pronounced peaks.

To analyze these results, micromagnetic simulations using the OOMMF code [36] have been done for a sample of identical dimensions. As can be seen in fig. 5.5(c), the reversal of the magnetization is mediated through the formation of a closed flux structure called magnetic vortex. In this case, two irreversible magnetization switching occur: the vortex nucleation and annihilation. Both events appear in the FORC distribution as two pronounced peaks (see fig. 5.5(b)). The first feature corresponds to the annihilation of the vortices, as the $H_r = 0$ is reduced, vortices are nucleated and as H is increased, they are annihilated. The second feature is similar but from negative saturation, in this case, the peak corresponds to the nucleation of the magnetic vortex [66, 67].

The magnetic vortex state corresponds to a state where the magnetization vector remains parallel to the nearest edge of the nanodot, so, reducing the stray fields and

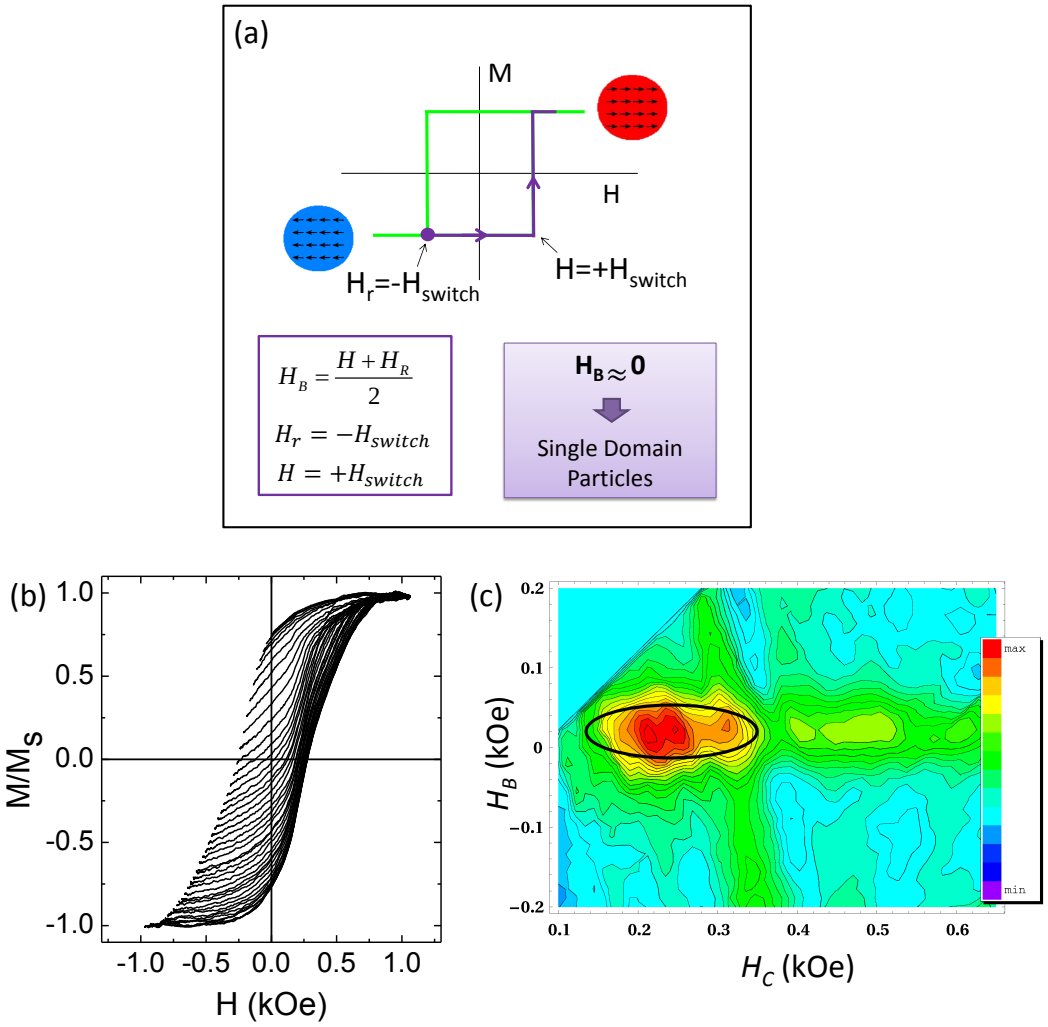

Figure 5.4: (a) Schematic of a single domain, uniaxial particle switching process.(b) Shows the family of FORCs and (c) the corresponding FORC distribution obtained for the IPSD sample.

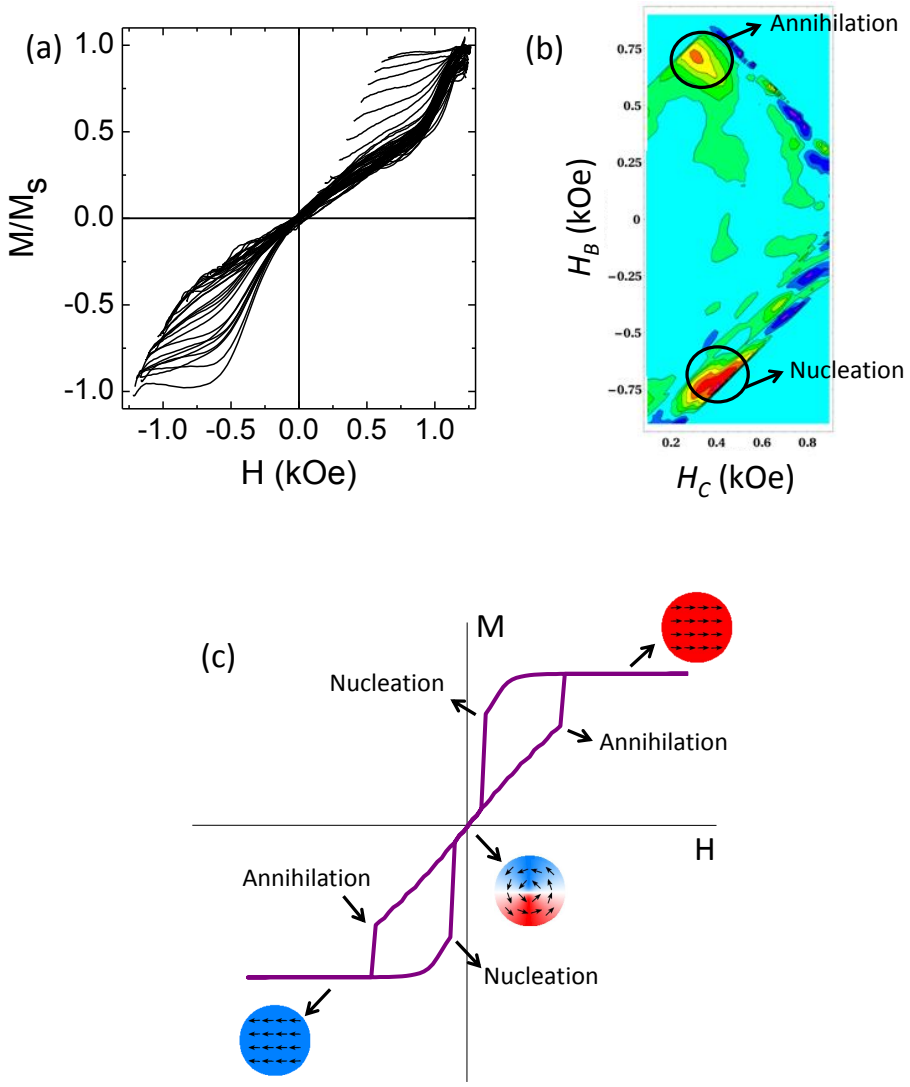

Figure 5.5: (a) shows the family of FORCs and (b) the corresponding FORC distribution obtained for the VS sample.(c) Simulated hysteresis loop of the sample; arrows indicate the annihilation and nucleation fields and insets the negative/positive saturated states and the vortex state at remanence.

hence lowering the magnetostatic energy [35] . However, in the center of the dot the spins point in the perpendicular direction (out of the plane of the nanodot). This region is the so-called vortex core and it is the only region that generates stray field [68]. The thinner the Co layer, the higher the demagnetization energy cost to form the vortex core. So, reducing the thickness of the magnetic layer tends to inhibit the formation of the vortex state [69]. As a result, in the IPSD, where the Co layer is 16 nm thick, the magnetization reversal is mediated through a coherent rotation of the spins (single domain behavior). In contrast, in the VS where the Co layer thickness is increased up to 35 nm, the magnetization reversal is mediated through the formation and annihilation of a magnetic vortex.

5.3.2 Out of Plane Magnetization

Magnetic nanostructures with perpendicular anisotropy have received significant scientific and technological attention for their fascinating magnetization reversal processes and important applications in perpendicular magnetic recording. In our case, we focus on Co/Pd multilayers which exhibit out of plane magnetization due to surface anisotropy at the Co/Pd interfaces and strain in the Co layers [70, 71].

In addition, it has been shown that by varying the sputtering pressure during deposition, magnetic anisotropy can be controlled: an increase in the growth Ar pressure introduces disorder which raises coercivity. In fact, pressure-graded media based in Co/Pd multilayers has been recently studied and proposed to be used as a storage media material. The soft layers help to decrease the necessary write field (due to the low coercivity) and the hard layers give the thermal stability to the whole structure due to the high exchange couple between the layers [72, 73].

The MOKE effect device used in the previous section for magnetic characterizations of IPSD and VS samples is not sensitive to out of plane magnetization. Therefore, in the case of the OP sample, magnetic force microscopy (MFM) and vibrating sample magnetometry (VSM) at room temperature was used to perform magnetic characterization.

Previous to the sample deposition, several samples with different Ar pressure were grown. As shown in fig. 5.6 (a) and (b), for 2 mTorr and 5 mTorr Ar pressure, low

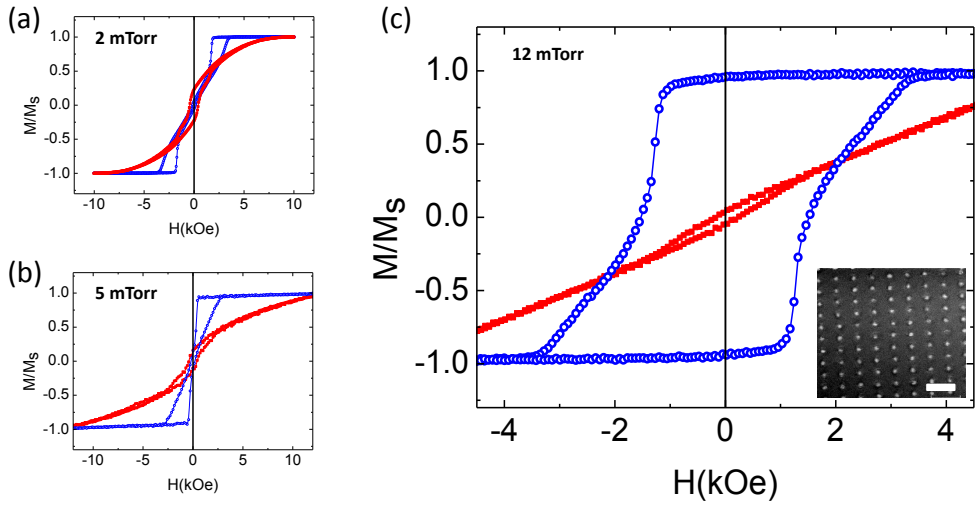

Figure 5.6: Out-of-plane (blue circles) and in-plane (red squares) hysteresis loops obtained for a witness sample of the [Pd(0.6nm)/Co(0.4nm)]40 film with an Ar sputtering pressure of (a) 2mTorr, (b) 5 mTorr and (c) 12 mTorr. Inset in (c) shows an MFM image of the remanent state of the array after positive saturation.

coercivity and remanence is obtained. However, when the Ar sputtering pressure is tuned to 12 mTorr an out-of-plane magnetization of the sample is obtained. Figure 5.6(c) shows the out-of-plane and in-plane hysteresis loop of the witness sample and confirms the out-of-plane anisotropy (with higher coercivity, higher remanence and lower saturation field for the out of plane hysteresis loop). In addition, MFM was performed on the patterned sample and confirms that the nanodots exhibit a single domain out of plane at remanence after saturation (see inset in fig. 5.6(c)).

5.4 Superconducting properties: Dissipation

5.4.1 Experimental procedure

In this work, a rotatable sample holder was used to apply magnetic fields perpendicular or parallel to the sample plane.

Before studying the superconducting properties, the following procedures were used to set the nanodots in different magnetic states:

1. The ac-demagnetized state of the magnetic nanodots was realized by applying a decreasing ac magnetic field.

2. The remanent state was induced in the sample by applying a 20 kOe saturating magnetic field and then switching it off.

To perform the magnetotransport measurements, small magnetic fields were applied perpendicular to the sample plane, which do not change the magnetic states of the nanodots.

5.4.2 Tuning the magnetic stray field

As discussed in section 5.3, using Co dots with identical physical dimensions but choosing the appropriate relative thickness of the Co/Pd layer, three different magnetic states have been obtained: IPSD, VS and OP. This approach allows to study the influence of the magnetic stray field in the dissipation in the mixed superconducting state eliminating the complications from structural variations at the superconductor/ferromagnetic interfaces.

By means of the OOMMF code [36] and Matlab simulations, the magnetic stray fields generated by each dot in a plane 50 nm over the dots have been simulated. The results for the OP, IPSD and VS samples are shown in fig. 5.7(a), (b) and (c) respectively. As can be seen, the OP case has the largest stray field (every magnetic moment is aligned out of plane), the flux-closure VS has the least stray field (the magnetic moments of the nanodots are oriented along the edge of the dot and only the magnetic moments in the vortex core generate stray field). The IPSD case is in between the OP and VS sample as magnetic poles in both sides of the dot generate stray field.

Figure 5.7(d) shows a comparison of the dissipation data at T=0.985T_c for the three stray field configurations which correspond to the OP configuration (blue triangles), IPSD configuration (red squares), and VS configuration (green circles). As it can be extracted from these results, a clear influence of the magnetic stray field in the dissipation is observed.

As introduced in section 1.2.3, magnetic pinning is the result of a compensation between Meissner currents that expel the stray magnetic stray field generated by the dots with the superconducting currents of the vortices: when the superconducting vortex

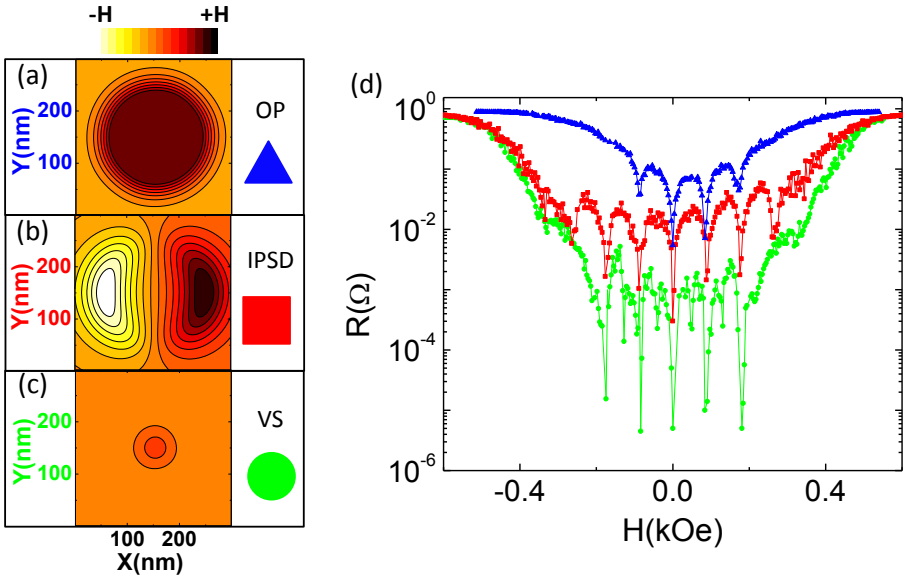

Figure 5.7: Magnetic stray field profile generated by each magnetic dot in the remanent state of the (a) OP sample, (b) IPSD sample and (c) VS sample. (d) Resistance vs. perpendicular applied magnetic field at temperature $0.985T_c$ in the remanent state. Blue triangles show data obtained for the OP sample, red squares for the IPSD sample and green dots for VS sample.

sits on the dot, both currents compensate and the free energy diminishes. As the higher the stray field, the higher the screening currents, pinning increases with the stray field. This increase in the pinning strength produces an increase in the depinning current (current required to set superconducting vortices into motion)[74–76].

In the present experimental work we explore a different regime: in our case, measurements are performed over the depinning current, so vortices are already moving. In this case, and in contrast to the expected behavior, an increase in the stray field leads to an increase in the dissipation. That is, the OP array yields the largest dissipation, the VS sample produces the smallest dissipation, and the dissipation value of the IPSD sample is in between. In fact, as can be extracted from fig. 5.7, the monotonous background dissipation can be decreased by more than two orders of magnitude as the stray field is reduced from OP to VS.

In the following sections, we will study, case by case, the influence of the stray field in the superconducting properties before and after magnetizing the dots.

Out-of-plane magnetization sample

Figure 5.8 shows the experimental magnetoresistance data for the OP sample. Results are shown for the three different states that can be set in this sample: i) ac-demagnetized state (circles), ii) remanent configuration after positive saturation (magnetization remains parallel to positive magnetic field direction) (red pointing-up triangles) and iii) remanent configuration after negative saturation (magnetization parallel to negative magnetic field) (green pointing-down triangles). The measurements show that the lowest dissipation corresponds to the ac-demagnetized state with random up and down domains inside each dot. In contrast, the dissipation increases by more than one order of magnitude when the entire array remains in a particular orientation. For the positive (ii) and negative (iii) magnetized states, a peak asymmetry appears which is shown to switch sides.

This asymmetry in the periodic minima distribution has been already shown in critical current measurements as a function of the magnetic field [77]. This effect is well understood since pinning force can be either attractive or repulsive depending on the relative alignment (parallel or antiparallel) between the superconducting vortices

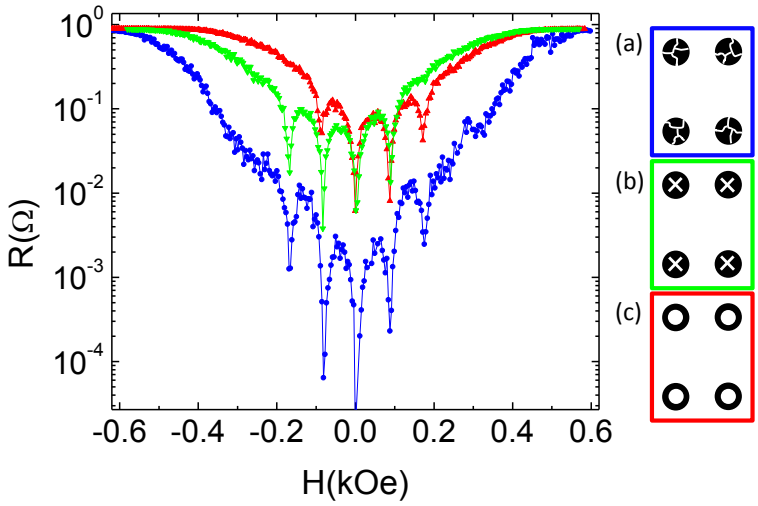

Figure 5.8: Resistance vs perpendicular applied magnetic fields at temperature T=0.985T$_c$ for the sample with out of plane magnetization (OP sample). Blue circles show data obtained for the demagnetized state, red pointing-up triangles for positive magnetized state and green pointing-down triangles for negative magnetized state. (a), (b) and (c) show a sketch of the three states respectively.

and the magnetic moment of the nanodot: $E = -\overrightarrow{\mu} \cdot \overrightarrow{H}$, where $\overrightarrow{H}$ represents the superconducting vortex generated by the external applied field and $\overrightarrow{\mu}$ the magnetic moment of the nanodot.

Vortex State sample

In fig. 5.9, experimental results obtained for the VS sample are shown. We compare the magnetoresistance obtained for two different states (see figures (a) and (b) in fig. 5.9): (i) the disordered state with random polarity (where the magnetic vortex cores are randomly oriented up or down); (ii) the ordered case with aligned polarity where all the cores are pointing in the positive direction out of plane (this state is achieved by an out of plane field of +20 kOe and switching it off).

In both cases, the magnetoresistance data show new commensurability effects with additional minima (occurring in-between the large, sharp minima) which are generated at fractional matching fields [22, 51].

If we compare the demagnetized state with the saturated case, in contrast to the

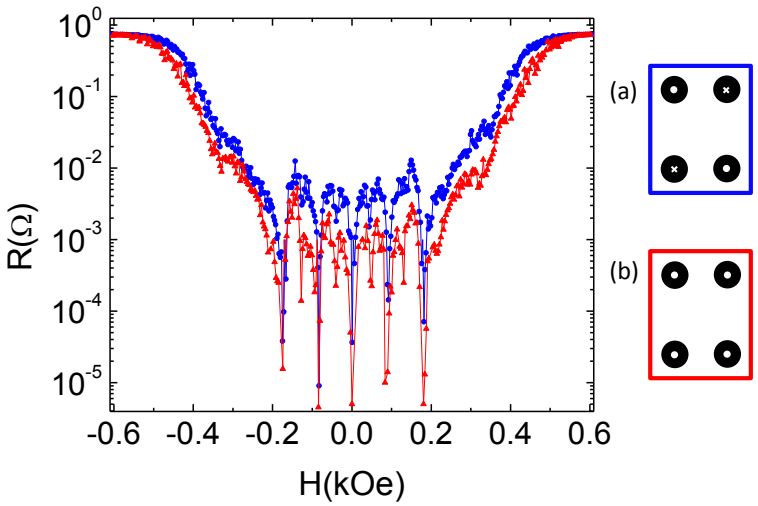

Figure 5.9: Resistance vs perpendicular applied magnetic fields at temperature T=0.985Tc for the sample with vortex state magnetization (VS sample). Blue circles show data obtained for the demagnetized state, red triangles for positive magnetized state.(a) and (b) show a sketch of both states.

trend observed in OP sample in fig. 5.8, the random polarity configuration shows slightly larger dissipation than the aligned polarity case.

In-plane single-domain sample

Finally, we investigate the behavior of the IPSD sample, shown in section 5.3.1, where each dot is in an in-plane single domain state. In this case, the disordered state corresponds to the case where the magnetization direction varies randomly from one dot to another. By contrast, after applying +20 kOe in the plane of the film along the short side of the unit cell and switching it off, an ordered state is obtained where all the magnetizations are pointing in the same direction in the dot plane (see insets in fig. 5.10). Similarly to the VS sample, the ordered state (triangles) shows a decrease in the background relative to the disordered state (circles). In addition, extra minima appear in the ordered state, showing an increase in the commensurability effect.

From the experimental results obtained for the VS and IPSD samples, and taking into account that the local stray field generated by each dot is the same for both ordered and disordered states; a straightforward and consistent picture arises. By ordering the

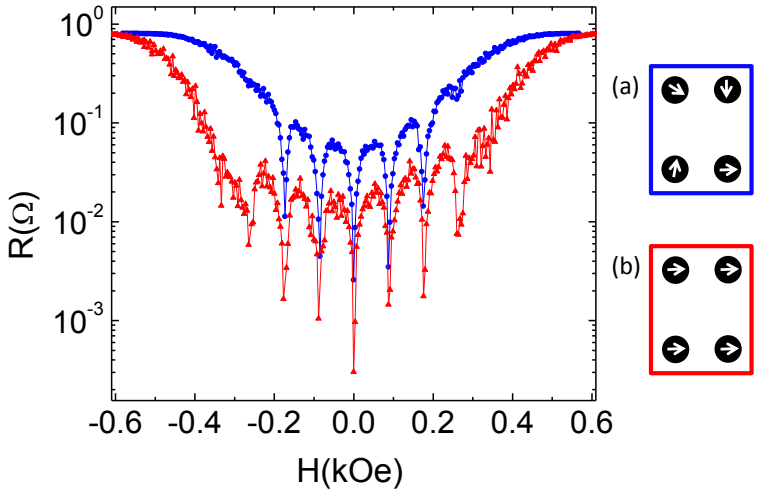

Figure 5.10: Resistance vs perpendicular applied magnetic fields at temperature T=0.985Tc for the sample with single domain in-plane magnetization (SD sample). Blue circles show data obtained for the demagnetized state, red triangles for positive magnetized state. (a) and (b) show a sketch of both states.

local magnetic stray fields created by the nanodots, an ordered magnetic landscape is created, producing an enhancement of the superconducting vortex lattice pinning. This influences the vortex lattice dynamics: first, it strongly reduces the usual monotonous background dissipation in comparison with the dissipation induced by the random distribution. Second, it enhances the commensurability effects and new minima show up.

5.5 Summary

The most important points of this chapter can be listed as follow:

- Co/Pd based nanodots with identical physical dimensions but different relative thickness of the Co/Pd layers produce different magnetic states as shown by the magnetic characterization. The three different configurations are:

  1. Vortex state sample.
  2. In-plane single-domain sample.
  3. Out-of-plane single-domain sample.

- As a result of the different magnetic configurations, the stray fields are systematically tuned. It is shown that dissipation in the mixed state of superconductors can be decreased (increased) by several orders of magnitude by decreasing (increasing) the stray magnetic fields. This result is unexpected since an increase in the magnetic stray field increases the pinning force.

- The relative orientation between the out-of-plane magnetic moment and the superconducting vortices generates an asymmetry in the dissipation as a function of the magnetic field. Parallel(antiparallel) alignment produces an attractive(repulsive) interaction between the superconducting vortex and the nanodot.

- Keeping constant the magnetic stray field, but ordering it over the entire array, helps to reduce dissipation and enhance commensurability effects increasing the number of dissipation minima.

6

Antivortex, interstitial and trapped vortex lattices:

Dynamic response

6.1 Introduction

New effects in vortex matter appear in superconducting hybrids with out of plane magnetized dots due to the strong modulation of the stray magnetic field [78]. For example, under certain conditions related to the magnetization and period of the magnetic nanodots [79], temperature and applied magnetic field [80] or the geometry of the superconductor [81, 82], vortex-antivortex pairs (V-AV) are spontaneously induced in the superconducting film. In an ordered array, vortices are placed on top of the dots whereas antivortices are placed between them [79, 80, 83].

Most of the works published up to date have focused on the static behavior of the V-AV pairs. For example, the creation of the V-AV pairs and their interaction with an external applied magnetic field can be imaged by scanning Hall microscopy[84,

85]. However, eventhough it has been suggested that confinement effects can lead to a different mobility of the V and AV [86], little information is known about their dynamics.

Recently, Kramer *et al.* [15] have studied the vortex-antivortex behavior by scanning Hall microscopy. In this work, they are able to study their dynamics by a scanning ac-susceptibility technique: the vortices are submitted to an external ac field and the points of maximum amplitude of oscilations are recorded for each single vortex. They reported that antivortices can be shaken by small ac field excitation, while the vortices sitting on top of the magnetic structures remain at rest. When the ac field is increased, both vortices and antivortices are set into motion. In summary, they demonstrated that antivortices could be easier subjected to motion than the vortices. However, they cannot quantify the difference in mobility for both types of vortices.

In hybrid samples, the vortex lattice moves on two different pinning landscapes: i) random pinning potentials generated by intrinsic defects in the sample, and ii) periodic and ordered pinning potentials generated by the magnetic nanodots. The competition between these potentials governs the vortex lattice dynamic response. Two extreme regimes can be expected comparing the applied current with the critical current [87]: (i) for driving currents quite close to the critical current, the intrinsic random pinning overcomes the periodic pinning potentials; (ii) for driving currents much higher than the critical current, the vortex lattice moves at very high velocities and the interactions between the pinning centers and the vortex lattice can be neglected. In this regime, the force (current) vs. velocity (voltage) is linear and the vortices move in a free flux flow [5]. In between those two regimes the competition between the random and the ordered pinning governs the vortex dynamics.

The aim of this chapter is the study of vortex dynamics of different types of vortices in the intermediate regime. For this goal, we will use magnetotransport measurements.

6.2 Sample description

Arrays of circular Co/Pd nanodots were fabricated using electron beam lithography following the usual procedure. The nanodots are polycrystalline, arranged on a rectangular lattice (400 nm x 600 nm spacing) covering an area of 100 μm x 100 μm. The dots consist of a $[Pd(0.6nm)/Co(0.4nm)]_{40}$ multilayer, deposited in 12 mTorr Ar atmosphere,

with a 2 nm Pd capping layer to prevent oxidation. The total thickness is 42 nm and the diameter is 230 nm. Magnetic characterizations were performed using vibrating sample magnetometry (VSM) magnetic force microscopy (MFM). The results are similar to those shown in section 5.3.2, so this sample exhibits out of plane magnetization. After the magnetic characterization, a 100 nm thick Nb film was deposited and a cross-shaped bridge was defined for the transport measurements (chapter 2). Small magnetic fields (up to 1kOe) were applied during the transport measurements perpendicularly to the sample plane, which do not alter the remanent magnetic state of the nanodots.

6.3 Ginzburg-Landau Simulations

The Ginzburg-Landau (GL) theory is very useful to reveal the actual vortex lattice configuration and complement the experimental study. It allows to plot the nonuniform distribution of the superconducting order parameter $\psi(r)$; *i.e.* vortex cores can be imaged in this numerical experiment at locations where order parameter drops to zero, and its phase has a whirl of 2π.

6.3.1 Theoretical method

We performed a theoretical analysis using the non-linear Ginzburg-Landau (GL) formalism [5, 9]. Since we are dealing with a type-II superconductor thin film, the formalism reduces to solving the following equation:

$$(-i\nabla - A)^2\psi = (1 - T - \mid \psi \mid^2)\psi, \tag{6.1}$$

where A denotes the vector potential resulting from the total applied magnetic field H (consisting of the stray field h_m generated by the nanomagnets and the applied perpendicular magnetic field H_a, *i.e.*, $\nabla \times \overrightarrow{A} = \overrightarrow{H} = \overrightarrow{H_a} + \overrightarrow{h_m}$), ψ is the superconducting order parameter, and T it temperature scaled to the critical temperature of the sample T_c=8.71 K [74, 79].

We solve eq. (6.1) iteratively by adding a time derivative of ψ on the left side of the equation, where each step of iteration corresponds to the GL time $t_0 = \pi\hbar/8K_BT_c$.

In addition, a random force is include that ensures that only true equilibrium is found. The relaxed numerical solution of eq. (6.1) minimizes the free energy:

$$G/G_0 = V^{-1} \int \mid \psi \mid^4 dV, \tag{6.2}$$

where G_0 equals the superconducting condensation energy $H_{c2}/8\pi$ and V is the volume of the sample [88].

In eqs. (6.1) and (6.2), the distances are expressed in units of the coherence length $\xi_0 = \xi(T = 0)$, the vector potential A is scaled to $\phi_0/2\pi\xi_0$ (where ϕ_0 is the flux quantum), and the order parameter is scaled to its bulk value in absence of field and for zero temperature. The equation is solved in a rectangular simulation region of 4 units cells ($W_x \times W_y$ (800 nm x 1200 nm)) with periodic boundary conditions (so that in practice an infinite film is studied).

To explore the superconducting state, we initialize the calculations from the zero-field cooled state ($H_a = 0$) and $\psi = 1$. Different vortex configurations are obtained and the ground state is determined by finding the minimum in the Gibbs Free energy. After this, we increase the applied magnetic field (H_a) and recalculate the vortex structure using as initial condition the ground state obtained for the previous field.

6.3.2 Vortex, antivortex and giant-vortex

GL simulations allow to distinguish between vortices and antivortices by plotting the phase of the order parameter. In these plots, blue indicates phases near zero and red near 2π. As it can be seen in fig. 6.1, even though in the contourplot of the order parameter both vortex and antivortex are similar (both drops to zero, see fig. 6.1(a)), when we examine the phase plot, there is a clear difference: by going around each single vortex, the phase changes from 0 to 2π in opposite directions (see fig. 6.1(b)). This 2π change defines the so-called vorticity (L) and equals 1 in the case of the vortex and -1 in the case of the antivortex. This, allows us to distinguish between V and AV and can be corroborated by plotting the screening currents.

The vorticity allows us to detect the presence of giant vortices as well (single multiquanta vortex). In this case, the Cooper-pair density drops to zero, as in the case of single vortices, but there is a multiple 2π phase change around them. The vorticity L

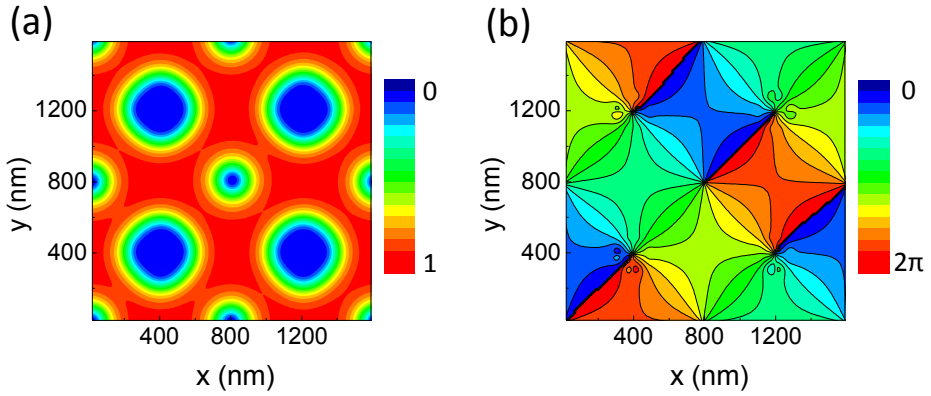

Figure 6.1: (a) and (b) show the cooper pair density and the phase of the order parameter respectively obtained in a sample with positive magnetic remanent state of the nanodots where vortex and antivortex are present. In (a) Blue/Red color corresponds to low/high Cooper pair density and in phase near $0(2\pi)$ are given in blue(red).

is defined as the number of times that the phase changes from zero to 2π and describes the number of vortices that form the giant vortex.

6.4 Theoretical and experimental results

Vortex lattice configuration

Fig. 6.2(a) shows the magnetoresistance data obtained at T=0.99T_c, on the hybrid sample with $[Pd(0.6nm)/Co(0.4nm)]_{40}$ multilayer nanodots. As shown previously, the dependence of the resistance on the magnetic field is very different depending on whether the applied magnetic field corresponds to matching condition or not, so the commensurability effect is observed section 1.3.2. However, in this case, a clear asymmetry appears in the magnetoresistance curves. The results shown in fig. 6.2(a) correspond to two configurations of the remanent state: one with the positive remanent magnetization ($m_z > 0$) obtained with the saturating field in the positive direction, and the other for the negative saturating field ($m_z < 0$). The periodic minima distribution shows a clear asymmetry around H_{match} (-H_{match}) for the positive (negative) remanent configuration, with more minima observed when the magnetic moment lies parallel

to the external magnetic field (in positive fields for the $m_z > 0$ configuration and in negative fields for $m_z < 0$ configuration).

This observed asymmetry can have two different origins. On one hand, the pinning strength depends on the relative alignment between the magnetic moments of the dots and the external applied magnetic field. If the polarity of the superconducting vortex and the magnetization of the dot are parallel, the vortex is attracted by the dot. The opposite occurs if the two are in opposite directions; the superconducting vortex is repelled by the magnetic dot and resides at interstitial positions between the dots (see section 5.4.2). Another possible origin is the nucleation of vortex-antivortex (V-AV) pairs by the magnetic dots. In this case, the asymmetry is produced by the annihilation of one of them by the external magnetic field.

To determine the origin of the observed asymmetry in the magnetoresistance curves shown in fig. 6.2(a), we perform a theoretical study of our system at T=0.99T$_c$. For that, we use the GL formalism explained above to simulate a 100 nm thick Nb film (ξ_0= 9 nm) grown on top of a rectangular array (400nm x 600 nm) of out of plane magnetized Co nanodots (40 nm thick and 230 nm diameter) with positive magnetization ($m_z > 0$). Co saturation magnetization was rescaled from 1400 G to 560 G (16 nm of Co out of 40 nm total thickness of the Co/Pd multilayer) to simulate the average magnetization of the nanodots.

First of all, we analyze the calculated free energy *vs.* the magnetic field normalized to the first matching field (H$_{match}$) fig. 6.2(b). A clear asymmetry is observed around the +H$_{match}$ and it is in agreement with the experimental results shown in fig. 6.2(a). The global minimum of the free energy– highlighted by a circle – is reached at the first positive matching field. This minimum proves that states with vortices have lower energy than those without them. This may be due to two reasons: (1) the energetically favorable compensation of the vortex currents and the screening currents over the dots (where vortices are pinned), and (2) the nucleation of a V-AV pair over each dot and subsequent annihilation of antivortices with vortices due to external field. To clarify the underlying mechanism for this phenomenon, we calculate and visualize the nucleation and stabilization of vortex states in our system.

Using the GL approach we obtained the ground state configuration for different number of vortices per unit cell, *i.e.* under different (fractional and integer) matching

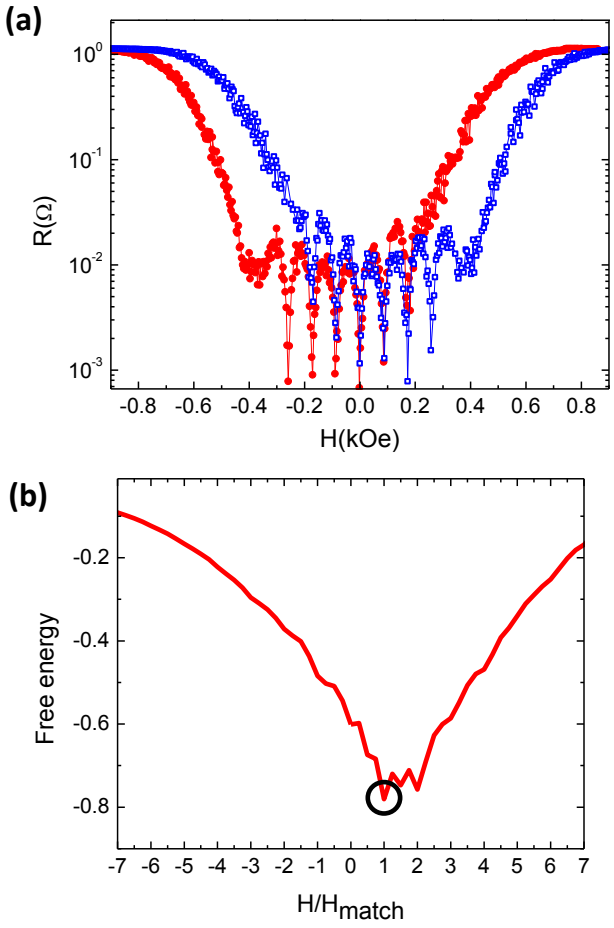

Figure 6.2: (a) Resistance (R) as a function of the magnetic field (H) at T=0.99T_c with I=3 mA and T_c=8.71 K. Red filled circles correspond to the curve obtained for negative remanent magnetization and blue hollow squares to the positive remanent magnetization. (b) shows the Gibbs free energy as a function of the external magnetic field.

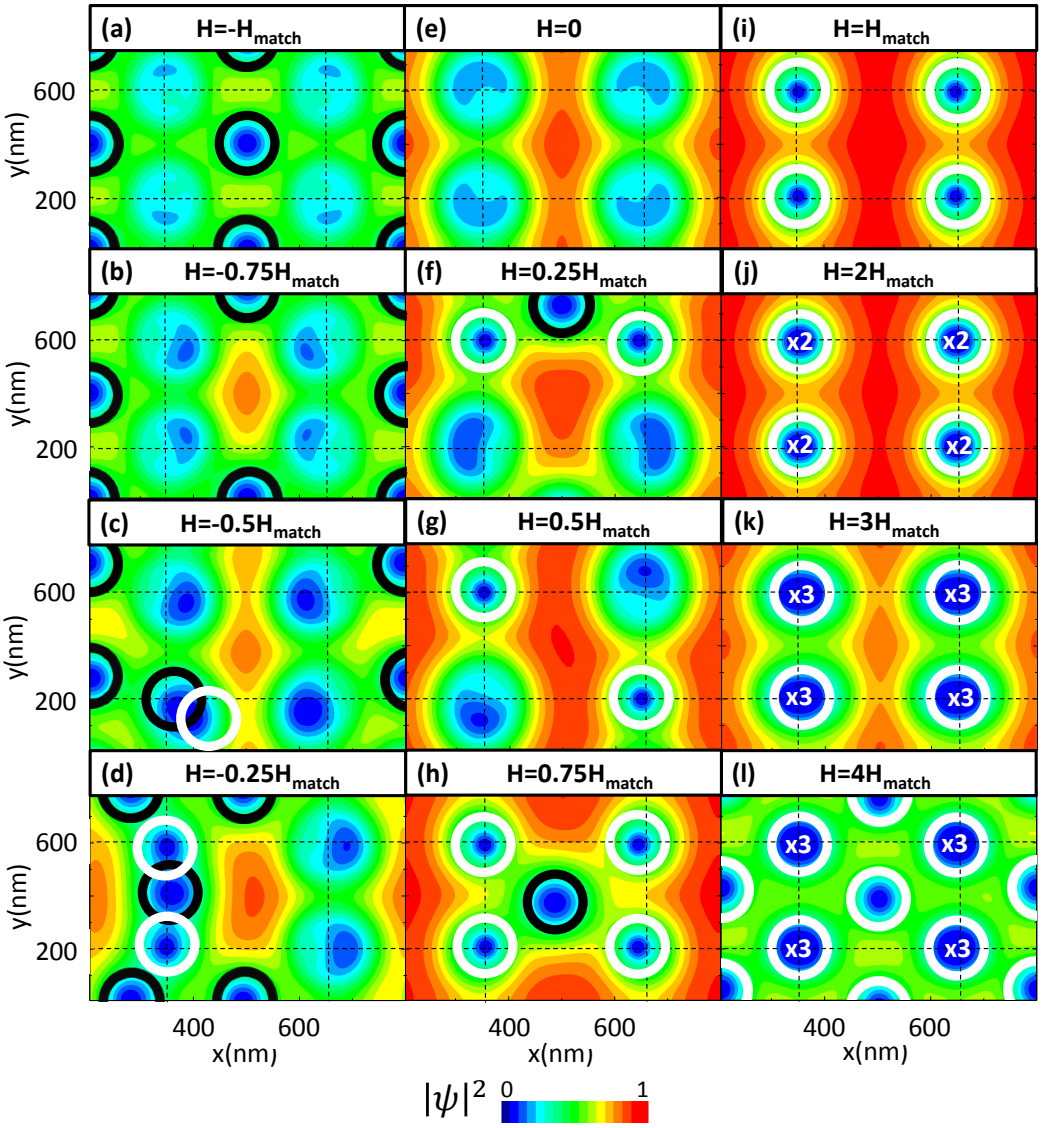

Figure 6.3: Contourplots of the Cooper pair density for the ground state vortex configurations obtained in a sample with positive magnetic remanent state of the nanodots. Different applied magnetic fields are shown from H=-H_{match} (a) to H=4H_{match} (l). Blue/Red color corresponds to low/high Cooper pair density, white/black circles show the position of the vortices/antivortices and dashed lines indicate the unit cells of the periodic lattice of nanodots.

fields. Fig. 6.3 shows the contourplots of the Cooper pair density of the ground state vortex configurations obtained for a magnetic array of dots with positive magnetization ($m_z > 0$) for different values of the applied magnetic field ranging from (a) H=-H_{match}, *i.e.* first negative matching field to (l) H=4H_{match}, *i.e.* four times the value of the first matching field. Both, the density of states and the phase have been plot so that vortices and antivortices can be distinguished. For clarity, only the density of states is plotted and white/black circles indicate the position of the vortices/antivortices. Dashed lines indicate the unit cells of the periodic lattice of nanodots.

Fig. 6.3(e) shows the contour plot configuration obtained for H=0. It is clear that for zero field no V-AV pairs are induced in the sample. However, fig. 6.3(d) and 6.3(f) show that, under a small applied magnetic field (H=$\pm$0.25H_{match}), V-AV pairs are induced in the system as was predicted earlier [80]. This is probably because V-AV pairs cannot be separated and stabilized since the magnetic lattice is too dense compared to the coherence length at this temperature (the lattice parameters are 400 nm and 600 nm and $\xi(0.99T_c)$= 90 nm), however, a small magnetic field can activate the nucleation of the V-AV pairs by compensation of the screening currents over the nanodots, which leads to larger effective interstitial space for nucleated antivortices. This suggests that vortex-antivortex creation and annihilation processes are essential in the analysis of the energy spectrum of the superconducting state of our system.

To corroborate this antivortex annhilitation by the external magnetic field we show in fig. 6.4 the evolution of the free energy for H=H_{match}. As it was explained before, the initial state corresponds to the one obtained for the previous field, so state (1) corresponds to the vortex configuration obtained for H=0.75H_{match}, for which one antivortex is placed in the interstitial position. Then, the external vortex induced by the applied magnetic field enters the observed area (states (2) and (3)), until it annihilates with the existing antivortex (state (4)) and the ground state is obtained. Therefore, the optimal superconductivity is obtained for H=H_{match} (where a minimum in the free energy is found (fig. 6.2(b))) due to the most favorable compensation of currents in the system (i.e. minimized supercurrents due to compensation of Meissner currents over the dots with currents of vortices sitting on the dots), but also due to the annihilation of the interstitial antivortices by the external applied magnetic field (see a sketch of the annihilation in fig. 6.4(b)).

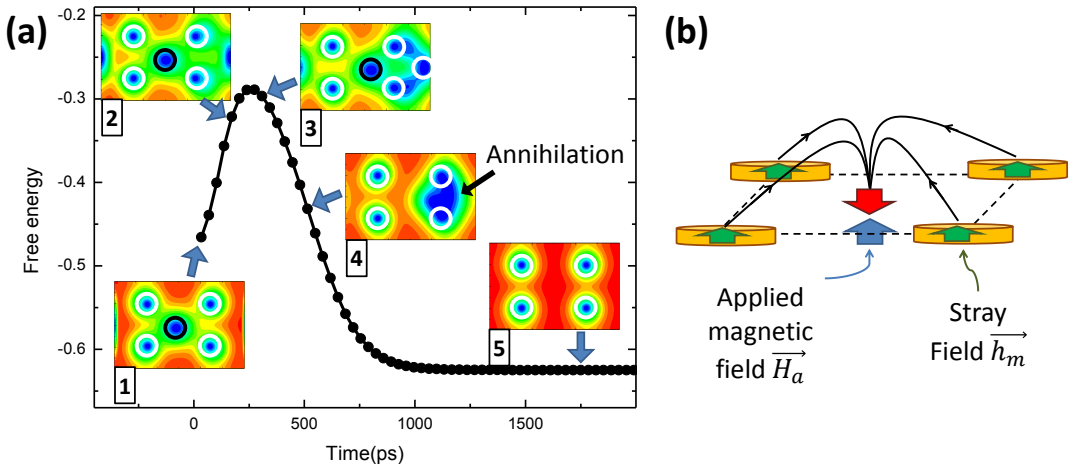

Figure 6.4: (a) Simulated free energy as a function of time: State 1 shows the initial state, which corresponds to H=0.75Hmatch (fig. 6.3(h)). States 2, 3, 4 show the snapshots of the annihilation process and state 5 shows the final state (fig. 6.3(i)). (b) shows a sketch of the antivortex annihilation process for H=H$_{match}$.

In summary, for H=H$_{match}$ only vortices on top of the dots are obtained: the external magnetic field annihilates the antivortices generated by the magnetic dots and only vortices are established in the ground state. For higher matching fields, $2H_{match}$ and $3H_{match}$, more vortices are pinned on the dots, where they coalesce into a giant vortex (with vorticity L=2 and L=3 respectively). Opposite process occurs for H=-H_{match}, in this case the external magnetic field annihilates the vortices placed on top of the dots and an antivortex lattice is established at the interstitial positions of the array, while dots remain vortex-free. This state is unstable under applied drive since interstitial antivortices are very loosely bound to the dots.

Finally, we point out one more particular state, namely for H=$4H_{match}$, where we find that a three-quanta giant vortex is placed on top of the dots and an extra vortex appears in the interstitial position of the dot array. This can be seen in the magneto-resistance curves showed in fig. 6.2(a), where the fourth minimum is shallower and less defined than the first three minima. This is a fingerprint that the fourth minimum corresponds to a vortex configuration in which an interstitial vortex appears as is shown in fig. 6.3(l). Dots of similar dimensions tend to show a vortex occupation number equal to one [20]; however, the out of plane magnetization of the dots increases

the filling factor up to three in the present case [15].

From these results we conclude that the combination of suitable magnetic pinning potentials and appropriate applied magnetic fields (number of vortices in the unit cell of the array) allows discrimination between different kinds of vortices in the sample, so that commensurability effects become a tool to distinguish between different types of vortices and study their dynamics.

Vortex lattice dynamics

We perform the following experimental procedure to study the vortex lattice dynamics. First, we apply the appropriate magnetic field to establish a certain vortex configuration and we keep it constant. Then, we apply a current density $\overrightarrow{J}$. As was explained in section 1.2.3, $\overrightarrow{J}$ yields a Lorentz force on the vortices, $\overrightarrow{F_L} = \overrightarrow{J} \times \overrightarrow{n}\phi_0$, where $\overrightarrow{n}$ is the unit vector along the field direction. Above a threshold current, this force sets the vortex lattice into motion with average velocity $\overrightarrow{v}$. Force-velocity curves (F_L vs. v) can be extracted from the experimental I-V characteristics by calculating the Lorentz force and using the Josephson relation for the electric field $\overrightarrow{E} = \overrightarrow{B} \times \overrightarrow{v}$. Force-velocity curves measured at two different fields: at matching field $H_{matching}$ and at a smaller field value $H_{outofmatching}$ close to $H_{matching}$ but far enough to be out of matching conditions have been obtained to extract the force enhancement $\Delta F_L = F_{L_{matching}} - F_{L_{outofmatching}}$. This is a measure of the driving force enhancement at matching conditions where a vortex lattice is moving with long range order induced by the ordered potential landscape. In addition, by plotting ΔF_L vs. vortex lattice velocity we can detect the velocity range for which the interaction between the ordered pinning and the different types of vortices is observable.

We have chosen three experimental conditions to explore the relevant dynamics of three different lattices: i) antivortex lattice, i.e. one interstitial antivortex per unit cell, placed in its center (fig. 6.3(a)), ii) trapped single vortex lattice, *i.e.* single vortex sitting on each dot (fig. 6.3(i)), and iii) vortex lattice with trapped giant vortex and single interstitial vortex, *i.e.* giant vortex at each dot and one interstitial vortex in the center of the unit cell (fig. 6.3(l)). Fig. 6.5(a) shows the results for the three situations

considered: isolated antivortex (circles), vortices placed on the dots (stars), and finally interstitial and pinned vortices (squares).

First of all, we observe that the vortex dynamics are sensitive to the type of vortex which is moving. Taking into account that the highest value of ΔF_L indicates the most ordered moving lattice, the vortex lattice consisting of "pinned" vortices (H=H$_{match}$) shows an enhancement in their interaction with the pinning landscapes. This is indicative of the strong attractive interaction between a vortex line and a magnetic moment aligned parallel to it and it renders in the largest vortex velocity interval where the order occurs. On the other hand, the motion of antivortices (H=-H$_{match}$) can be considered as scaled down in comparison with that of the vortices (H=H$_{match}$). In this case, the antivortices experience a repulsive interaction with the magnetic dots and the origin of the pinning is a "caging effect". This interaction results in a weaker pinning, and a ΔF_L reduction is observed. In addition, the velocity range where the ordering takes places is reduced. Finally, we have studied the results obtained for the vortex lattice with interstitial vortices (H=4H$_{match}$ in fig. 6.3(l)). In this case, the interaction between the pinned vortices and the interstitial vortices makes the vortex lattice stiffer and the onset velocity is shifted to higher values.

Additionally, from the experimental results we can estimate the necessary forces to move a vortex or an antivortex lattice and quantify the difference in the pinning strength. Fig. 6.5(b) shows the experimental results using the normalized Lorentz force difference $((F_{L_{n=+1}} - F_{L_{n=-1}})/F_{L_{n=-1}})$, where $F_{L_{n=+1}}$ and $F_{L_{n=-1}}$ are the Lorentz forces needed to move the vortex and antivortex lattices at a certain velocity, respectively. We observe that the force required to start moving the vortex lattice is 65% higher than that for the antivortex. Once they are moving, we observe a plateau around 40% which spands over three orders of magnitude for the velocity. When the velocity is high enough so that the interaction between the vortex/antivortex lattice and the pinning array is overcome and the free flux flow regime is reached, this difference vanishes.

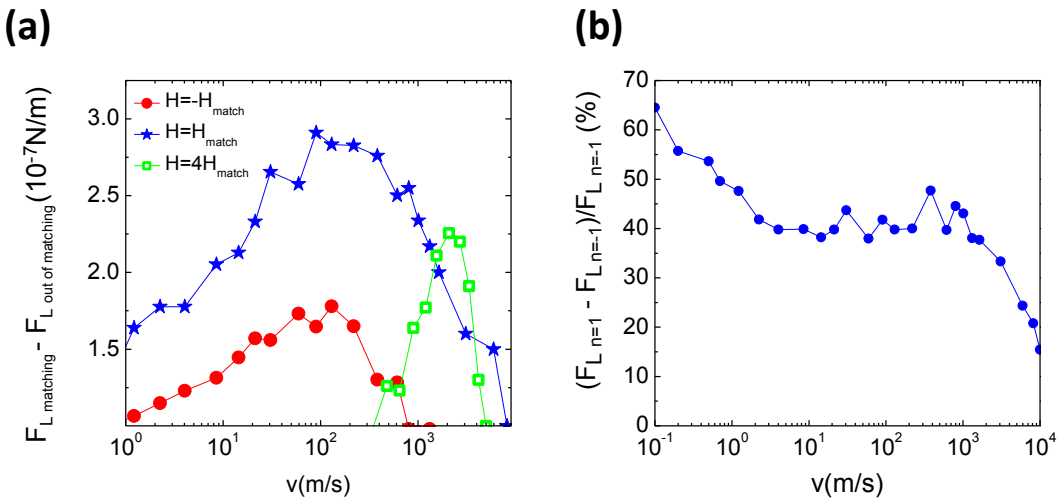

Figure 6.5: (a) Force enhancement ($\Delta F_L = F_{L_{matching}} - F_{L_{outofmatching}}$) as a function of the vortex lattice velocity at 0.99T$_c$. Red circles show the pinning enhancement for H=-H$_{match}$, blue stars for H=H$_{match}$ and green squares for H=4H$_{match}$. (b) Velocity dependence of the normalized difference of the Lorentz Force needed to move a vortex and an antivortex ($(F_{L_{n=+1}} - F_{L_{n=-1}})/F_{L_{n=-1}}$) at T=0.99T$_c$. Note that the force needed to start moving a vortex is 65% higher than the needed to start moving an antivortex. Once they are moving, the difference is 40% until the velocity is high enough so that interaction between vortex lattice and pinning array is overcome.

6.5 Summary

The most important points of this chapter can be listed as follow:

- Inhomogeneous magnetic field generated by an array of dots with perpendicular magnetization can induce the formation of vortex and antivortex pairs in a superconducting film. In our system, a small external magnetic field induce the spontaneous formation of V-AV pairs.
- Commensurability effect and Ginzburg-Landau simulations have been used to stablish different types of vortex lattices:
  1. Pure antivortex lattice.
  2. Vortex lattice with all vortices pinned on the dots.
  3. Vortex lattice with pinned and interstitial vortices.
- The dynamics of the different vortex lattices have been studied:
  1. The pinned vortex lattice shows the strongest interaction between the periodic array and the vortex lattice, whereas the antivortex lattice exhibits a lower pinning interaction.
  2. We have estimated that the force needed to start moving the vortex lattice is around 65% higher than the one needed to move the antivortex one.
  3. In the case of the vortex lattice with pinned and interstitial vortices, the onset in velocity where the lattice becomes ordered increases.

7

Magnetic Ratchet:

Fe single-crystal nanotriangles

7.1 Introduction

Since the experimental work of Villegas et al. [28], many researchers have studied different types of superconducting vortex ratchets, see for example references [57, 89, 90]. In vortex ratchet, the broken inversion symmetry of the pinning potential landscape can be generated either by geometric [22, 28, 57, 89–91] or by magnetic asymmetries [92, 93] independently.

As previously mention in chapter 1, the lack of inversion symmetry in the geometry of the pinning array can be achieved in different ways. For instance, the symmetry can be broken through an asymmetric arrangement of symmetric pinning centers [22] or through an asymmetric shape of the pinning sites [28]. As can be seen in fig. 1.6(a), the triangular shape of the pinning sites generates an asymmetric potential that produces the vortex ratchet effect (fig. 1.6(b)).

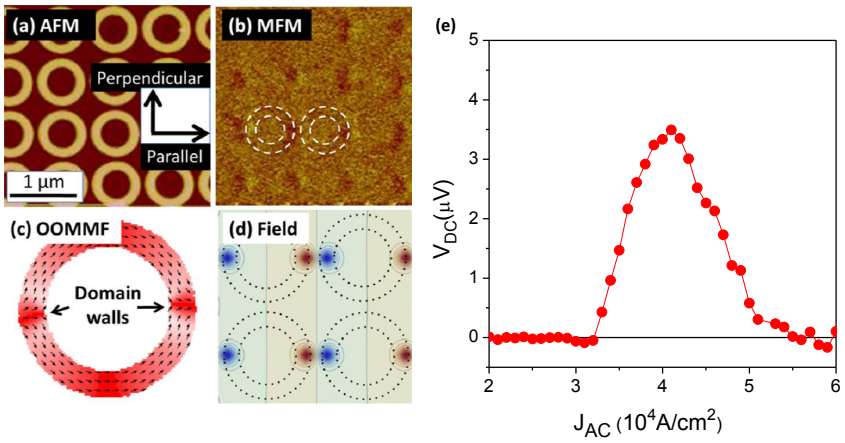

Figure 7.1: (a) AFM image of the sample. (b) MFM images of part of the sample after being magnetized into onion state. (c) OOMMF simulation of an onion state with the 180° domain walls indicated. (d) Out-of-plane field at a height of 60 nm above the rings in the onion state. From Perez de Lara *et al.* [94]. (e) Ratchet effect at 0.97T$_c$ obtained for vortex motion along the direction of the domain walls shown in (c). From Perez de Lara *et al.* [93].

On the other hand, the asymmetry can be also generated by magnetic potentials [92, 93]. By tailoring the magnetic stray field produced by a symmetric nanostructure, an asymmetric potential can be generated and the ratchet effect is induced by pure magnetic potentials. For example, in the work of Perez de Lara *et al.* [93], the asymmetric potential is obtained by the presence of domain walls in Ni nanorings. As can bee seen in fig. 7.1, when vortex motion is parallel to the domain walls, a ratchet signal is obtained.

It was shown section 1.2.3 that the electric field $\overrightarrow{E}$, the vortex-lattice velocity $\overrightarrow{v}$ and the magnetic induction $\overrightarrow{B}$ can be related by:

$$\overrightarrow{E} = \overrightarrow{B} \times \overrightarrow{v}, \tag{7.1}$$

Therefore, in the V$_{dc}$ *vs.* I$_{ac}$ signal, the voltage dc drop probes the time averaged vortex-lattice velocity $\langle v \rangle = V_{dc}/dB$, where d is the distance between the voltage contacts. By taking into account these simple relations, the dominant type of ratchet effect in a sample can be identified as follows:

- In samples exhibiting vortex ratchet effects of geometric origin, the inversion of the perpendicular magnetic field $\overrightarrow{B}$ produces the inversion of the electric field $\overrightarrow{E}$ because the velocity $\overrightarrow{v}$ of the vortex lattice is not reversed. Thus, the sign of the dc voltage is sensitive to the field polarity ($\overrightarrow{B}$).

- In samples which vortex ratchet effects have a magnetic origin, the inversion of the perpendicular field $\overrightarrow{B}$ polarity reverses the vortex lattice velocity $\overrightarrow{v}$. As a result, the electric field $\overrightarrow{E}$ is not reversed and the output voltage V_{dc} is insensitive to the field polarity. However, if we reverse the (in-plane) magnetization of the pinning centers, while preserving the polarity of the perpendicular magnetic field, the velocity is also reversed. In this latter case, the output dc voltage changes sign.

Thus, the ratchet origin can be experimentally identified: for purely geometric asymmetry, the ratchet effect is odd with the polarity of the applied magnetic field, *i.e.*, reversing the magnetic field reverses the sign of V_{dc}. On the other hand, for purely magnetic asymmetry the ratchet effect is odd with the direction of the magnetization configuration of the pinning centers, *i.e.* reversing the magnetization reverses the sign of V_{dc}. However, ratchet effect is even with the applied magnetic field, *i.e.* reversing the magnetic field does not reversed the sign of the V_{dc}.

Besides this behavior, as was mention in chapter:sust, geometric vortex ratchet effects are sensitive to the presence of interstitial vortices which allows tuning the polarity of the vortex ratchet upon increasing the strength of the driving current (vortex ratchet reversal). In the case of pure magnetic ratchet, by contrast, the polarity of the ratchet effect is constant, although interstitial vortices exist in the sample [93]. Thus, the presence of ratchet reversal is a fingerprint of geometric ratchet effect.

In this chapter, hybrid samples based on Fe single-crystal nanotriangles embedded in Nb films are studied. In these type of samples, both types of asymmetries (geometric and magnetic) coexist. On one hand, the geometric asymmetry is achieved by the triangular shape of the pinning sites and it cannot be manipulated. On the other one, by tailoring the magnetic stray fields generated by different magnetic remanent states in the nanotriangles, an asymmetric pinning potential can be generated and, moreover,

can be easily manipulated. Hence, in this type of samples we can study both types of ratchets and the interplay between them when they coexist in the same direction.

7.2 Sample Description

The hybrid samples are arrays of Fe triangles embedded in Nb films. The Fe triangles were patterned by means of electron beam lithography (EBL) on epitaxial Au(001)/Fe(001)/MgO(001) films deposited by Pulsed Laser Deposition (PLD), using a Nd-YAG laser ($\lambda = 532$ nm, 4 ns pulses, 25 mJ/pulse). The Fe (001) films, 25 nm thick, were deposited at room temperature on MgO (001) substrates, previously annealed for water desorption for 25 minutes at 200 °C. After PLD deposition the films were annealed at 400 °C in order to improve their crystalline quality and surface roughness. Then a Au (001) capping layer, 10 nm thick, was deposited at room temperature by Molecular Beam Epitaxy (MBE) to prevent the oxidation of the Fe layer. The whole process was carried out under ultra-high vacuum conditions. A detailed structural analysis by x-ray diffraction and x-ray reflectivity evidenced the excellent crystalline structure of the films, and very sharp and flat Au/Fe and Fe/MgO interfaces, respectively. Those results confirmed the existence of a single in-plane crystalline domain with the Fe lattice rotated 45° with respect to that of the MgO.

Two arrays, covering an area of 500 x 500 μm^2, were lithographed by e-beam lithography(EBL). After the developing, an Ar^+ ion etching was carried out. The patterned motifs in both arrays are triangles which dimensions were chosen to be the same than those in reference [28]. The two fabricated arrays present different relative orientations of the Fe crystalline directions, and the axes defined by the motifs base (X axis) and base-to-tip line (Y axis). Array-1 is oriented with the [100] and [010] Fe directions rotated 45° with respect to the XY frame so that the easy axes are almost parallel to the other two sides of the triangle. Array-2 is oriented with the X-axis parallel to the base of the triangles and the Y axis parallel to the Fe [010] direction. So, in this situation, the X and Y axes are coincident with the Fe magnetocrystalline easy axes along [100] and [010] directions, respectively. The morphological characterization of the nanopatterned arrays was performed by SEM providing information about the shape and quality of the triangles as well as their dimensions, which are: i) Array 1:

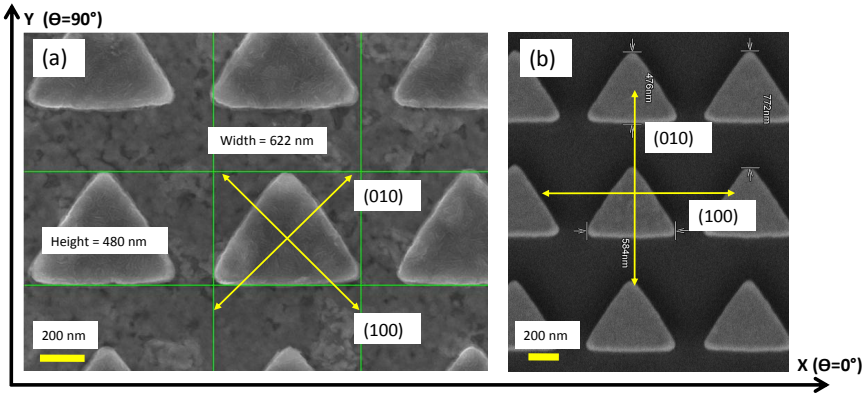

Figure 7.2: SEM images of Array-1 (a) and Array-2 (b) showing the dimensions of the triangles, the configuration of the crystalline axes and the XY frame.

base, 620 nm; base to top, 480 nm and x (y) separation, 150 (270) nm; ii) Array 2: base, 580 nm; base to top, 475 nm and x (y) separation, 160 (295) nm (see fig. 7.2).

After the magnetic characterization of the arrays, a 100 nm thick superconducting Nb film was deposited on top of them and a cross-shaped 40 μm wide bridge in the magnetic/superconducting hybrid sample was defined to perform the magnetotransport measurements using the usual procedure (see section 2.1).

7.3 Magnetic Characterization

Different energy contributions governs the magnetization reversal mechanisms in magnetic nanostructues. In the specific case of arrays of magnetic dots, the geometry (shape and size) usually gives rise to an internal magnetostatic energy term related to the symmetry of the dots, the so-called configurational anisotropy [95], which might yield striking magnetization configurations. In the intermediate range between the single and multidomain regime, magnetic vortices - low magnetization, flux closed structures - appear to reduce the internal dipolar energy [68, 69]. In the case of dots patterned on polycrystalline isotropic films or on low anisotropy materials (such as Co, Ni and Py samples studied in previous chapters), where magnetocrystalline anisotropy does not play an important role, the configurational anisotropy makes the magnetic vortex

state the most stable configuration. So, for magnetic dots of 200 nm diameter and 40 nm thick of Co, Ni, Py or for the Ni nanotriangles studied in reference [28], the stable configuration is a magnetic vortex state and no magnetic asymmetry can be induced in these systems [96–99]. This is the reason why, in this work, we have chosen Fe single-crystal nanotriangles, where the magnetocrystalline anisotropy plays a major role[98, 100]. In this case, different magnetic configuration might be induced as the result of the interplay between the dipolar interactions, shape and magnetocrystalline anisotropies.

The magnetic characterization was performed by in-plane hysteresis loops measured by magnetometry on a magneto-optical Kerr effect (MOKE) system at room temperature. The system allows measuring the angular dependence of the hysteresis processes and both components of the magnetization, parallel and perpendicular to the applied field, under a maximum applied field of 5 kOe. The magnetization configurations were analyzed from the results of micromagnetic simulations carried out using two-dimensional OOMMF code [36] with 5 nm x 5 nm cell size and 25 thickness. The intrinsic Fe parameters were $M_s = 1.7 \cdot 10^6$ A/m, $A = 21 \cdot 10^{-12}$ J$\cdot$ m^{-1} and $K_1 = 48 \cdot 10^3$ J $\cdot$ m^{-3}, being M_s the saturation magnetization, A the exchange constant, and K_1 the magnetocrystalline anisotropy constant [35]. The cell size used for the calculations is below the typical Fe exchange length, which is close to 50 nm.

As a first step, the hysteresis loops of both arrays were measured with the field applied parallel (Θ=0°) and perpendicular (Θ=90°) to the base of the triangles. As can be seen in fig. 7.3 (c) and (d), the loops of Array 2 have a clearly constricted shape, with well defined nucleation and annihilation fields, H_n and H_{an}, which correspond to the low and high field magnetization jumps, respectively [69], whereas the constrictions of the loops of Array 1 (fig. 7.3 (a) and (b)) are not so evident, which suggest a broad distribution of H_n and H_{an}. The remanence-to-saturation ratios of the loops in Array 2 (0.83 and 0.42, for Θ=0° and Θ=90°, respectively) are higher than their counterparts in Array 1 (0.6 and 0.3, respectively), which is due to the coincidence of the magnetocrystalline easy axes with the x and y directions in Array 2. In spite of the differences in the shape of the loops, due to the orientation of the crystalline axes, lower susceptibility and remanence values are obtained in the loops measured in both arrays at 90°. This is due to the large magnetostatic energy required to keep the

magnetization vertical, related to the high density of magnetic poles appearing at the base. In addition to it, when the field is applied parallel to the base, *i.e.*, pointing in the positive x direction, the interactions between negative and positive poles that appear at the left and right corners of neighboring triangles, respectively, help decreasing the dipolar energy, which contributes to the higher susceptibility and remanence.

Micromagnetic simulations have been used to calculate the loops for Θ=0° and Θ=90° for both arrays (fig. 7.3, red lines). The simulations confirm that the hysteresis loops measured with the field parallel to the base present a higher susceptibility and remanence and also that the loops corresponding to Array 2 have more constriction than those of Array 1. In general, a good qualitative and quantitative agreement between the calculated and measured hysteresis parameters (remanence, nucleation and annihilation fields) has been obtained for Array 2. However, for Array 1, remanence of the calculated Θ=90° hysteresis loop is smaller than the experimental one.

This simulations give us the opportunity to study the magnetic configurations for different applied magnetic fields. Fig.7.4 (a) and (b) show the configurations obtained for Array 2 for different applied magnetic fields parallel (Θ=0°) and perpendicular (Θ=90°) to the base of the triangles respectively. States 1 and 4 correspond to the positive and negative saturation configuration and states 2 to the remanence configuration. States 3 correspond to the magnetization configuration obtained for the coercivity field showing that, in both directions, the magnetic reversal mechanism is mediated through the formation of a magnetic vortex. Similar states have been obtained for Array 1 for (Θ=0°), whereas, for (Θ=90°) the remanence corresponds to a vortex state as can be extracted from the low magnetization obtained for H=0 Oe in the hysteresis loop in (fig. 7.3(b),red line).

The remanent configuration deserves special attention: after saturation parallel to the base (Θ=0°), the remanence consists (fig. 7.4(a), state 2), for both arrays, on a highly symmetrical structure resembling a "c state" with null vertical magnetization component in agreement with previous results reported for Permalloy triangles [101, 102]. For both arrays, the magnetization is essentially parallel to the base and sides of the triangles to reduce the dipolar energy even though, in the case of Array 2, this occurs at the expenses of the magnetocrystalline energy due to the orientation of the crystalline axes.

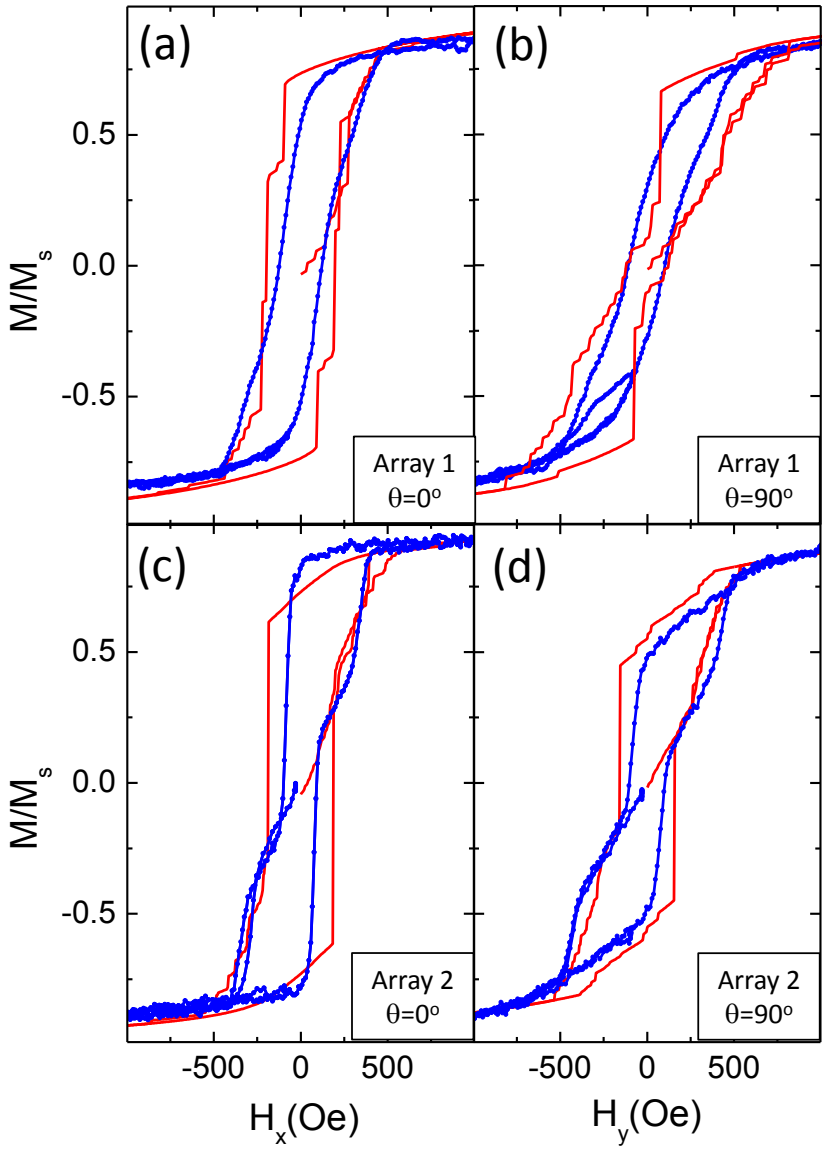

Figure 7.3: Calculated (red solid line) and experimental (blue dots) hysteresis loops for Array 1 and Array 2 for different applied field directions: (a) and (c) show the hysteresis loop with the field applied parallel (Θ=0°) to the base of the triangles and (b) and (d) for applied field perpendicular to the base (Θ=90°) for Array 1 and 2 respectively.

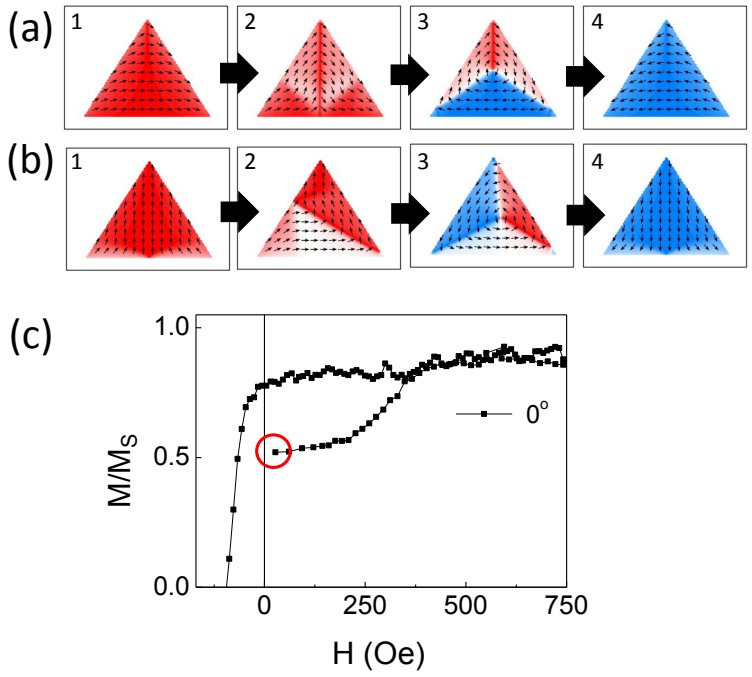

Figure 7.4: Magnetization configurations obtained by micromagnetic simulations for Array 1 for different applied magnetic field parallel (a) and perpendicular (b) to the base of the triangles. States 1 and 4 correspond to the positive and negative saturation, states 2 show the remanence configurations and states 3 show the coercivity configurations. (c) shows the initial magnetization and demagnetization branch of the hysteresis loop of Array-2 measured along the X axis, after previous saturation along the Y axis.

When considering the remanence after saturation along the Y-axis, studies done in Permalloy triangular dots, where the magnetocrystalline anisotropy does not play an important role, have shown that two possible states can be found: the "y" configuration (where the magnetization fans in from the corners to the tip) and the "buckle" configuration (where magnetization tends parallel to the base toward the tip)[101, 102]. In our case, for Array 2, the vertical base-to-tip axis is a symmetry axis along which the magnetocrystalline anisotropy is a minimal. Thus, a highly symmetric configuration similar to "y" state is likely to appear. However, the "y" state is proved to be stable just under very restrictive conditions and, even in Permalloy, a "buckle" state usually appears. Any small perturbation breaking the symmetry gives rise to a non symmetric configuration with the magnetization essentially parallel to the base in the lower left region and vertical in the upper region, giving rise to a non-null magnetization along the base direction. Micromagnetic simulations show that in our case, the remanent configuration corresponds to the "buckle" state, (see state 2 in fig. 7.4(b)). To confirm experimentally this configuration, we have carried out a routine as follows: the array was first saturated applying a vertical field and then it was kept in its remanent state, the sample was rotated and a loop with the field applied parallel to the base was measured. As can be seen in fig. 7.4(c), the initial point of the obtained hysteresis loop corresponds to a reduced magnetization value of 0.5, approximately, in good agreement with the value calculated from the configuration of state 3 in fig. 7.4(b) (0.48). This experimentally confirms that the remanent configuration corresponds to the "buckle" state with a non-null horizontal magnetization component.

In this case of Array 1, micromagnetic simulations show a vortex state at remanence with positive nucleation field. This will be proved by the experimental results as we will show in the following discussion.

A relevant issue regarding the magnetization processes of the dots is related to the conditions for the nucleation of vortices during the demagnetization from saturation. The stability of the vortices gives rise to irreversibilities in the half loop once a vortex is nucleated, which can occur even at positive fields due to large internal demagnetizing fields. This is, for a fixed reversal field, if the magnetic vortex has been nucleated, when the dots are remagnetized by increasing the field back to saturation, the ascending branch lies below the descending one until the annihilation field is reached [67]. Fig.

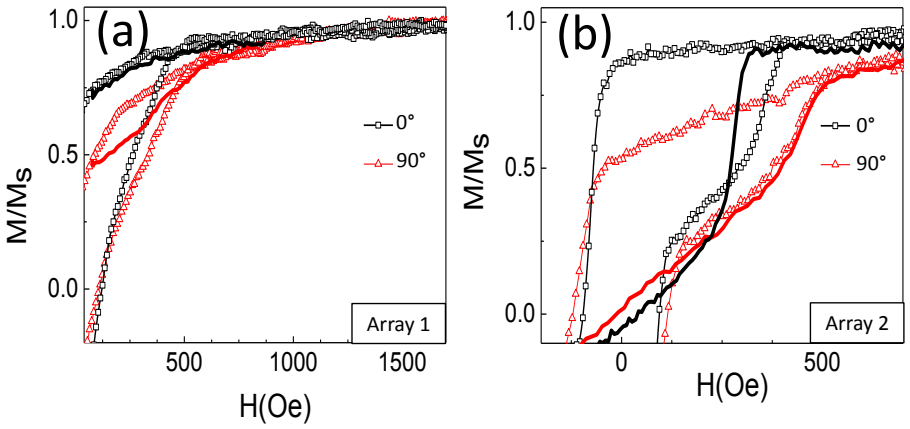

Figure 7.5: Figures (a) and (b) compare the half loop (solid lines) to the full loop (symbols) for Array 1 (a) and Array 2 (b).

7.5(a) shows the half loop branch of Array 1 obtained from remanence. For Θ=90° the obtained ascending branch lies below the full loop, which reflects that, for some triangles, the vortex nucleation field is positive and that, at remanence, some of them will exhibit vortex state configuration. This shows the instability of this state due to the large dipolar fields that appear when the triangles are magnetized along the vertical direction. In contrast, when the field is applied parallel to the base of the triangles (Θ=0°), the demagnetization to remanence and half loop magnetization processes are fully reversible, indicating lower dipolar fields and the higher stability of this state due to the interactions between neighboring triangles.

In the case of the loops obtained of Array 2, if we perform the same measurements from remanence, the remagnetization branch for both Θ=0° and Θ=90° are fully reversible, which is associated with the fact that the crystalline axes are parallel, respectively, to the x and y axes, thus opposing the tendency of the magnetostatic energy to create closed flux structures. When the reversal field is pushed to negative field and the nucleation field is reached, vortices appear and the magnetization almost vanishes; if the array is then remagnetized back to saturation (*i.e.* a half loop is performed) two different behaviors can be observed depending on the orientation of the

applied field (see fig. 7.5(b)). For Θ=0° the annihilation field of the half loop is below that of the full loop. This behavior implies that, the energy barrier to break the vortex nucleated in the half loop is smaller. Along the base of the triangle, shape anisotropy forces a chirality control: in the remagnetization branch from positive magnetization, the magnetic vortex is forced to be annihilated in the base of the triangles, whereas in the full loop, (saturating from negative magnetization), the vortex is forced to be annihilated in the tip of the triangles giving rise to a higher annihilation field. Along the Θ=90° direction, saturation is reached at a positive annihilation field equal to that measured in a full loop, showing that, along the base-to-tip direction, chirality control is lost. This chirality control has been reported in Ni polycrystalline nanotriangles with similar sizes [97, 98] and in asymmetric polycrystalline Co dots [99, 103].

From the previous magnetic characterization, we conclude that both arrays has an easy axis along the base of the triangles and exhibit similar remanent state after saturating along this direction (state 2 in fig. 7.4(a)). In contrast, when saturating along the base-to-tip direction, the different orientations of the magnetocrystalline axes produces different magnetic states at remanence: In the case of Array 1, some of the triangles exhibit positive nucleation field and, at remanence, some of them will exhibit a vortex state configuration; In the case of Array 2, where one of the easy axis is parallel to the base-to-tip direction, the nucleation field is negative, and the remanent magnetic configuration corresponds to a "buckle" configuration as shown in the state 2 in fig. 7.4(b).

7.4 Superconducting properties: Ratchet Effect

After the magnetic characterization of the arrays, ratchet effect was studied for both arrays in different remanent configurations.

7.4.1 Demagnetized State

As was explained in chapter 1, in these hybrid systems the magnetoresistance exhibits sharp periodic minima when the vortex density is an integer multiple of the pinning site density [8]. Hence, the number of vortices in the array is controlled by the external magnetic field perpendicular to the sample plane and they can be obtained from

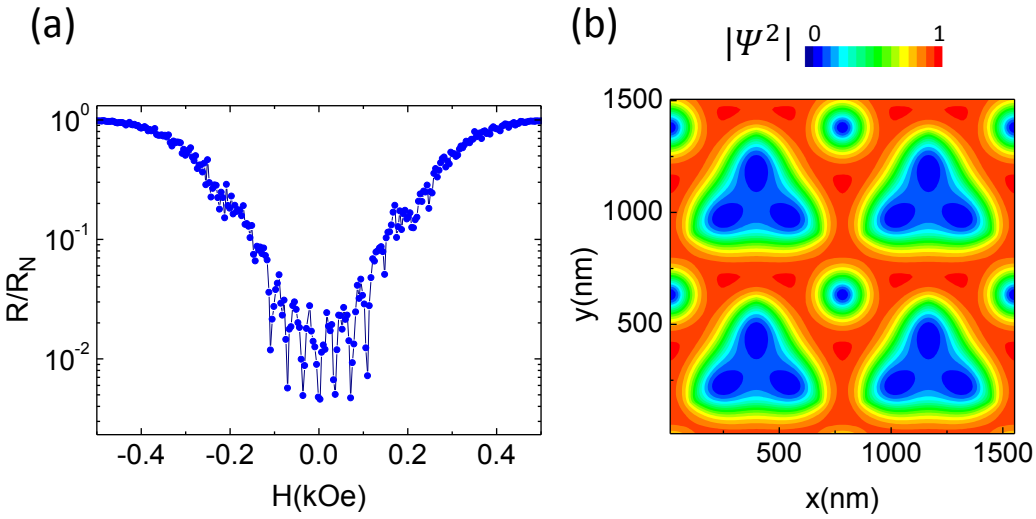

Figure 7.6: (a) Normalized resistance vs perpendicular applied magnetic fields at T = 8.37 K (T$_c$ =8.54 K) for Array-1. (b) Contourplot of the Cooper pair density obtained for H=4H$_{match}$. Blue/Red color corresponds to low/high Cooper pair density.(referencia capitulo)

magnetoresistance measurements. Both arrays show magnetoresistance curves (see fig. 7.6(a)) similar to those reported for arrays of Ni triangles [28]. Studying the vortex configuration obtained for H=4H$_{match}$ by the Ginzburg-Landau formalism (see fig. 7.6(b)), we can confirm that the filling factor of these triangles is three and that the fourth minimum corresponds to a vortex configuration where three vortices are placed on top of the triangles and the forth one is placed at an interstitial position. Experimentally, this can be seen in the magnetoresistance curve: the first, second and third minima are sharp and well defined, whereas, for higher matching fields, minima become shallow and not so well defined (see fig. 7.6(a)).

We have measured the ratchet effect in the demagnetized state, since in this state the only possible vortex ratchet effect is due to geometric asymmetry. Again, the experimental situation is the same than in vortex ratchet effect observed in Ni triangles [28]. Geometric ratchet effect is obtained when the vortex lattice moves parallel to the Y-axis (parallel to the triangle reflection axis). When vortex lattice moves parallel to the X-axis the ratchet effect is null, since the pinning potentials are symmetric, see

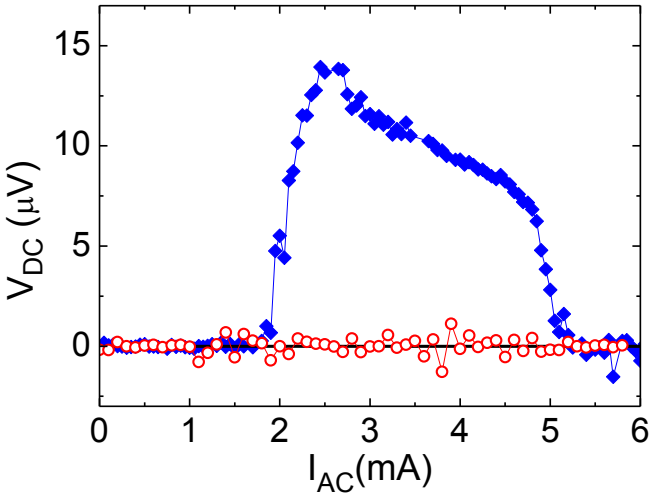

Figure 7.7: Array-1: V_{dc} *vs.* I_{ac} signal for the demagnetized state at T = 8.42 K, for N = 1 (one vortex per triangle), frequency is 10 kHz. Vortex motion parallel to Y-axis (full symbols) and vortex motion parallel to X-axis (hollow symbols).

fig. 7.7.

7.4.2 Magnetized State

Once we have obtained the usual geometric ratchet effect, the ratchet effect based on asymmetric magnetic potentials is studied.

Array-1

From the magnetic behavior explained in section 7.3, we get that, in this sample, the most relevant vortex lattice motion direction is parallel to X-axis, since in this direction the magnetization in the remanent state is enhanced. Moreover, vortex lattice motion parallel to X-axis does not show geometric ratchet effect, so we can study if magnetic ratchet appears without any mixing of the usual geometric ratchet. The remanent state after saturation along the X axis, as extracted by micromagnetic simulations, is shown in state 2 in fig. 7.4(a). The magnetization has a relatively large X component and it becomes parallel to the sides of the triangle near them. The largest density of poles in this configuration is clearly at the left (negative poles) and right (positive) vertex of

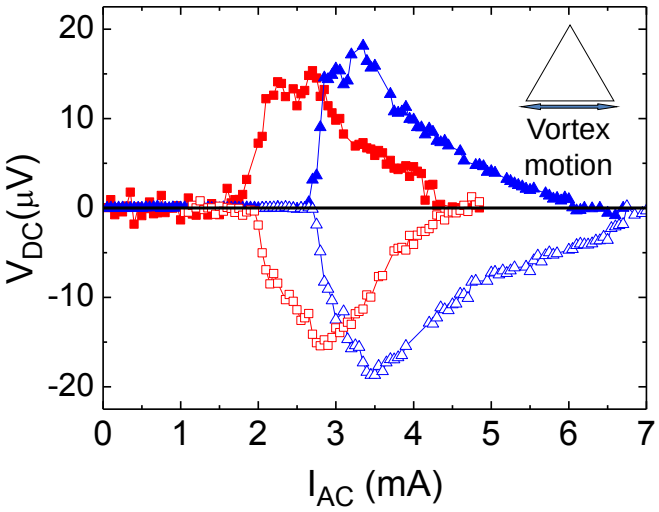

Figure 7.8: Array-1: output dc voltage vs. input ac current amplitude; the vortex motion is parallel to the base of the triangles and the magnetization is in the remanent configuration after saturating the sample along the positive (fill symbols) or negative (hollow symbols) X axis. The triangular and square symbols correspond, respectively, to data measured at 8.20K (0.96T$_c$) and 8.30 K (0.97T$_c$). The density of vortices, set by the perpendicular magnetic field, is 1 vortex per triangle.

the triangle. Therefore, a clear magnetic asymmetry arises from this array of Fe single crystal triangles and a new magnetic induced ratchet effect is expected. This magnetic asymmetry is absent in polycrystalline Ni triangles where the magnetic vortex state is the minimum energy magnetic configuration and no magnetic asymmetry is generated [28, 98].

To study the vortex ratchet effect, the remanent magnetic state is induced by saturating the sample along the X-axis. Afterwards, one vortex per unit cell is set by a perpendicular magnetic field H=H$_{match}$. The ratchet effect obtained for this remanent state is shown in fig. 7.8 at two different temperatures. This new result is induced only by the asymmetry of magnetic pinning potentials, as evidenced by the fact that the inversion of the in-plane magnetization changes the polarity of the ratchet effect (see again fig. 7.8).

In summary, in Array-1 sample geometrical and magnetic ratchet effects exist, but neither of them is associated with the same vortex motion direction. Both ratchet effects

(geometric and magnetic) show similar behavior; *i.e.* the ratchet amplitudes and the experimental values of the ac driving forces are similar.

Array-2

Ratchet with geometric and magnetic origins competing in the same vortex lattice motion direction is the second issue we have explored. To achieve this situation, Array 2 sample was studied. In this sample, see fig. 7.2(b), the magnetic easy directions are coincident with the X (base) and Y (base to tip) axes, respectively, making it easily to establish a magnetic configuration different to the magnetic vortex state along the base to tip direction: state 2 in fig. 7.4 can be stablished with a remanent magnetization of 50% of the saturation value. Therefore, this experimental setting is the ideal tool to study the coexistence of the two vortex ratchet mechanisms: magnetic and geometric asymmetries coexist along the base to tip direction.

So, for this case, we measure vortex ratchet effect with vortex lattice motion parallel to the Y-axis after saturating the sample in this direction. The rich phenomenology of the ratchet effect with geometric origin allows designing an experiment where the fingerprint of geometric ratchet is noticeable. As was mentioned in section 7.4.1, in our samples the filling factor is 3 vortices per triangle, so the fourth vortex is an interstitial one (fig. 7.6(b)). Dc voltage *vs.* ac current obtained for H=4H$_{match}$ is shown in fig. 7.9. In this case, increasing the strength of the driving ac current changes the polarity of the ratchet signal, *i.e.* vortex ratchet reversal is obtained. In addition, we carried out measurements under applied magnetic fields in opposite directions (H=4H$_{match}$ and H=-4H$_{match}$), and the ratchet signal is reversed, see again fig. 7.9. These two outcomes are a fingerprint of geometric asymmetry exclusively and underline that we are dealing with geometric ratchet unambiguously. Interestingly, in the measurements obtained with opposite directions of the applied fields, the maximum dc voltages obtained are similar. These experimental facts show that geometric ratchet effect is the dominant.

7.4.3 Discussion

The first question that emerges from the experimental results is why, in the remanent configuration after saturating along the Y-axis (base to tip), when motion is along

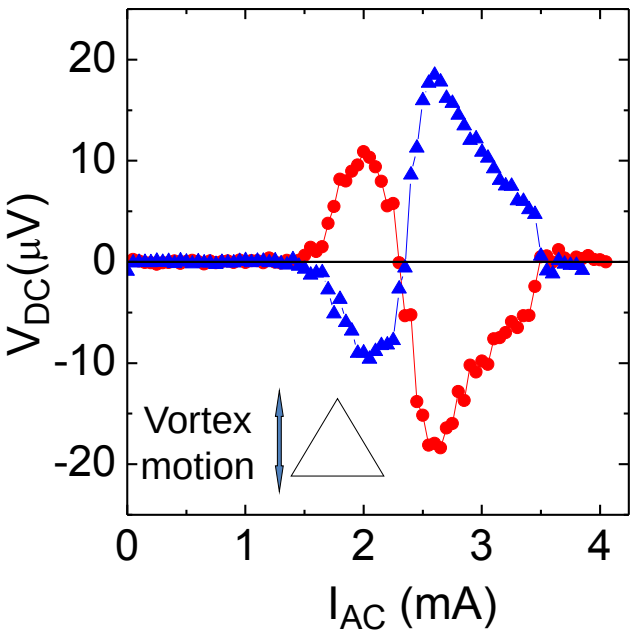

Figure 7.9: Array-2: output dc voltage vs. input ac current at 8.45 K and with N=4 vortices per lattice unit cell when the vortex motion is parallel to the base-to-tip direction. The magnetization is in the remanent configuration after positive saturation. Blue triangles (red circles) correspond to a perpendicular applied magnetic field H=4H_{match} (H=-4H_{match}).

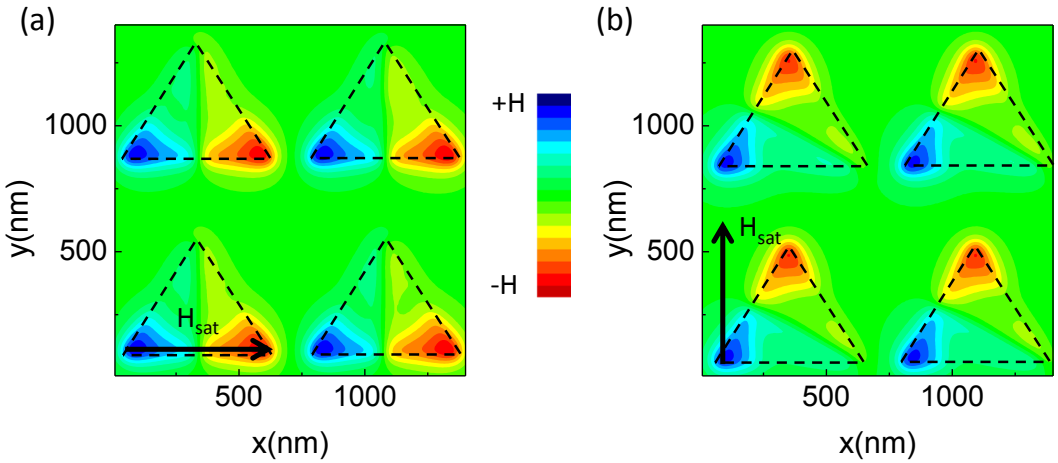

Figure 7.10: Array-2: Magnetic stray field generated by the remanent state obtained from simulations after saturation along the base direction (a) and along the base to tip direction (b). Dash lines show the position of the Fe single-crystal triangles. The arrows indicate the direction of the saturating applied fields.

this direction, there is no experimental evidence of magnetic ratchet. To answer this question, we have to demonstrate that the magnetic configuration obtained after saturation along the Y-axis (state 2 in fig. 7.4(b)) generates a magnetic ratchet effect in the base to tip direction. As explained before, this state exhibits a non-null remanent magnetization along the base direction, in fact, at remanence, almost 50% of the saturation magnetization lies along the X-axis and the other 50% lies along the Y-axis.

In fig. 7.10(b), we plot the stray field distribution obtained along the X-axis and Y-axis for this magnetic configuration. Similar magnetic asymmetry is detected in both directions and, if this asymmetry is enough to generate a ratchet effect, it should be present in both direction. So, we define a new experimental setting where the remanent state is kept the same than before and the geometric ratchet is not present, this is, the vortex lattice moves parallel to X-axis. Hollow circles in fig. 7.11(a) depicts vortex ratchet data associated to this new situation (vortex motion parallel to X-axis, and remanent state obtained after applying a saturating field parallel to Y-axis). We observe that, in this case, a well-defined vortex ratchet is obtained, so the asymmetry created in the stray field distribution by this magnetic configuration should generate magnetic ratchet effect along the Y-axis as well. However, as was shown in fig. 7.9, for vortex

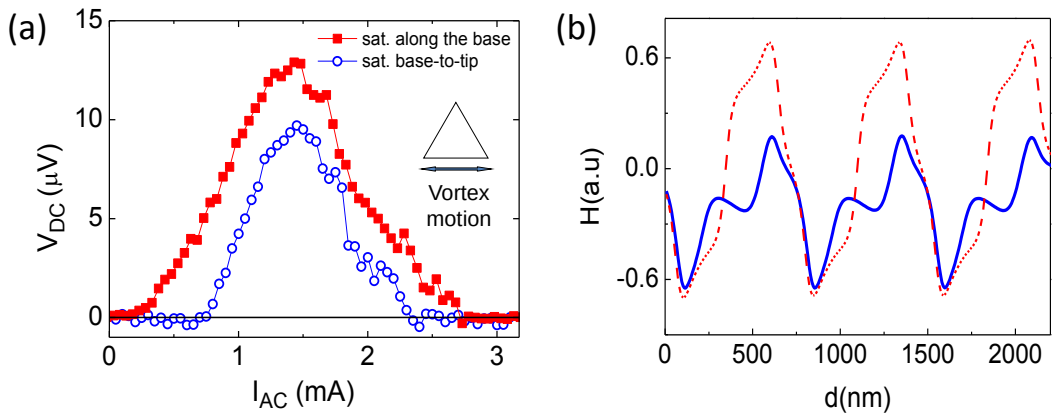

Figure 7.11: (a)Voltage dc drop vs. the driving current I_{ac} in Array-2, measured at 8.45 K and with N=4. The vortex motion is parallel to the base, after saturation either along the base (filled squares) or along the base to tip direction (hollow circles).(b)Magnetic stray field profile along the base of the triangles generated by the magnetic remanent configuration after saturation along the base to tip direction (blue line) and along the base direction (red dash line) for Array 2.

motion parallel to the Y-axis, only geometric ratchet was obtained. From this, we can conclude that, in this type of samples, when geometric and magnetic ratchet coexist, the rectifier effect is governed by the geometric potentials.

Now, we compare the ratchet signal obtained for the previous magnetic configuration (with 50% of magnetization parallel to the X-axis) with the ratchet signal obtained for the same vortex lattice motion (parallel to the X-axis) but after saturating along the triangle base direction (with 83% parallel to the X-axis). As shown in fig. 7.11(a) an enhancement of the ratchet effect is obtained with saturating magnetization parallel to the X-axis. Again, a hint to explain this behavior is the different stray field distributions in the X-axis direction generated by both magnetic states. Figure 7.10 (a) and (b) show the stray field distributions generated by the Fe motifs, as evaluated from the magnetic moments configuration shown in the states 2 in fig. 7.4, after saturation along X-axis and Y-axis respectively.

Fig. 7.11(b) shows the magnetic field profile along the vortex motion (parallel to the base of the triangles) obtained from fig. 7.10 (a) and (b). It is straightforward to see that stray field distribution exhibits higher asymmetry when it arises from saturating

magnetic fields applied along the X-axis direction than from the obtained after saturating magnetic fields applied in the Y-axis direction. This result confirms that the stray field distribution plays a crucial role in vortex ratchet induced by magnetic asymmetric pinning potentials.

7.5 Summary

The most important points of this chapter can be listed as follow:

- Asymmetry needed to obtained ratchet effect can be obtained either by geometric potentials or by magnetic potentials. The asymmetry of the geometric potential cannot be manipulated, whereas the asymmetry of the magnetic potential can be modified.
- The origin of the ratchet effect can be identify experimentally.

  Geometric ratchet effect:

  i. It is odd with the polarity of the applied magnetic field.
  ii. It exhibits ratchet reversal if interstitial vortices are present in the sample.

  Magnetic ratchet effect:

  i. It is even with the polarity of the magnetic field.
  ii. It is odd with the direction of the in-plane magnetization.
  iii. No ratchet reversal can be induced.
- Fe single-crystal triangular nanocenters have been used to study both ratchet mechanisms. The triangular shape allows defining a geometric asymmetry. On the other hand, the magneto-crystalline axes in competition with the shape anisotropy generates different magnetic configuration which can be modified at will so that a magnetic asymmetry can be induced.
- A magnetic asymmetry can develop pure magnetic ratchet effect. The distribution of magnetic stray fields is the key to control and understand this ratchet effect.
- In the case of experimental conditions for which both geometric and magnetic contributions to the ratchet effect coexist in the same direction, geometric contribution governs the global ratchet behavior.

Summary

The aim of this thesis was to study and control the vortex dynamics on superconducting thin films grown on top of arrays of nanocenters. The vortex pinning landscape can be easily manipulated using artificial pinning sites, therefore, the main attention was given to control the vortex dynamics by changing the arrangement, the shape and the magnetic state of the pinning centers.

For this purpose, several samples were fabricated by combination of lithography and DC sputtering techniques. Two different magnetometers and micromagnetic simulations were used for characterizing the magnetic properties of the pinning sites. Finally, the superconducting properties were studied by magnetotransport measurements.

Vortex dynamics in superconducting films grown on top of ordered arrays of pinning sites strongly depends on commensurability effects between the vortex lattice and the underlying pinning array. For certain fields (called matching fields), both lattices commensurate giving rise to different features in the superconducting properties: dips in the resistance, peaks in the critical current, shoulders in the magnetization and peaks in the susceptibility. As this type of samples are typically studied at temperatures close to T_c, it is not clear if the origin of these features is the vortex pinning enhancement in a thin film or the Little-Parks oscillations typically observed in superconducting wire networks. In *Chapter 3*, we have clarified the origin of these features by studying the superconducting properties over a wide range of temperature. A crossover was obtained at T= $0.993T_c$. Below this temperature, the system behaves like a thin film and the origin of the commensurability effect is an enhancement of the vortex pinning.

Once this origin was clarified, the influence of different geometries and magnetic states of the pinning sites in the vortex dynamics has been studied.

In *Chapter 4*, two samples formed by bicrystal-like structures were studied. In this case each array consisted of symmetric nanodots arranged in two different sublattices. In the first sample, the array consisted of a triangular and a square sublattices that ensured the same density of pinning centers along the whole bi-array. Identical commensurability effects were obtained independently of the vortex motion direction, so, from this experimental result, we conclude that this effect does not distinguish the moving vortex lattice arrangement. The second sample consisted of two sublattices with different pinning density; in addition, one of the halves exhibited an asymmetric pinning potential. Commensurability with both sublattices was obtained when the vortex lattice was crossing both arrays. Ratchet effect was induced in the lattice even though only half of the array exhibited asymmetry.

In *Chapter 5* the role of the magnetic stray fields was studied. For this aim, three different arrays of Co/Pd nanodots were fabricated. By changing the relative thickness of the Co/Pd layers, three different magnetic states were obtained: vortex state, single domain in plane and single domain out of plane. It has been reported in the literature that an increase in the magnetic stray field produces an increase in the critical current. However, our study was performed at currents higher than the critical one and vortices are already moving. In this regime, as extracted from the magnetoresistance curves, an increase in the stray fields leads to an increase in dissipation. In contrast, it was shown that dissipation is decreased by ordering the magnetic stray fields.

Under certain conditions, vortex-antivortex pairs (V-A) can be induced in a superconductor. In *Chapter 6* we studied an hybrid sample containing dots with out of plane magnetization, where V-AV pairs appeared due to the strong magnetic field modulation. By means of commensurability effect and Ginzburg-Landau simulations we were able to establish three different lattices: pure antivortex lattice, vortex lattice with all vortices pinned on the dots and vortex lattice with pinned and interstitial vortices. Dynamics of these lattices was studied by magnetotransport measurements. From the experimental results, we quantified the interaction between the periodic array and the different lattices and studied the range of velocity where these lattices order.

Finally, in *Chapter 7* we focused on the different mechanisms that can develop a superconducting ratchet effect. Particularly, using single-crystal Fe nanotriangles, we studied the competition between the geometric and magnetic ratchet effect. In this

chapter, we experimentally distinguished between both types of ratchets. Moreover, we show that the distribution of magnetic stray fields is the key to control and modify the magnetic ratchet effect. Finally we showed that when both asymmetries coexisted in the same direction, geometric asymmetry dominated the ratchet effect.

Resumen en español

El presente resumen comienza con una breve introducción a la superconductividad, centrándose en los superconductores tipo II y en la dinámica de vórtices. A continuación, se han expuesto los principales objetivos de este trabajo. Posteriormente, se explicará el sistema experimental, tanto los métodos empleados en la fabricación y caracterización de las muestras, como el sistema de licuación de Helio y el montaje de medida empleado. Finalmente, se resumirán y analizarán los principales resultados obtenidos durante el transcurso de esta tesis en distintos sistemas híbridos superconductor/magnético.

Introducción

Uno de los efectos más sorprendentes descubiertos en el último siglo dentro de la Física del Estado Sólido es la superconductividad. Este efecto fue descubierto en 1911 por H.K. Onnes al observar como al enfriar el Hg hasta la temperatura del helio líquido (4.2 K) se produce una caída súbita de la resistencia hasta cero. Este nuevo estado, denominado estado superconductor, ha sido muy atrayente tanto en el ámbito de la investigación básica como en el ámbito tecnológico debido a sus numerosas posibles aplicaciones.

El estado superconductor no sólo se caracteriza por una conducción sin disipación (resistencia eléctrica nula) sino que además tiene un comportamiento diamagnético perfecto (estado Meissner) en el que el campo magnético es expelido del interior del superconductor a través de corrientes superconductoras.

Las longitudes características de los superconductores son dos: la longitud coherente ξ que indica la distancia en la que varía la densidad de electrones superconductores y la longitud de penetración λ que indica la distancia que el campo magnético puede

penetrar en el superconductor. Ambas longitudes dependen de la temperatura y divergen en las proximidades de T_c.

Dependiendo de cómo se produce la transición al estado normal con un campo magnético aplicado, se distinguen dos tipos de superconductores: los superconductores tipo I y los superconductores tipo II (ver fig. 1.1). Los superconductores tipo II, a diferencia de los superconductores tipo I que transitan directamente desde el estado Meissner al estado normal, poseen en su diagrama de fases un estado intermedio superconductor entre el estado Meissner y el estado normal. Este nuevo estado es denominado estado mixto, estado de vórtices o estado de Abrikosov.

En el estado mixto o de Abrikosov, el flujo magnético penetra en el material de una forma cuantizada a través de los vórtices superconductores. Cada vórtice porta un quanto de flujo magnético Φ_0 (eq. (1.5)). La figura 1.2(a) muestra de forma esquemática la estructura de un vórtice. Constan de un núcleo de radio ξ en el que el campo magnético ha roto la superconductividad y el material ha pasado a estado normal. Están rodeados por corrientes superconductoras J_s que concentran el campo magnético en el nucleo y apantallan el resto del superconductor. Estas supercorrientes se extienden en una distancia λ.

A. A. Abrikosov demostró en 1957 que la interacción entre vórtices era repulsiva. Esto hace que el estado de mínima energía corresponda a una ordenación triangular de la red de vórtices como se observa en la fig. 1.2(b).

Al aplicar una densidad de corriente sobre la red de vórtices, éstos sufrirán una fuerza perpendicular a dicha corriente que vendrá dada por la fuerza de Lorentz (eq. (1.7)). Si esta fuerza es mayor que la fuerza de anclaje F_p, los vórtices adquirirán una velocidad neta en dirección perpendicular a la corriente produciendo un campo eléctrico disipativo. Por tanto, el movimiento de vórtices es disipativo y provoca una caída de potencial V y una resistencia R distinta de cero.

La introducción de centros de anclaje, aumenta la fuerza de pinning disminuyendo el movimiento de la red de vórtices. J. I. Martin *et al.* [8], mostraron que al crecer una lámina superconductora de Nb sobre una red de puntos magnéticos ordenados, aparece el denominado efecto de conmensurabilidad. Para ciertos campos (H_{match}), la densidad de vórtices es igual o proporcional a la densidad de puntos de anclaje. En estas condiciones de ajuste, la red de vórtices adopta la geometría de la red de anclaje,

disminuyendo su movimiento y provocando mínimos en la resistencia (ver como ejemplo fig. 3.2).

Villegas *et al.* [28] mostraron que al incluir una asimetría en la red de anclaje, usando puntos con forma triangular, se obtiene el denominado *efecto ratchet*. Al inyectar una corriente ac, los vórtices sienten una fuerza de Lorentz alterna cuyo promedio es nulo. Sin embargo, si los vórtices se mueven en un potencial asimétrico (en este caso a lo largo de la dirección punta-base), éstos adquieren una velocidad neta en una determinada dirección que depende de la asimetría de la red de anclaje.

Objetivos

El principal objetivo de esta tesis es el estudio y control de la dinámica de vórtices a través de centros de anclaje ordenados. Para ello, se han diseñado y fabricado muestras híbridas formadas por láminas superconductoras crecidas sobre redes de puntos magnéticos ordenados. Mediante el diseño de distintas geometrías y el control del estado magnético de los centros de anclaje, se ha realizado un estudio de la disipación en el estado mixto de superconductores tipo II.

Los siguientes objetivos se han ido cubriendo a lo largo de cada uno de los capítulos de esta tesis:

- Determinación del origen del efecto de commensurabilidad.
- Estudio del comportamiento disipativo de la red de vórtices moviéndose sobre redes formadas por dos zonas con distinta geometría.
- Análisis y control del campo de fuga generado por redes de puntos magnéticos y su influencia en la dinámica de vórtices.
- Estabilización de distintas redes de vórtices superconductores y comparación de sus dinámicas.
- Identificación y comparación del efecto ratchet originado por asimetrías magnética y geométrica.

Técnicas experimentales

A lo largo de esta tesis se han estudiado muestras híbridas superconductor magnético. La fig. 2.1 muestra de forma esquemática los distintos pasos necesarios para su fabricación. Sobre un sustrato (generalmente de Si), se define mediante combinación de litografía electrónica y sputtering la red de puntos de anclaje. A continuación mediante pulverización catódica en un sistema de alto vacío, se crece una lámina de 100 nm de Niobio superconductor. Finalmente, mediante litografía óptica y ataque iónico (RIE), se define un puente en forma de cruz para realizar las medidas de magnetotransporte.

La figura 2.11 muestra el sistema empleado para realizar las medidas a bajas temperaturas. Para conseguir bajas temperaturas es necesario el empleo de helio líquido; por ello, se dispone de un licuefactor comercial de la marca Quantum Technology Corporation. La licuación del helio se produce mediante tres ciclos de enfriamiento de temperaturas nominales 70 K, 15 K y 4.2 K. Además el laboratorio cuenta con un circuito cerrado de recuperación de helio que permite reutilizar el helio evaporado durante el proceso de medida.

Las medidas de magnetotransporte se realizan en dos criostatos de He líquido. Estos criostatos permiten aplicar altos campos magnéticos ya que constan de dos imanes superconductores (hasta 9 T). Además permiten estabilizar la temperatura de la muestra con una precisión de 1 mK.

El control de los distintos equipos necesarios para realizar las medidas (controlador de temperatura, amperímetro, voltímetro...) se lleva a cabo mediante el software LabView.

Resultados y conclusiones

A continuación se exponen los principales resultados y conclusiones para cada uno de los capítulos de esta tesis.

Origen del efecto de commensurabilidad

Una red de hilos superconductores entrelazados se denomina *superconducting wire network* (SWN). Si la anchura de los hilos (W) es comparable a la longitud coherente (ξ), aparece el efecto Little-Parks. Este efecto, basándose en la cuantización de flujo magnético, explica la aparición de oscilaciones en la temperatura crítica en los campos

de matching. Estudios recientes atribuyen la aparición de mínimos en la resistencia al efecto Little-Parks. Estos trabajaos se basan en que los estudios de dinámica de vórtices se realizan en temperaturas próximas a la temperatura crítica (T_c), donde la longitud coherente diverge, haciéndose comparable a la distancia entre los puntos. En este cápitulo, intentamos clarificar el origen de las anomalías observadas en las distintas propiedades superconductoras.

Para ello se ha fabricado una lámina de niobio sobre una red cuadrada (400 nm x 400 nm) de puntos de níquel de 200 nm de diámetro, siendo la distancia borde-borde entre los puntos W=200 nm. La longitud coherente obtenida a través de un ajustoe lineal del campo crítico perpendicular H_{c_2}, $\xi(T=0)$=9nm (fig. 3.7(b)).

Se han realizado medidas de las propiedades superconductoras en un amplio rango de temperaturas. En los campos de matching, se obtienen mínimos en la resistencia, maximos en la corriente crítica, escalones en la imanación y picos en la susceptibilidad. Éstos se mantienen hasta bajas temperaturas ($0.78T_c$) donde $\xi(0.78T_c) << W$, estando lejos del régimen de SWN (fig. 3.7). De este análisis confirmamos que el origen de estas anomalías es el anclaje de la red de vórtices. Sólo para temperaturas superiores a $0.993T_c$, $\xi > 1.84W$, entrando en el régimen de SWN y obteniendo máximos en la temperatura critica en los campos de matching.

Por último se ha realizado un estudio de la anchura de la transición superconductora en función del campo magnético. El paso de régimen SWN a anclaje de vórtices se observa como una aumento neto en la anchura de la transición. Mínimos en la anchura son obtenidos en los campos de matching en ambos regímenes.

Dinámica de vórtices en redes con doble geometría

El avance en las técnicas de litografía permite diseñar distintas geometrías para estudiar los efectos de commensurabilidad. En este capítulo muestras con doble geometría (dos redes distintas separadas por una frontera) han sido diseñadas para estudiar el comportamiento de la red de vórtices.

La primera muestra estudiada consta de una mitad en la que la red de puntos magnéticos define una red cuadrada y otra en la que la geometría es triangular (fig. 4.1). Los parámetros de red han sido elegidos tales que la densidad de puntos sea la mismo en ambas mitades, teniendo por tanto el mismo H_{match}. En este caso, mínimos en R(H)

son obtenidos para el movimiento de la red de vórtice paralelo y perpendicular a la frontera fig. 4.4. De estos resultados concluimos que el único parámetro que controla el efecto de commensurabilidad es la densidad de centros de anclaje y no su distribución geométrica.

La segunda muestra posee densidades de puntos distintos en cada mitad. La primera mitad tiene simetría triangular. La segunda mitad (de geometría similar a la kagomé) se ha obtenido eliminando 3 de cada 9 puntos de la red triangular (fig. 4.2). Además permite estudiar el efecto ratchet ya que la mitad con geometría tipo kagomé presenta ruptura de simetría.

En este caso, distintos efectos de commensurabilidad se obtienen dependiendo de la dirección de movimiento de la red de vórtices. Si el movimiento es paralelo a la frontera, la red de vórtices sólo se ajusta a la red de mayor densidad (la red triangular). Si el movimiento es perpendicular a la frontera, la red de vórtices viaja de una mitad a la otra, ajustándose a ambas (fig. 4.5). Además, se obtiene señal ratchet para el movimiento de vórtices en esta dirección (fig. 4.6).

Influencia del estado magnético en la dinámica de vórtices

Estudios previos han demostrado que un aumento en el campo magnético de fugas provoca un aumento en la fuerza de anclaje, que trae como consecuencia un aumento de la corriente crítica. Sin embargo, no se ha estudiado la influencia del aumento del campo de fugas en el régimen dinámico (para corrientes mayores que la corriente crítica). Este es el objetivo de este capítulo.

Para ello, se han crecido redes de puntos de Co/Pd con distintos espesores relativos de las capas de Co/Pd conseguiendo distintos estados magnéticos (fig. 5.1). Mediante una caracterización magnética basada en el análisis FORC, tres estados remanentes han sido identificados: estado vórtice (VS), estado monodominio en el plano (IPSD) y estado monodominio fuera del plano (OP). Simulaciones micromagnéticas han sido empleadas para calcular el campo de fugas producido por cada estado.

Tras obtener el estado remanente en las tres muestras, se han realizado medidas de disipación en función del campo magnético R(H) a $0.985T_c$ (fig. 5.7). La mayor disipación es obtenida para el caso de la muestra OP (mayor campo de fugas), y la menor para el caso VS (menor campo de fugas). De este análisis se obtiene que, a pesar

de que un mayor campo de fugas genera mayor corriente crítica, en el régimen dinámico (por encima de esta corriente) se obtiene mayor disipación para mayores campos de fuga.

Finalmente, se ha realizado un estudio por separado de cada una de las muestras. En el caso de OP (fig. 5.8), se obtiene una asimetría en la disipación dependiendo del alineamiento relativo entre el momento magnético de los puntos y el campo externo aplicado. En el caso de VS y IPSD se obtiene que al ordenar los momentos magnéticos de la red de centros de ancleje, se produce un potencial de anclaje ordenado que disminuye la disipación (fig. 5.9 y fig. 5.10, respectivamente).

Estudio de la dinámica de vórtices, antivórtices y vórtices intersticiales

La modificación local del campo magnético en un superconductor ofrece la posibilidad de estudiar nuevos aspectos de la dinámica de vórtices. En el caso de redes de puntos con momento magnético fuera del plano, éstos pueden generar pares de vórtices-antivórtices por su alto campo de fugas.

Una lámina de niobio ha sido crecida sobre una red de puntos formados por multicapas de Co/Pd. Estos puntos presentan anisotropía perpendicular, por lo que en estado remanente, se encuentran en forma de monodominio fuera del plano. En las medidas de R(H) se observa una asimetría entorno al primer campo de matching (fig. 6.2).

Para clarificar el origen de esta asimetría, realizamos simulaciones basadas en el formalismo de Ginzburg-Landau (GL). Estas simulaciones permiten obtener la distribución del módulo y de la fase del parámetro de orden superconductor. De esta forma, podemos obtener la distribución de los vórtices en función del campo magnético.

Como resultado de la combinación del efecto de commensurabilidad y la simulaciones GL, se han podido establecer tres redes (fig. 6.3). Para H=H_{match}, se obtiene una red de vórtices anclados sobre la red de puntos. Para H=-H_{match}, se obtiene una red de antivórtices anclados en posiciones intersticiales por efecto de repulsión con los puntos magnéticos. Finalmente, una red de vórtices anclados y vórtices intersticiales es establecida para H=4H_{match}.

Para las tres situaciones realizamos medidas de intensidad frente a voltaje (I *vs.* V) en condiciones de anclaje y fuera de anclaje. Restando la fuerza de Lorentz (F_L) en

ambas condiciones, se realiza un análisis de la fuerza de anclaje $\Delta F_L = F_{L_{matching}} - F_{L_{outofmatching}}$ en función de la velocidad v ($\Delta F_L vs. v$).

El mayor anclaje se obtiene para la red de vórtices anclados, que además se ordena para un mayor rango de velocidades. El caso de la red de antivórtices, ΔF_L es menor al igual que el rango de velocidades. Finalmente, la red de vórtices anclados e intersticiales, se ordena a mayores velocidades.

Medidante estas medidas, se ha cuantificado la diferencia de fuerzas necesaria para mover la red de vórtices y la red de antivórtices.

Efecto ratchet: coexistencia de asimetría magnética y geométrica

Como se indicó al inicio de este resumen, al someter la red de vórtices a fuerzas alternas, si éstos se mueven sobre un potencial asimétrico pueden adquirir velocidad neta en una determinada dirección. El potencial asimétrico se puede obtener mediante la asimetria geométrica o magnética. En esta sección se estudia la coexistencia de ambas asimetrías en arrays formados por triángulos de hierro monocristalinos (fig. 7.2).

El carácter monocristalino de los triángulos de hierro permite establecer distintos estados remanentes según la dirección de aplicación del campo magnético (fig. 7.4). De esta forma, y mediante el estudio de los campos de fuga creados por estos estados, la asimetría magnética puede ser controlada y modificada.

Tras saturar los triángulos a lo largo de la base, una asimetría magnética es generada en esta dirección. En este caso, se obtiene una señal rectificada con origen puramente magnético. El ratchet magnético se identifica por ser par respecto al campo magnético externo y por la ausencia de señal invertida en la presencia de vórtices intersticiales (fig. 7.8).

Tras saturar los triángulos en la dirección de base a punta, una asimetría magnética es inducida. De esta forma, ambas asimetrías (magnética y geométrica) coexisten en esta dirección. En este caso (fig. 7.9), la señal rectificante obtenida muestra las propiedades de ratchet de origen puramente geométrico (impar con el campo y señal invertida debido a los vórtices intersiticiales).

Bibliography

[1] H. Togalla and P. H. Kes *100 years of superconductivity*. CRC Press (2011).

[2] J. Bednorz and K. Müller "Possible high Tc superconductivity in the BaLaCuO system", *Zeitschrift für Physik B Condensed Matter* **64**, 189–193 (1986).

[3] M. K. Wu, J. R. Ashburn, C. J. Torng, P. H. Hor, R. L. Meng, L. Gao, Z. J. Huang, Y. Q. Wang, and C. W. Chu "Superconductivity at 93 K in a new mixed-phase Y-Ba-Cu-O compound system at ambient pressure", *Phys. Rev. Lett.* **58**, 908–910 (1987).

[4] *US Department of Energy report, Basic Research Needs for Superconductivity*. 2006. URL: www.er.doe.gov/bes/reports/files/SCrpt.pdf.

[5] M. Tinkham *Introduction to Superconductivity*. Dover (1996).

[6] L Civale "Vortex pinning and creep in high-temperature superconductors with columnar defects", *Superconductor Science and Technology* **10**, A11 (1997).

[7] M. Baert, V. V. Metlushko, R. Jonckheere, V. V. Moshchalkov, and Y. Bruynseraede "Composite Flux-Line Lattices Stabilized in Superconducting Films by a Regular Array of Artificial Defects", *Phys. Rev. Lett.* **74**, 3269–3272 (1995).

[8] J. I. Martin, M. Velez, J. Nogues, and I. K. Schuller "Flux Pinning in a Superconductor by an Array of Submicrometer Magnetic Dots", *Phys. Rev. Lett.* **79**, 1929–1932 (1997).

[9] P. De Gennes *Superconductivity Of Metals And Alloys*. Advanced Book Program, Perseus Books (1999).

[10] H. F. Hess, R. B. Robinson, R. C. Dynes, J. M. Valles, and J. V. Waszczak "Scanning-Tunneling-Microscope Observation of the Abrikosov Flux Lattice and the Density of States near and inside a Fluxoid", *Phys. Rev. Lett.* **62**, 214–216 (1989).

[11] U. Essmann and H. Träuble "The direct observation of individual flux lines in type {II} superconductors", *Physics Letters A* **24**, 526 –527 (1967).

[12] Y. Fasano and M. Menghini "Magnetic-decoration imaging of structural transitions induced in vortex matter", *Superconductor Science and Technology* **21**, 023001 (2008).

[13] I. Guillamon, H. Suderow, A. Fernandez-Pacheco, J. Sese, R. Cordoba, J. M. De Teresa, M. R. Ibarra, and S. Vieira "Direct observation of melting in a two-dimensional superconducting vortex lattice", *Nat. Phys.* **5**, 651–655 (2009).

[14] K. Harada, O. Kamimura, H. Kasai, T. Matsuda, A. Tonomura, and V. V. Moshchalkov "Direct Observation of Vortex Dynamics in Superconducting Films with Regular Arrays of Defects", *Science* **274**, 1167–1170 (1996).

[15] R. B. G. Kramer, A. V. Silhanek, W. Gillijns, and V. V. Moshchalkov "Imaging the Statics and Dynamics of Superconducting Vortices and Antivortices Induced by Magnetic Microdisks", *Phys. Rev. X* **1**, 021004 (2011).

[16] A Oral, S. J. Bending, R. G. Humphreys, and M Henini "Microscopic measurement of penetration depth in thin films by scanning Hall probe microscopy", *Superconductor Science and Technology* **10**, 17 (1997).

[17] K. Buschow *Concise Encyclopedia of Magnetic and Superconducting Materials*. Elsevier Science (2005).

[18] M. Velez, J. Martin, J. Villegas, A. Hoffmann, E. Gonzalez, J. Vicent, and I. K. Schuller "Superconducting vortex pinning with artificial magnetic nanostructures", *Journal of Magnetism and Magnetic Materials* **320**, 2547 –2562 (2008).

[19] A. Y. Aladyshkin, A. V. Silhanek, W Gillijns, and V. V. Moshchalkov "Nucleation of superconductivity and vortex matter in superconductor–ferromagnet hybrids", *Superconductor Science and Technology* **22**, 053001 (2009).

[20] A. Hoffmann, P. Prieto, and I. K. Schuller "Periodic vortex pinning with magnetic and nonmagnetic dots: The influence of size", *Phys. Rev. B* **61**, 6958–6965 (2000).

[21] J. I. Martin, M. Velez, A. Hoffmann, I. K. Schuller, and J. L. Vicent "Artificially Induced Reconfiguration of the Vortex Lattice by Arrays of Magnetic Dots", *Phys. Rev. Lett.* **83**, 1022–1025 (1999).

[22] D. Perez de Lara, A. Alija, E. M. Gonzalez, M. Velez, J. I. Martin, and J. L. Vicent "Vortex ratchet reversal at fractional matching fields in kagomélike array with symmetric pinning centers", *Phys. Rev. B* **82**, 174503 (2010).

[23] M. F. Laguna, C. A. Balseiro, D. Domínguez, and F. Nori "Vortex structure and dynamics in kagomé and triangular pinning potentials", *Phys. Rev. B* **64**, 104505 (2001).

[24] T. C. Wu, J. C. Wang, L. Horng, J. C. Wu, and T. J. Yang "Temperature dependence of vortex configuration by honeycomb hole arrays in a superconducting Nb film", *Journal of Applied Physics* **97**, 10B102 (2005).

[25] J. E. Villegas, M. I. Montero, C.-P. Li, and I. K. Schuller "Correlation Length of Quasiperiodic Vortex Lattices", *Phys. Rev. Lett.* **97**, 027002 (2006).

[26] C. S. Lee, B. Janko, I. Derenvi, and A. L. Barabasi "Reducing vortex density in superconductors using the ratchet effect", *Nature* **400**, 337–340 (1999).

[27] P. Hänggi and F. Marchesoni "Artificial Brownian motors: Controlling transport on the nanoscale", *Rev. Mod. Phys.* **81**, 387–442 (2009).

[28] J. E. Villegas, S. Savel'ev, F. Nori, E. M. Gonzalez, J. V. Anguita, R. Garcia, and J. L. Vicent "A Superconducting Reversible Rectifier That Controls the Motion of Magnetic Flux Quanta", *Science* **302**, 1188–1191 (2003).

[29] B. L. T. Plourde "Nanostructured Superconductors With Asymmetric Pinning Potentials: Vortex Ratchets", *Applied Superconductivity, IEEE Transactions on* **19**, 3698–3714 (2009).

[30] D. Adelerhof, M. Bijlsma, P. Fransen, T. Weiman, J. Flokstra, and H. Rogalla "Fabrication of Nb/Al,AlOx/Al/Nb Josephson tunnel junctions using reactive ion etching in {SF6}", *Physica C: Superconductivity* **209**, 477 –485 (1993).

[31] P. F. Miceli, D. A. Neumann, and H. Zabel "X-ray refractive index: A tool to determine the average composition in multilayer structures", *Applied Physics Letters* **48**, 24–26 (1986).

[32] E Paz, F Cebollada, F. J. Palomares, F García-Sánchez, and J. M. González "Control of magnetization reversal by combining shape and magnetocrystalline anisotropy in epitaxial Fe planar nanowires", *Nanotechnology* **21**, 255301 (2010).

[33] W. Brown *Micromagnetics*. Interscience Publishers. (1963).

[34] H. Kronmüller and M. Fähnle *Micromagnetism and the Microstructure of Ferromagnetic Solids*. Cambridge University Press (2003).

[35] B. Cullity and C. Graham *Introduction to Magnetic Materials*. Wiley (2011).

[36] *math.nist.gov/oommf*.

[37] *http://inkscape.org/*.

[38] A. Gomez, E. M. Gonzalez, and J. L. Vicent "Superconducting vortex dynamics on arrays with bicrystal-like structures: matching and rectifier effects", *Superconductor Science and Technology* **25**, 124006 (2012).

[39] J. I. Martin, M. Velez, A. Hoffmann, I. K. Schuller, and J. L. Vicent "Temperature dependence and mechanisms of vortex pinning by periodic arrays of Ni dots in Nb films", *Phys. Rev. B* **62**, 9110–9116 (2000).

[40] B. Pannetier, J. Chaussy, R. Rammal, and J. C. Villegier "Experimental Fine Tuning of Frustration: Two-Dimensional Superconducting Network in a Magnetic Field", *Phys. Rev. Lett.* **53**, 1845–1848 (1984).

[41] C. C. Abilio, P. Butaud, T. Fournier, B. Pannetier, J. Vidal, S. Tedesco, and B. Dalzotto "Magnetic Field Induced Localization in a Two-Dimensional Superconducting Wire Network", *Phys. Rev. Lett.* **83**, 5102–5105 (1999).

[42] U. Patel, Z. L. Xiao, J. Hua, T. Xu, D. Rosenmann, V. Novosad, J. Pearson, U. Welp, W. K. Kwok, and G. W. Crabtree "Origin of the matching effect in a superconducting film with a hole array", *Phys. Rev. B* **76**, 020508 (2007).

[43] V. V. Moshchalkov, M. Baert, V. V. Metlushko, E. Rosseel, M. J. Van Bael, K. Temst, Y. Bruynseraede, and R. Jonckheere "Pinning by an antidot lattice: The problem of the optimum antidot size", *Phys. Rev. B* **57**, 3615–3622 (1998).

[44] Y. Bruynseraede, T. Puig, E. Rosseel, M. Baert, M. Bael, K. Temst, V. Moshchalkov, and R. Jonckheere "Flux confinement by artificial arrays and clusters in superconducting films", *Journal of Low Temperature Physics* **106**, 173–182 (1997).

[45] R. D. Parks and W. A. Little "Fluxoid Quantization in a Multiply-Connected Superconductor", *Phys. Rev.* **133**, A97–A103 (1964).

[46] M. Tinkham, D. W. Abraham, and C. J. Lobb "Periodic flux dependence of the resistive transition in two-dimensional superconducting arrays", *Phys. Rev. B* **28**, 6578–6581 (1983).

[47] V. V. Moshchalkov, M. Baert, V. V. Metlushko, E. Rosseel, M. J. Van Bael, K. Temst, R. Jonckheere, and Y. Bruynseraede "Magnetization of multiple-quanta vortex lattices", *Phys. Rev. B* **54**, 7385–7393 (1996).

[48] U. Welp, Z. L. Xiao, J. S. Jiang, V. K. Vlasko-Vlasov, S. D. Bader, G. W. Crabtree, J. Liang, H. Chik, and J. M. Xu "Superconducting transition and vortex pinning in Nb films patterned with nanoscale hole arrays", *Phys. Rev. B* **66**, 212507 (2002).

[49] D Bothner, C Clauss, E Koroknay, M Kemmler, T Gaber, M Jetter, M Scheffler, P Michler, M Dressel, D Koelle, and R Kleiner "The phase boundary of superconducting niobium thin films with antidot arrays fabricated with microsphere photolithography", *Superconductor Science and Technology* **25**, 065020 (2012).

[50] C. Chiliotte, G. Pasquini, V. Bekeris, J. E. Villegas, C. Li, and I. K. Schuller "Vortex lattice dynamics in Nb films with competing intrinsic random and artificial periodic pinning", *Superconductor Science and Technology* **24**, 065008 (2011).

[51] O. M. Stoll, M. I. Montero, J. Guimpel, J. J. Åkerman, and I. K. Schuller "Hysteresis and fractional matching in thin Nb films with rectangular arrays of nanoscaled magnetic dots", *Phys. Rev. B* **65**, 104518 (2002).

[52] A. V. Silhanek, S. Raedts, M. Lange, and V. V. Moshchalkov "Field-dependent vortex pinning strength in a periodic array of antidots", *Phys. Rev. B* **67**, 064502 (2003).

[53] V. Metlushko, U. Welp, G. W. Crabtree, R. Osgood, S. D. Bader, L. E. DeLong, Z. Zhang, S. R. J. Brueck, B. Ilic, K. Chung, and P. J. Hesketh "Interstitial flux phases in a superconducting niobium film with a square lattice of artificial pinning centers", *Phys. Rev. B* **60**, R12585–R12588 (1999).

[54] R. R. Hake "Paramagnetic Superconductivity in Extreme Type-II Superconductors", *Phys. Rev.* **158**, 356–376 (1967).

[55] A. V. Silhanek, L. Van Look, S. Raedts, R. Jonckheere, and V. V. Moshchalkov "Guided vortex motion in superconductors with a square antidot array", *Phys. Rev. B* **68**, 214504 (2003).

[56] J. E. Villegas, E. M. Gonzalez, M. I. Montero, I. K. Schuller, and J. L. Vicent "Vortex-lattice dynamics with channeled pinning potential landscapes", *Phys. Rev. B* **72**, 064507 (2005).

[57] C. C. de Souza Silva, J. Van de Vondel, M. Morelle, and V. V. Moshchalkov "Controlled multiple reversals of a ratchet effect", *Nature* **440**, 651–654 (2006).

[58] J. E. Villegas, M. I. Montero, C.-P. Li, and I. K. Schuller "Correlation Length of Quasiperiodic Vortex Lattices", *Phys. Rev. Lett.* **97**, 027002 (2006).

[59] Y. J. Rosen, A. Sharoni, and I. K. Schuller "Enhanced superconducting vortex pinning with disordered nanomagnetic arrays", *Phys. Rev. B* **82**, 014509 (2010).

[60] A. Y. Aladyshkin, A. I. Buzdin, A. A. Fraerman, A. S. Mel'nikov, D. A. Ryzhov, and A. V. Sokolov "Domain wall superconductivity in hybrid superconductor ferromagnet structures", *Phys. Rev. B* **68**, 184508 (2003).

[61] Z. Yang, M. Lange, A. Volodin, R. Szymczak, and V. V. Moshchalkov "Domain-wall superconductivity in superconductor-ferromagnet hybrids", *Nat. Mater.* **3**, 793 (2004).

[62] C. Pike and A. Fernandez "An investigation of magnetic reversal in submicron-scale Co dots using first order reversal curve diagrams", *Journal of Applied Physics* **85**, 6668–6676 (1999).

[63] C. R. Pike "First-order reversal-curve diagrams and reversible magnetization", *Phys. Rev. B* **68**, 104424 (2003).

[64] I. D. Mayergoyz "Mathematical Models of Hysteresis", *Phys. Rev. Lett.* **56**, 1518–1521 (1986).

[65] I. Mayergoyz and G. Friedman "Generalized Preisach model of hysteresis", *Magnetics, IEEE Transactions on* **24**, 212–217 (Jan).

[66] J. W., P. Greene, R. K. Dumas, and K. Liu "Probing magnetic configurations in Co/Cu multilayered nanowires", *Applied Physics Letters* **94**, 032504 (2009).

[67] R. K. Dumas, C.-P. Li, I. V. Roshchin, I. K. Schuller, and K. Liu "Magnetic fingerprints of sub-100nm Fe dots", *Phys. Rev. B* **75**, 134405 (2007).

[68] T. Shinjo, T. Okuno, R. Hassdorf, . K. Shigeto, and T. Ono "Magnetic Vortex Core Observation in Circular Dots of Permalloy", *Science* **289**, 930–932 (2000).

[69] R. P. Cowburn, D. K. Koltsov, A. O. Adeyeye, M. E. Welland, and D. M. Tricker "Single Domain Circular Nanomagnets", *Phys. Rev. Lett.* **83**, 1042–1045 (1999).

[70] C.-J. Lin, G. Gorman, C. Lee, R. Farrow, E. Marinero, H. Do, H. Notarys, and C. Chien "Magnetic and structural properties of Co/Pt multilayers", *Journal of Magnetism and Magnetic Materials* **93**, 194 –206 (1991).

[71] P. F. Carcia, A. D. Meinhaldt, and A. Suna "Perpendicular magnetic anisotropy in Pd/Co thin film layered structures", *Applied Physics Letters* **47**, 178–180 (1985).

[72] B. J. Kirby, J. E. Davies, K. Liu, S. M. Watson, G. T. Zimanyi, R. D. Shull, P. A. Kienzle, and J. A. Borchers "Vertically graded anisotropy in Co/Pd multilayers", *Phys. Rev. B* **81**, 100405 (2010).

[73] B. J. Kirby, S. M. Watson, J. E. Davies, G. T. Zimanyi, K. Liu, R. D. Shull, and J. A. Borchers "Direct observation of magnetic gradient in Co/Pd pressure-graded media", *Journal of Applied Physics* **105**, 07C929 (2009).

[74] M. V. Milosevic, F. M. Peeters, and B Janko "Vortex manipulation in superconducting films with tunable magnetic topology", *Superconductor Science and Technology* **24**, 024001 (2011).

[75] A. Silhanek, N. Verellen, V. Metlushko, W. Gillijns, F. Gozzini, B. Ilic, and V. Moshchalkov "Rectification effects in superconductors with magnetic pinning centers", *Physica C: Superconductivity* **468**, 563 –567 (2008).

[76] M. J. Bael, K. Temst, L. V. Look, J. Bekaert, V. V. Moshchalkov, and Y. Bruynseraede "Flux pinning by magnetic dots with in-plane magnetization", *Physica B: Condensed Matter* **284-288, Part 1**, 893 –894 (2000).

[77] D. J. Morgan and J. B. Ketterson "Asymmetric Flux Pinning in a Regular Array of Magnetic Dipoles", *Phys. Rev. Lett.* **80**, 3614–3617 (1998).

[78] M. Lange, M. J. V. Bael, Y. Bruynseraede, and V. V. Moshchalkov "Nanoengineered Magnetic-Field-Induced Superconductivity", *Phys. Rev. Lett.* **90**, 197006 (2003).

[79] M. V. Milosevic and F. M. Peeters "Vortex-Antivortex Lattices in Superconducting Films with Magnetic Pinning Arrays", *Phys. Rev. Lett.* **93**, 267006 (2004).

[80] M. V. Milosevic and F. M. Peeters "Vortex-Antivortex Nucleation in Magnetically Nanotextured Superconductors: Magnetic-Field-Driven and Thermal Scenarios", *Phys. Rev. Lett.* **94**, 227001 (2005).

[81] L. F. Chibotaru, A. Ceulemans, V. Buyndoncx, and V. V. Moshchalkov "Symmetry-induced formation of antivortices in mesoscopic superconductors", *Nature* **408**, 833 (2000).

[82] V. R. Misko, V. M. Fomin, J. T. Devreese, and V. V. Moshchalkov "Stable Vortex-Antivortex Molecules in Mesoscopic Superconducting Triangles", *Phys. Rev. Lett.* **90**, 147003 (2003).

[83] M. V. Milosevic and F. M. Peeters "Field-enhanced critical parameters in magnetically nanostructured superconductors", *Europhysics Letters* **70**, 670 (2005).

[84] J. S. Neal, M. V. Milosevic, S. J. Bending, A. Potenza, L. San Emeterio, and C. H. Marrows "Competing Symmetries and Broken Bonds in Superconducting Vortex-Antivortex Molecular Crystals", *Phys. Rev. Lett.* **99**, 127001 (2007).

[85] M. Iavarone, A. Scarfato, F. Bobba, M. Longobardi, G. Karapetrov, V. Novosad, V. Yefremenko, F. Giubileo, and A. M. Cucolo "Imaging the spontaneous formation of vortex-antivortex pairs in planar superconductor/ferromagnet hybrid structures", *Phys. Rev. B* **84**, 024506 (2011).

[86] M. Lange, M. J. Van Bael, A. V. Silhanek, and V. V. Moshchalkov "Vortex-antivortex dynamics and field-polarity-dependent flux creep in hybrid superconductor/ferromagnet nanostructures", *Phys. Rev. B* **72**, 052507 (2005).

[87] M. Velez, D. Jaque, J. I. Martin, F. Guinea, and J. L. Vicent "Order in driven vortex lattices in superconducting Nb films with nanostructured pinning potentials", *Phys. Rev. B* **65**, 094509 (2002).

[88] M. Milosevic *Vortex Matter in Mesoscopic Superconductor / Ferromagnet Heterosystems.*. PhD Thesis, Universiteit Antwerpen (2004).

[89] T. C. Wu, L. Horng, J. C. Wu, R. Cao, J. KolaCek, and T. J. Yang "Vortex ratchet effect in a niobium film with spacing-graded density of pinning sites", *Journal of Applied Physics* **102**, 033918 (2007).

[90] Y. Togawa, K. Harada, T. Akashi, H. Kasai, T. Matsuda, F. Nori, A. Maeda, and A. Tonomura "Direct Observation of Rectified Motion of Vortices in a Niobium Superconductor", *Phys. Rev. Lett.* **95**, 087002 (2005).

[91] J. E. Villegas, E. M. Gonzalez, M. P. Gonzalez, J. V. Anguita, and J. L. Vicent "Experimental ratchet effect in superconducting films with periodic arrays of asymmetric potentials", *Phys. Rev. B* **71**, 024519 (2005).

[92] C. C. de Souza Silva, A. V. Silhanek, J. Van de Vondel, W. Gillijns, V. Metlushko, B. Ilic, and V. V. Moshchalkov "Dipole-Induced Vortex Ratchets in Superconducting Films with Arrays of Micromagnets", *Phys. Rev. Lett.* **98**, 117005 (2007).

[93] D. Perez de Lara, F. J. Castano, B. G. Ng, H. S. Korner, R. K. Dumas, E. M. Gonzalez, K. Liu, C. A. Ross, I. K. Schuller, and J. L. Vicent "Rocking ratchet induced by pure magnetic potentials with broken reflection symmetry", *Phys. Rev. B* **80**, 224510 (2009).

[94] D. P. de Lara, F. J. Castano, B. G. Ng, H. S. Korner, R. K. Dumas, E. M. Gonzalez, K. Liu, C. A. Ross, I. K. Schuller, and J. L. Vicent "Magnetic pinning of flux lattice in superconducting-nanomagnet hybrids", *Applied Physics Letters* **99**, 182509 (2011).

[95] R. P. Cowburn, A. O. Adeyeye, and M. E. Welland "Configurational Anisotropy in Nanomagnets", *Phys. Rev. Lett.* **81**, 5414–5417 (1998).

[96] P. Vavassori, N. Zaluzec, V. Metlushko, V. Novosad, B. Ilic, and M. Grimsditch "Magnetization reversal via single and double vortex states in submicron Permalloy ellipses", *Phys. Rev. B* **69**, 214404 (2004).

[97] M. Jaafar, R. Yanes, D. Perez de Lara, O. Chubykalo-Fesenko, A. Asenjo, E. M. Gonzalez, J. V. Anguita, M. Vazquez, and J. L. Vicent "Control of the chirality and polarity of magnetic vortices in triangular nanodots", *Phys. Rev. B* **81**, 054439 (2010).

[98] M. Jaafar, R. Yanes, A. Asenjo, O. Chubykalo-Fesenko, M. Vazquez, E. M. Gonzalez, and J. L. Vicent "Field induced vortex dynamics in magnetic Ni nanotriangles", *Nanotechnology* **19**, 285717 (2008).

[99] R. K. Dumas, D. A. Gilbert, N. Eibagi, and K. Liu "Chirality control via double vortices in asymmetric Co dots", *Phys. Rev. B* **83**, 060415 (2011).

[100] J. Mejia-Lopez, D. Altbir, A. H. Romero, X. Batlle, I. V. Roshchin, C.-P. Li, and I. K. Schuller "Vortex state and effect of anisotropy in sub-100-nm magnetic nanodots", *Journal of Applied Physics* **100**, 104319 (2006).

[101] L. Thevenard, H. T. Zeng, D. Petit, and R. P. Cowburn "Six-fold configurational anisotropy and magnetic reversal in nanoscale Permalloy triangles", *Journal of Applied Physics* **106**, 063902 (2009).

[102] D. K. Koltsov, R. P. Cowburn, and M. E. Welland "Micromagnetics of ferromagnetic equilateral triangular prisms", *Journal of Applied Physics* **88**, 5315–5317 (2000).

[103] R. K. Dumas, T. Gredig, C.-P. Li, I. K. Schuller, and K. Liu "Angular dependence of vortex-annihilation fields in asymmetric cobalt dots", *Phys. Rev. B* **80**, 014416 (2009).

List of Publications

1. **Probing the dynamic response of antivortex, interstitial and trapped vortex lattices on magnetic periodic pinning potentials**
   A. Gomez, E. M. Gonzalez, D. A. Gilbert, M.V. Milosevic, K. Liu, J. L. Vicent
   Superconductor Science and Technology **26**, In press (2013)

2. **Low Temperature Vortex Dynamics in Superconducting Nb Films Containing Square and Rectangular Arrays of Ni Nanodots**
   C. E. Chiliotte, S. J. Carreira, V. Bekeris, A. Gomez, E. M. Gonzalez, J. L. Prieto, J. L. Vicent
   IEEE Transactions on Magnetics **49**, In press (2013)

3. **A superconducting/magnetic hybrid rectifier based on Fe single-crystal nanocentres: role of magnetic and geometric asymmetries**
   A. Gomez, E. M. Gonzalez, M. Iglesias, N. Sanchez, F. J. Palomares, F. Cebollada, J. M. Gonzalez, J. L. Vicent
   Journal of Physics D: Applied Physics **49**, 095302 (2013)

4. **Vortex lattice motion in the flux creep regime on asymmetric pinning potentials**
   D. Perez de Lara, M. Velez, A. Gomez, F. Galvez, A. Alija, M. A. Garcia, J. I. Martin, E. M. Gonzalez, J. L. Vicent
   Superconductor Science and Technology **26**, 035016 (2013)

5. **Control of dissipation in superconducting films by magnetic stray fields**
   A. Gomez, D. A. Gilbert, E. M. Gonzalez, K. Liu, J. L. Vicent
   Applied Physics Letters **102**, 052601 (2013)

6. **Superconducting vortex dynamics on arrays with bicrystal-like structures: matching and rectifier effects**
   A. Gomez, E. M. Gonzalez, J. L. Vicent
   Superconductor Science and Technology **25**, 124006 (2012)

7. **Superconducting Vortex Lattice Configurations on Periodic Potentials: Simulation and Experiment**
   M. Rodriguez-Pascual, A. Gomez, R. Mayo-Garcia, D. Perez de Lara, E. M. Gonzalez, A. J. Rubio-Montero, J. L. Vicent
   Superconductivity and Novel Magnetism **25**, 2127 (2012)

8. **Amorphous and crystalline magnetic/superconducting hybrids: Interplay between periodic defects and random defects**
   A. Gomez, D. Perez de Lara, A. Alija, E. M. Gonzalez, J. I. Martin, M. Velez, J. L. Vicent
   IEEE Transactions on Applied Superconductivity **21**, 2597 (2011)